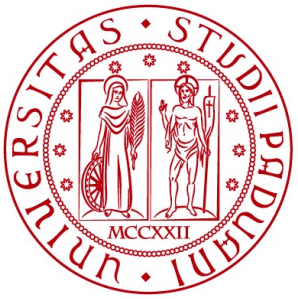

UNIVERSITÀ DEGLI STUDI DI PADOVA

Università degli Studi di Padova

DEPARTMENT OF CIVIL, ENVIRONMENTAL AND ARCHITECTURAL ENGINEERING

Ph.D. course in: Civil and Environmental Engineering Sciences

COORDINATOR: **Prof. Stefano Lanzoni**

Water and Sediment Temperature Dynamics in Shallow Tidal Environments

Ph.D. Student:
Mattia Pivato

Advisor:
Prof. Luca Carniello

Co-advisors:
Prof. Marco Marani
Dr. Sonia Silvestri

XXX Series

Abstract

The purpose of the present study is to investigate the water and sediment temperature dynamics in shallow coastal environments. Indeed, water and sediment temperature dynamics are a first order control of many physical and biological processes in aquatic ecosystem, driving the short and long term evolution of the ecosystem.
Given the scarcity of studies and data from the literature that investigate in particular the heat fluxes at the sediment-water interface (SWI), we conceived and performed an ad hoc, one-year-long field campaign was performed in the Venice lagoon to collect water and sediment temperature data. The collected data show that, in our study site, temperature is uniform within the water column, and enabled us to estimate the net heat flux at the sediment-water interface. Based on these results we developed a "point" model for describing the temperature dynamics of the sediment-water continuum in shallow tidal environments. Modeling the flux at the SWI as the sum of a conductive component and of the solar radiation reaching the bottom, we found the latter being negligible. Our analysis further revealed that, in general, horizontal advection driven by tidal currents is an important process also at our study site despite we placed it quite close to a divide. For applying the "point" model we therefore selected, in our data set, only periods when advection is negligible, that correspond to periods characterized by neap tide and small temperature difference between sea and lagoon. The results we obtained following our numerical approach are quite satisfactory showing the capability of the model of reproducing, in the selected conditions, the temperature dynamics both in the water column and within the sediments. Both the analysis of the data and model results show that the heat exchange between water and sediment is crucial for describing sediment temperature but plays a minor role on the water temperature. This observation suggests that, as a first approximation, the water temperature dynamics can be modeled neglecting the heat exchange between water and sediments.
Using the developed numerical model we further investigated the effect of different turbidity conditions of the water column on the water and sediment temperature and on the photosynthetic capacity of the microphytobenthos (MPB), i.e. communities of microalgae commonly present in coastal environments and colonizing the uppermost layer of bed sediments. We found that the water temperature dynamics is poorly affected by the different conditions investigated, while the sediment temperature variation is significant,

especially for very shallow water depth (i.e. $\leq 0.5\ m$). Considering the average annual budget, the photosynthetic rate of the MPB is found to be better promoted by clear water conditions, being the light availability the major limiting factor for the photosynthetic process. These results suggest the possibility of investigating a positive feedback between water column turbidity and the MPB proliferation, driven by its photosynthetic capacity. In fact, the abundance of MPB provides a bio-stabilization of the sediment bottom, creating a biofilm that limits sediment resuspension and thus reduces the water column turbidity.

Acknowledgments

The last three years have been so busy and dense that I can not believe my period as a Ph.D. student has already finished. Sometimes it has been tough, but in the end it has been a great experience, and I would like to thank the University of Padova for the privilege of having been a PhD student of the PhD school in Civil and Environmental Engineering Sciences.

But most of all I want to thank all the people I have been lucky enough to work, live and spend time with, because thanks to them I will bring with me so many good memories of this journey.

First, a special thanks must be given to my supervisor Luca Carniello, a great scientist but most of all one of the kindest human being I have ever met. You always encouraged and helped me with my research, you believed in me and made me feel comfortable, but most of all you have been a good friend. I hope you enjoyed working with me as much as I did.
I would also like to thank my co-advisors Marco Marani and Sonia Silvestri for their useful suggestions and the kindness they have always shown me.
I wish to thank also the director of the Ph.D. school Stefano Lanzoni for the attention shown, in his way, to me and my colleagues.

A special thanks to all the guys I had the pleasure to share the office with: Alessandro, Arianna, Chiara, Gigi, Giulia, Gianluca, Irma, Laura, Manuel, Mara, Marta, Riccardo M., Riccardo T., Sergio, Silvia, Tommaso, Valentina. I can't find the right words to explain all my gratitude for the time we spent together, we shared moments of frustration and anger, but most of all we shared so many laughs and great times! All of you gave me something that I will remember with joy, and I think I am not wrong in considering the most of you as true friends! In particular, I want to thank Sergio, who crossed the ocean to share this journey with me and became a good friend of mine, and Gigi, who has been one of my best friends for ten years now.

Of course I can not forget all the "guests" who have been for a while in our office during the last three years. I want to thank John, Alfonso, Fateme Lucia and Enrico, each one of you has become "one of the office" and left us great memories.
In particular, I want to thank John for the needful help he provided with my

work, but mostly for the beers and the fun we shared!

One of the things that I will never forget about my PhD is the time I spent abroad, at the University of Virginia and at the University of California, Berkeley. I had great times there and visited many beautiful places, but most of all I had the pleasure to meet and know many wonderful people.
First of all, I have to thank Paolo D'Odorico, my supervisor during the period I spent there. There is no need to waste words about you as scientist, I knew I was going to work with a great professor, but I could not expect you were also such a nice person. I could not ask for two better supervisors than you and Luca. Thank you for everything.
I want to thank all the people I met at the International Center in Charlottesville, especially Carol who has been my company during the Christmas holiday, and Shradda, who shared the office with me during my short stay at the UVA.
A huge thanks to Huang, Lorenzo and Mo (my man!), my office-mates and friends in Berkeley. You made every day I spent there enjoyable, and I wish you the best for your PhD.
And what to say about the house at 2725 Dohr St? I have to thank all the people who live or used to live there: Tim, Sheryl, Princy, Tom, Sean, Malgosia, and most of all Giovani, Choryi, Tito, Paul and Evan, my amazing room-mates. I had just a tiny room there, but it was all I needed because you made me feel at home. And of course thanks to Misty, my furry friend with whom I shared my bed many times.

A special thanks to all my friends, I could not go on without the laughs, the fun and the joy you give me. Thank you for being such a crazy set of people.

I want to thank my parents, Antonio and Antonella, for their never ending support and for believing in me more than I believe in myself. Even if we are different and sometimes we don't understand each other, I know you are always there for me.

Finally, a very big thanks goes to my girlfriend Elisa. You are the only one who really has to deal with the negative side of my character, but still, after ten years, you want to stay by my side and you make me feel loved. I think you are crazy... I love you!

Probably I am forgetting someone, I am sorry but too many things happened during the last three years. Anyway, thank you!

Contents

Chapter 1

Introduction

The coastline separating continents from oceans consists of many different environments (e.g. bays, estuaries, lagoons, deltas), and represents one of the most productive areas of the world (Martínez et al., 2007). Coastal environments are suffering and their ecosystems are at risk because of the increasing anthropogenic pressure and the accelerated global nitrogen cycle promoting the eutrophication (WRI, 2005). About half of the world's population live along the coastline (PRB, 2012), inevitably stressing coastal environments. The reduction of sediment supply from rivers (also related to human interventions) and the increased pollution are causing a degradation of shallow water environments, that brought to the disappearance of half of the world's wetlands and mangroves in the last century, and deteriorated nearly the 60% of the world's coral reef (FAO, 2001).

Lagoons represent one of the typical environments along the coastline, occupying almost the 15% of the world's shoreline. Lagoons play a crucial ecological role, providing the perfect habitats for many animal and plant species and rates of primary productivity comparable to that of rain forests, representing hot-spots of carbon-cycling and therefore working as regulators of climate change (Cronk and Fennessy, 2016). Typically, many socio-economic interests are connected to coastal lagoons, leading to intense human stress on these environments that causes losses of ecosystem goods and services.
Considering the increasing anthropogenic pressure on lagoons and coastal areas, proper methods for monitoring the water quality must be developed, in order to manage a sustainable utilization of the water resource and of the environments, and to better control and describe the eco-bio-morphodynamic

processes driving the evolution of the ecosystem.

Water and sediment temperature dynamics are a first order control of physical and biological processes affecting the dynamics of water quality in aquatic ecosystems in general, and in coastal systems in particular. Organic matter production and decomposition rates in the sediment-water continuum is directly linked with temperature, and thus greenhouse-gases (chiefly Carbon Dioxide and Methane) emission and uptake (Battin et al., 2009). Dissolved oxygen level is also function of water temperature, with lower values of saturated dissolved oxygen observed at higher water temperatures (Lee and Lwiza, 2008), possibly leading to hypoxia (i.e. depletion of dissolved oxygen below $2 \div 3\ mg\ l^{-1}$) and therefore to relevant disturbances of the ecosystem (Kemp et al., 2005). This phenomenon typically affects shallow water basin located in temperate coastal regions (Hearn and Robson, 2001; Hagy et al., 2004). The temperature dynamics in the water column and within the sediment controls water transparency (Williamson et al., 2009) and drives biological processes, especially in semi-enclosed environments, such as lagoons and estuaries, often characterized by long residence times (Viero and Defina, 2016). Water transparency and therefore the light transmittance trough the water column represents also one of the major factors responsible for the loss of seagrass coverage (Carr et al., 2010, 2015). Temperature at the sediment-water interface is a crucial factor influencing the growth and survival of microphytobenthic biomass (Guarini et al., 2000), while temperature in the underlying sediment layers affects biochemical kinetics and the recycling of nutrient and toxic materials within the sediment column (Fang and Stefan, 1998). Controlling the microphytobenthic biomass growth, the temperature at the sediment-water interface indirectly affects the morphodynamics of the tidal environments because of the stabilizing effect of the biofilm produced by the microphytobenthos on the sediment surface (Paterson, 1989; Miller et al., 1996).
Water temperature variations related to climate change or local thermal pollution also creates suitable conditions for alien algal species to grow, leading to environmental alteration and possible reduction of the native sea flora (Gritti et al., 2006; Wolf et al., 2014).

1.1 Microphytobenthos

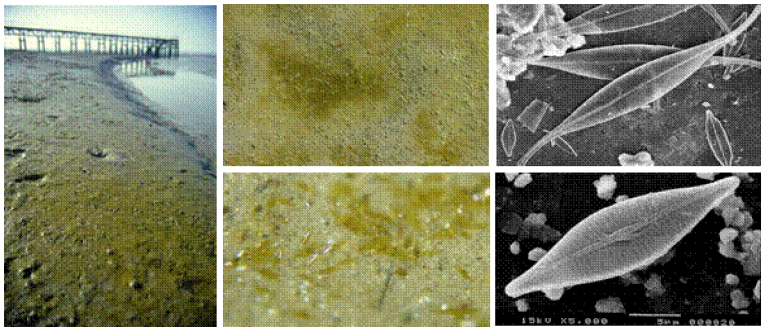

Figure 1.1: Biofilms of benthic microalgae, or microphytobenthos (MPB), growing on the sediment surface in intertidal flats.

The microphytobenthos (MPB) (figure 1.1) consists of microscopic, eukaryotic algae and cyanobacteria typically present in coastal environments, including habitats like salt marshes, intertidal and tidal flats characterized by light availability (MacIntyre et al., 1996), but also in shallow lakes and rivers (Cochero et al., 2014).
The role played by the MPB is crucial for the ecosystems. In fact, benthic microalgae are one of the major factors driving primary productivity in shallow coastal environments, concurring significantly to carbon intake and oxygen and nutrients production, and constitute also a food source for secondary producers (Miller et al., 1996).

The benthic biomass is distributed along the first centimeters of sediments. The small fraction of biomass located within the photic zone (i.e. the very first layer of sediments characterized by light penetration) constitutes the "photosynthetically active layer", which, at a given time, actively participates to the productivity (Guarini et al., 2000). The vertical distribution of the MPB biomass is due both to physical and biological processes and to the inner motility of the MPB. In fact, the microalgae can migrate downward under high light condition, to avoid photoinhibition, and upward under low/medium light condition to enhance the photosynthetic process.
The benthic biomass growth and the related primary productivity of the MPB is driven by four major factors: light availability, sediment temper-

ature, nutrients concentration and sediment transport (Barranguet et al., 1998). Usually, the nutrients availability is not a limiting factor in environments characterized by the presence of MPB, while sediment temperature and light are the most important constrains (Du et al., 2016).

The benthic communities not only plays a crucial role for the primary productity, but also importantly affects the short and long term morphodynamic evolution of the environments where they prolifer (Kirwan and Murray, 2007; Marani et al., 2010) and therefore the characteristics of the ecosystem. The abundance of MPB at the bottom provides a stabilizing effect on the sediment surface (Paterson, 1989; Paterson and Black, 1999; Black et al., 2002). Benthic diatoms, in fact, produce extracellular polymeric substances (EPS) creating a biofilm on the sediment surface that, increasing the critical threshold for erosion, reduces the sediment resuspension and the bottom erosion (Parsons et al., 2016). The EPS distribution profile varies in time as function of the biofilm growth and "age", affecting progressively deeper layers of sediments. Therefore, the biostabilization provided by the EPS structure varies in time, and as the biofilm grows the sediments resistance to erosion increases at greater depths within the bed (Chen et al., 2017). The structure of the biofilm produced by the MPB depends also on the flow regime at the bed surface (Wang et al., 2014), with stronger structures observed when higher flow velocities affect the bed surface. The interaction between MPB and morphodynamics is therefore crucial, and provides a good example to support the necessity of an eco-bio-morphodynamic approach in the study of coastal environments.

1.2 Temperature Dynamics in Aquatic Enviroments

Water and sediment temperature dynamics in aquatic systems is driven by the sum of different energy fluxes, potentially small compared to the single contributions (Imboden and Wuest, 1995).
Process-based energy balance models (Fang and Stefan, 1996; Martynov et al., 2010; Subin et al., 2012) are based on a physical description of radiative, conductive, and advective energy transfer within the water-sediment continuum, accurately characterizing the different energy fluxes driving the

temperature dynamics. Calibrating and running these models require accurate time series of meteorological data as input (e.g., air temperature, humidity, wind speed, cloudiness, etc.), which are often not available thus limiting their applicability.
In order to overcome this limitation, regression models (Sharma et al., 2008; Cho and Lee, 2012) and semi-empirical models (Kettle et al., 2004; Piccolroaz et al., 2013) are an alternative. While the purpose of process-based models is to fully represent the process of interest, regression and semi-empirical models provide a simplified representation, with the advantage of requiring less data as input. In particular, regression models identify the main parameters to consider as predictors of the process and provide a formulation based on a statistical approach (i.e. linear regression, Bayesian multiple linear regression); semi-empirical models, instead, provide a parameterized description of the process based on physical principles. Both these type of models have been successfully applied to different environments as rivers (Morrill et al., 2005; Toffolon and Piccolroaz, 2015), lakes (Kettle et al., 2004; Piccolroaz et al., 2013, 2017) and bays (Cho and Lee, 2012). Regression and semi-empirical models are typically applied for long-term analysis (seasonal to multi-annual timescale) because of the simplicity, parsimony and computational efficiency. The applicability of regression models is theoretically limited to the range of variation of data used for the calibration, while semi-empirical models can be applied when it is necessary to extrapolate beyond the limit of the measured time series because of their physically based derivation. Therefore, semi-empirical models represent the preferable choice for climate change studies. On the other hand, unlike process-based models, both regression and semi-empirical models do not allow to investigate separately the processes involved in the energy balance and to estimate the short-term (sub-daily) evolution of the temperature dynamics.

1.3 Research Goals

To our knowledge, few studies have investigated the water temperature dynamics and energy balance in shallow coastal environments (e.g. Umgiesser et al. (2004); Bouin et al. (2012)). Even fewer studies focus on the description of energy exchanges at the sediment-water interface. Heat exchange at the sediment-water interface was studied in coastal regions to describe temperature evolution in bed sediments (Guarini et al., 1997; Smith, 2002),

but without fully solving for the two-way coupling of sediment-water energy fluxes. The mutual interaction between water and sediment temperature was studied in lakes with the aim of investigating the effect of the water on the underlying bed sediment temperature (Fang and Stefan, 1996; Boike et al., 2015) and the hypolimnion warming induced by seiche oscillations (Kirillin et al., 2009; Nishri et al., 2015), in relatively deep waters and in the absence of tidal fluctuations.

The aim of the present study is to investigate the evolution of the temperature profile in the water-sediment continuum in a very shallow tidal environment characterized by a temperate climate. In particular, we aim at analyzing, observationally and numerically, the temporal variation of the vertical temperature profile within the water-sediment continuum, with particular attention to the energy flux exchanged at the sediment-water interface (herein after SWI) and its relevance for modeling the water temperature dynamics.

Our analysis focuses on the Venice lagoon (Italy), a significant example of lagoonal environment because of its ecological, socio-economical and historical relevance. We performed a field campaign on a tidal flat within the Lagoon in order to collect temperature data at several points in the water column and within the sediment for about one year. Such an almost unique data set allowed us to investigate the dynamics of the temperature profile within the water-sediment continuum. Observations were used to compute the heat flux at the SWI and interpreted using a "point" model developed for describing the time evolution of the vertical temperature profile. The "point" model is based on a process-based approach, which enabled us to compute separately the different components of the energy balance. The heat exchanged at the SWI was compared with the computed energy fluxes at the air-water interface (herein after AWI) in order to understand its relevance compared to the other vertical energy fluxes.

The "point" model, applied to a synthetic condition, allowed us to further investigate the possible effect of the water column turbidity/light trasmittance on the water and sediment temperature dynamics and consequently on the photosynthetic capacity of microphytobenthos.

Chapter 2

Study Case - the Venice Lagoon

The Venice lagoon, located in the Northeast of Italy (see figure 2.1), is famous worldwide for its historical relevance, mainly related to the presence of the city of Venice, which we can address as an "open-air" museum because of its uniqueness and because of the history and beauty told by its monuments and buildings. Moreover, besides Venice, many other sites within the Lagoon, maybe less known, deserve to be mentioned because of their historical and artistic relevance, like the islands of Murano and Burano and the city of Chioggia.

But the importance of the Venice lagoon is not limited to its artistic and historical characteristics. In fact, the Lagoon represents also a very dynamic ecosystem, characterized by the presence of very different natural environments.
Today, the Venice lagoon extends over a surface of about 550 km^2, bordering an area approximately 50 km long and 8 km wide. A thin littoral border 60 km long separates the Lagoon from the sea. Three inlets (i.e. Lido, Malamocco and Chioggia inlets) interrupt this littoral border, ensuring a connection with the Adriatic Sea. The mean depth characterizing the Lagoon is about 1.2 m, with a typical tidal range of 1.0 m and a main tidal period of 12 h.
The Lagoon consists of various environments like salt marshes, tidal and intertidal flats, fishing farms, lagoonal channels and islands (both natural and artificial). This multitude of environments leads to a very peculiar ecosystem, hosting the perfect habitats for various animal and plant species, as well as bird migratory fluxes of global relevance.

The Venice lagoon that we can appreciate today is the result of a long evolution lasted thousands of years (D'Alpaos (2010), Gambolati and Pietro Teatini (2013)).
Its origin is due to fluvial detritus transported to the sea by the rivers and distributed along the coast by waves and sea currents during the period of stabilization of the Adriatic Sea, constituting the littoral borders of the "first" Lagoon. The early Lagoon was different from the today's Lagoon, smaller and connected to the sea by many inlets. Many rivers (e.g. Brenta, Sile, Piave) used to flow into the lagoonal basin, creating a brackish environment characterized by a lower salinity compared to the connected Adriatic Sea. The rivers flowing within the Lagoon were also responsible of huge amount of sediments supply to the Lagoon, higher than the erosion capacity of the tidal currents within the basin, that would have brought the Lagoon itself to disappear becoming a marshland.

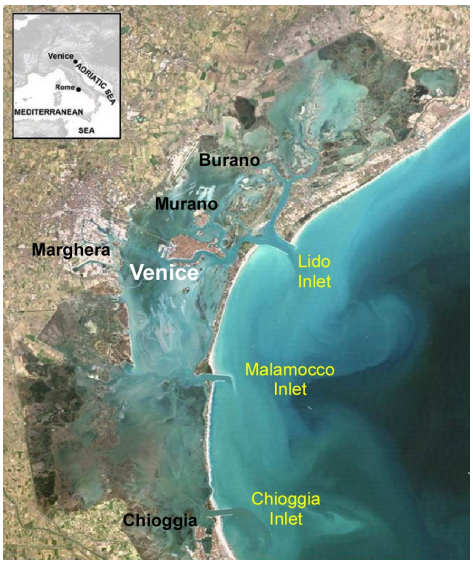

Figure 2.1: Satellite image of the Venice lagoon.

But the location of the city of Venice, in the middle of the Lagoon, ensuring protection either on the land and on the sea side, was strategical for the Venetian State. Therefore, since the *XVI* century, massive interventions have been promoted and realized in order to avoid the disappearing of the characteristic lagoonal features. In particular, the main rivers flowing into the Lagoon have been diverted, drastically reducing the sediment poured into the water basin. Moreover, artificial channels were excavated and the inlets were modified in order to facilitate the navigation. Because of these interventions, the Lagoon faced a dramatic change in time: the reduction of sediment supply and the increased erosion driven by the modified hydrodynamic regime of the Lagoon lead to the retreat of the salt marshes and the lowering of the tidal and intertidal flat bottom. The result is a lagoonal

environment less brackish and characterized by more sea-like features (e.g. increased salinity, higher tides).
During the *XXth* century, the Lagoon modifications due to man interventions and activities have been even more relevant, and the anthropogenic pressure on the ecosystem increased. Deeper navigation channels have been excavated in order to allow the navigation within the Lagoon of bigger ships, new industrial and urban areas have been constructed reclaiming surface occupied by salt marshes and intertidal flats. Moreover, the extraction of subsurface water have increased significantly the lowering of the land level due to subsidence, inducing a much greater effect than in condition of natural sinking. The large industrial area of Marghera was built in the '50-'60s in order to promote the economy of the area, decayed because of the location of Venice that, strategical in the past, became a major limitation in the modern days. However, the industrial area and the industrial waste produced represents a new source of stress for the lagoonal ecosystem.

The history of the Venice lagoon and its strong relationship with the human activities makes the Lagoon a perfect example of the interconnections between natural and built environments, and the delicate equilibrium for a sustainable use of the natural resource. Climate change and related sea level rise, subsidence of the bottom and the anthropic pressure on the environments are threatening the ecosystem of the Lagoon, affecting its eco-bio-morphodynamic evolution. The main environmental issues are the progressive reduction of the main morphological structures of the lagoonal environment, i.e. salt marshes and tidal flat, and the lagoon water quality.

In the last 100 years a reduction of about the 40% of the salt marshes area and a 30% increase of the mean water depth has been observed, reinforcing the erosional trends by increasing the mean fetch and depth of the flows (Carniello et al. (2009), Molinaroli et al. (2009), D'Alpaos (2010)). The modified hydrodynamics and the increase sediments erosion and resuspension significantly affects also the water quality, spreading the pollutants accumulated in the Lagoon's sediments. The main sources of pollution are the high nutrient load from water inflow, associated with agricultural activities and residential waste, and the industrial waste produced by the activities in Marghera. The industrial estate of Marghera is also responsible of a sensible thermal pollution, leading to an increase water temperature in the surrounding area that creates suitable condition for the proliferation of alien algal species with possible degradation of the local ecosystem (Wolf et al. (2014)).

The damages on the ecosystem caused by pollutants are worsened by the high residence time of water, that in the inner parts of the Lagoon can be of 12 days (Viero and Defina (2016)).

Giving the increasing anthropogenic pressure, a multidisciplinary approach, integrating satellite data, *in situ* water quality data, and mathematical-physical models, is needed for studying and monitoring the Venice lagoon, as well for others lagoons and coastal areas, in order to couple biological, ecological and hydrodynamic processes and understand the short and long term evolution of these environments and how we can preserve them.

Chapter 3

Field Measurements and Data

The main goal of the present study is to investigate the time evolution of the temperature profile of water-sediment continuum and the role of the heat exchange at the sediment-water interface (SWI) on the water column temperature dynamics.

In pursuing this goal we conceived and performed, in cooperation with the Duke University (US), a field campaign in the Venice lagoon, a very shallow tidal environment characterized by a temperate climate. The Venice lagoon represents an example of well monitored coastal environment, characterized by the presence of an efficient monitoring network. However, temperature data describing the temperature profile within the water-sediment continuum were not available.Thus, the field campaign we performed provided an almost unique dataset.
During the field campaign we collected water and sediment temperature data in a tidal flat within the Lagoon. During the same field campaign we collected also temperature data over a salt marsh but those data have not been used in the present study.

Meteorological data necessary to compute the energy fluxes at the air-water interface (AWI), as well as tidal oscillation data, were obtained from the monitoring network of the Venice Municipality.

3.1 Study Site

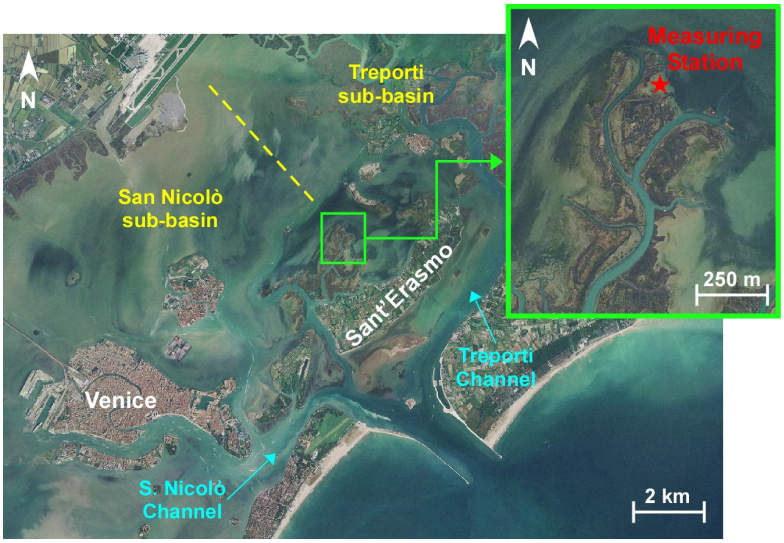

Figure 3.1: Satellite image of the portion of the Venice lagoon close to the Lido inlet. The yellow dashed line shows the position of the divide between the sub-basins of San Nicolò and Treporti. The green box highlights the position of the study site where the field measurements campaign was performed. The position of the measuring station is identified by the red star in the enlargement of the stidy site area.

We installed the measuring station in a shallow tidal flat in the northern part of the Venice lagoon, close to the island of Sant'Erasmo (see figure 3.1), during the period between July 2015 and May 2016.
We choose this study site for the following reasons:

- bathymetric and morphological information of the area were already available from previous works (Bendoni et al. (2016));
- the study site is quite close to the divide between two sub-basins of the lagoon (Solidoro et al. (2004), D'Alpaos (2010)), i.e. areas to/from which sea water is transported along different paths (through the Treporti channel and the San Nicoló channel). This position implies that water advection in the area is, in general, limited (flow through the boundary being theoretically equal to zero), as well as the associated

energy exchange with surrounding areas. The location close to the divide was selected in order to make as much realistic as possible the hypothesis of neglecting the contribution of the horizontal advection and therefore the possibility of modeling the local temperature dynamics using a simplified 1-D (vertical) approach;

- the study site can be reached quite easily from Venice, making possible to periodically visit the measuring station in order to change the batteries and check the status of the instruments.

The bottom elevation at the measuring station is 0.65 m below mean sea level, and the local tidal range is about 0.80 m during a spring tide and 0.50 m during a neap tide. Therefore, the tidal flat is almost permanently submerged, except for rare meteorological conditions. In fact, the tidal flat emerged only once during the almost one year monitoring period, and only for few hours.

3.2 Measuring Station

The measuring station consisted of 9 temperature sensors, deployed in the sediment at depths of 5, 10, 25, 50, 100 and 150 cm below the sediment surface and in the water column at 10, 40, 70, 100 cm above the sediment surface. The temperature sensors were fixed to a steel pipe, properly positioned in order to measure the water and sediment temperature at the desired depths once the pipe was stuck in the tidal flat. The temperature sensors in the water column were variably submerged by water depending on the local tidal elevation, measured by a pressure transducer (U20 HOBO Onset, Massachusetts, USA) positioned on the sediment bed surface.

The digital temperature sensors have an accuracy $+/-$ 0.5 $°C$ with a logging resolution of 0.0625 $°C$ (ControlByWeb, Xytronix Inc. Utah, USA) and were connected to an Arduino Pro 328 microcomputer, with a data logging shield (Adafruit, New York, USA). All data were collected at five minutes intervals. The data logger and sensors were powered by sealed lead acid batteries. Data logger and batteries were contained in a waterproof box, positioned on the top of a PVC pipe stuck in the sediments next to the steel pipe to which the temperature sensors were attached. The schematic of the

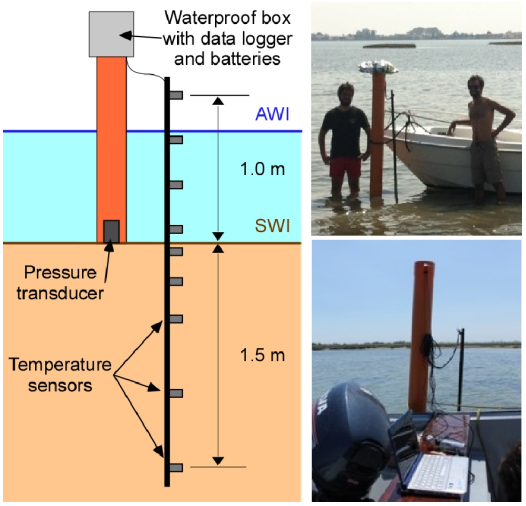

Figure 3.2: Scheme of the measuring station installed in the tidal flat for the almost 1-year-long field campaign performed. The pictures show the measuring station and the data collection activity performed at regular intervals.

measuring station is shown in figure 3.2.

The duration of a battery charge is temperature-dependent, and was the cause of some missing data. Over a period of 318 days (from the 17^{th} of July 2015 to the 31^{st} of May 2016), we collected data for 134 days, with continuous data-records that are all longer than one week.

The pressure transducer was in operation only during the first month of the field campaign. Water level data from this period were related to the tidal observations recorded at Burano by a tide gauge of the Venice Municipality monitoring network. Tidal levels from the Burano station were then used for the remainder of the data collection window.

3.3 Meteorological Data

The meteorological data necessary to compute the heat fluxes at the AWI are solar radiation (R_{sun} $[W\ m^{-2}]$), air temperature (T_{air} $[°C]$), relative humidity (H_{rel} $(\%)$), atmospheric pressure (p_{atm} $[mbar]$), wind speed (V_{wind} $[m\ s^{-1}]$) and cloudiness (N $(\%)$).

Except for cloudiness, meteorological and tidal elevation data (h $[m]$) were obtained, with a 5-minutes resolution, from the Venice Municipality through its Tidal Forecast and Alert Center. The Venice Municipality Monitoring Network further provided the sea water temperature (T_S $[°C]$) measured at the off-shore CNR platform, that we used to observe the temperature difference between the water at the measuring station inside the Lagoon and at the sea.

Table 3.1 lists the monitoring stations considered for each input quantity. The location of the different stations is shown in figure 3.3. Air temperature and relative humidity are measured at 14 m above the mean sea level at the measuring station of Palazzo Cavalli, while the wind speed is measured at 9 m above the mean sea level at the measuring station of Laguna Nord, where the wind regime can be considered characteristic of the entire northern part of the Lagoon (Carniello et al. (2012), Carniello et al. (2014)). The

Station	**Coordinates**	**Variables**	**Sensor Elevation**	**Unit**
San Giorgio	$45°25'42.27"N$ $12°20'46.55"E$	R_{sun}	12 $[m]$	$[W\ m^{-2}]$
Palazzo Cavalli	$45°26'11.16"N$ $12°20'0.73"E$	T_{air} H_{rel} p_{atm}	14 $[m]$ 14 $[m]$ 10 $[m]$	$[°C]$ $(\%)$ $[mbar]$
Laguna Nord (Saline)	$45°29'44.14"N$ $12°28'19.10"E$	V_{wind}	9 $[m]$	$[m\ s^{-1}]$
Burano	$45°28'58.94"N$ $12°25'03.09"E$	h	3 $[m]$	$[m]$
CNR Platform	$45°18'51.29"N$ $12°30'29.69"E$	T_{sea}	/	$[°C]$

Table 3.1: List of the measuring stations of the Venice Municipality Monitoring Network considered in the present study and measured variables.

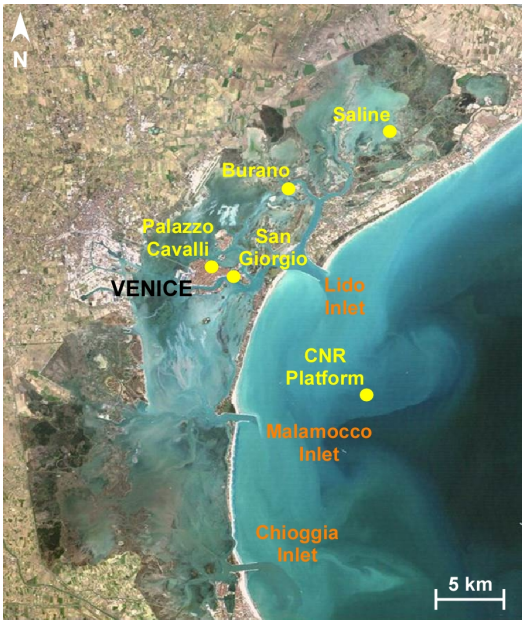

Figure 3.3: Satellite image of the Venice lagoon showing the position of the measuring station (yellow dots) of the Venice Municipality Monitoring Network that provided the meteorological data necessary for the present study.

solar radiation transducer measures all the solar radiation spectrum, with a measuring range of $0.3 \div 3$ μm. More information about the monitoring stations and the monitoring network can be found at the Venice municipality website (*Cittá di Venezia* (2017)).

As anticipated, we used tidal level observations from the Burano station, the tide gauge closest to our study site, to complement local water depth observations. The comparison of the tidal levels measured at the two locations during the first month of the field campaign (when the pressure transducer was deployed) showed consistent values, with a lag of 5 minutes (i.e. the tidal signal reaches the Sant'Erasmo station 5 minutes before it reaches the Burano station). More precisely, the root mean square error between the tidal signal computed using the pressure data and the signal measured at Burano anticipated of 5 minutes is $\approx 0,01$ m, while the value of the Pearson's linear correlation coefficient is ≈ 1, indicating an almost perfect agreement. This

information was used to ensure that tidal level values at the study site could be reconstructed during the entire campaign.

Hourly information on cloud cover obtained from model simulations (Mesinger et al. (2012)) were provided by the forecasting service *IlMeteo* (2017). Fractional cloud cover is computed as a weighted average over the cloud cover values at different heights.

3.4 Observations on the recorded data

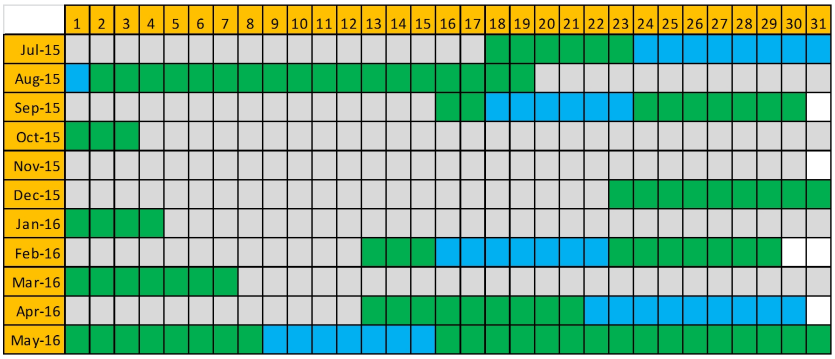

Figure 3.4: Periods when continuous measurements are available (in green and blue) during the almost 1-year-long measuring campaign. Periods characterized by negligible effect of advection (see section 6.1) are highlighted in blue.

The almost one-year-long temperature dataset contains gaps, due to the variable duration of the batteries, but continuous data records are all longer than one week, the longest stretches being longer than one month (see figure 3.4). We were thus able to investigate temperature changes over time scales from minutes to seasons.

Figure 3.5 shows the time evolution of the temperature vertical profile during a summer (figure 3.5(a)) and a winter (figure 3.5(b)) day.
In both cases we notice that:

- water temperature is uniform within the water column (observation

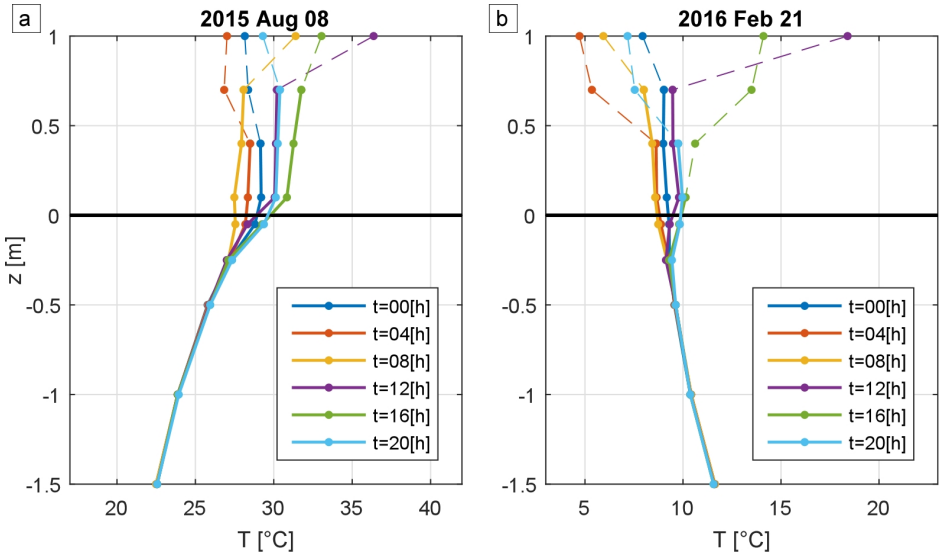

Figure 3.5: Vertical temperature profiles of the water-sediment continuum at different hours of a summer (a) and a winter (b) day. Temperature measured within the water-sediment continuum is indicated by solid lines. Dotted lines show temperature measured by sensors exposed to the atmosphere.

supported also by water temperature measurements collected in previous studies at other locations within the Venice lagoon (MAV (2004))). This is confirmed by figure 3.6, showing the time series of water temperature data measured from the temperature sensors above the SWI at different depths over period of 5 days in summer (figure 3.6(a)) and in winter (figure 3.6(b)). We observe that the measured temperature by the sensors is the same when they are submerged (i.e. when they are measuring the water temperature T_w - solid lines), independently from the sensor position above the SWI, while they become different only when the sensor is exposed to the atmosphere (dashed lines). This observation suggests that the water column is characterized by well-mixed conditions and that the temperature profile within the water column is homogeneous;

- the temperature variation at the daily timescale affects only the topmost $30 \div 50$ cm of the sediments;

- the variations of the sediment temperature over seasonal time scales

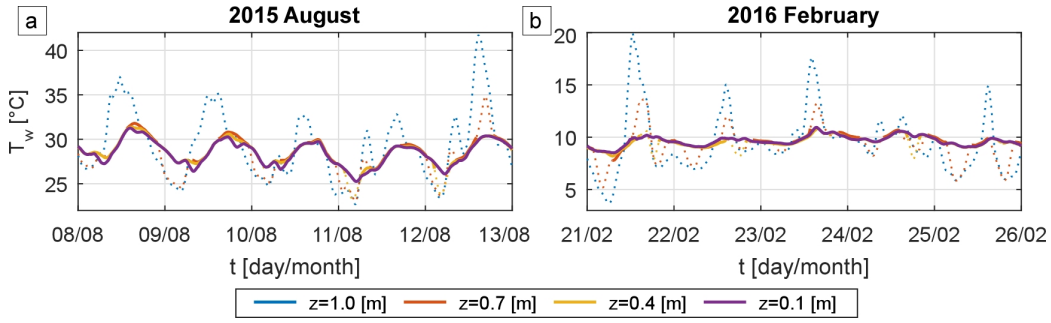

Figure 3.6: Time evolution of the temperature measured by the temperature sensors located at different depths above the SWI for a 5-days-long period in summer (a) and winter (b). The measured water temperature is indicated by solid lines. Dotted lines show the temperature measured by the sensors while exposed to the atmosphere (i.e. the sensor is measuring the air temperature).

affect the entire sediment layer monitored in this study (i.e. first 1.5 m of sediment bed);

- in summer the mean temperature of the sediment is lower than the mean water temperature and therefore the heat flux is on average directed from the water to the sediment, while in winter the opposite pattern is observed.

Chapter 4

Theory and Methods

In the present section we present the theoretical and mathematical framework adopted for investigating the temperature dynamics in the water-sediment continuum, the interaction between water and sediment at the SWI and the energy fluxes at the AWI.

4.1 Water Column Temperature Dynamics

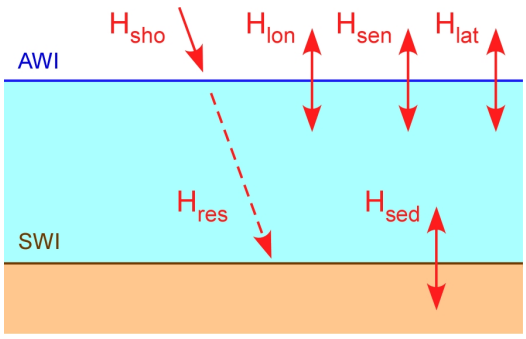

Figure 4.1: Sketch reproducing the vertical energy fluxes at the air-water interface (AWI) and at the sediment-water interface (SWI). Refer to the main text for the meaning and description of the fluxes.

As we discussed in section 3.4, the temperature data we collected during the field campaign, as well as other available field observations, suggest that,

dealing with very shallow water environments like the Venice lagoon, we can consider the temperature uniform within the water column, being the water column characterized by well-mixed conditions.
Therefore we assume a single temperature value to represent the thermal state of the water column, whose dynamics is described by the following equation:

$$\frac{dT_w(t)}{dt} = \frac{1}{C_w(t)} H_N(t) \tag{4.1}$$

where $T_w(t)$ $[°C]$ is the water column temperature, $C_w(t)$ $[W\ s\ °C^{-1} m^{-2}]$ is the thermal capacity of the water column, $H_N(t)$ $[W\ m^{-2}]$ is the net energy flux driving the water column dynamics. The thermal capacity is given by:

$$C_w(t) = \rho_w c_{Pw} Y(t)$$

where $\rho_w = 1027$ $[kg\ m^{-3}]$ is the water density end $c_{Pw} = 3800$ $[J\ kg^{-1} °C^{-1}]$ the water specific heat, both assumed constants, while $Y(t)$ $[m]$ is the water depth at time t.
The net incoming energy flux H_N $[W\ m^{-2}]$ is given by the sum of the horizontal and vertical energy fluxes exchanged by the water column with the surrounding domain.

Focusing on the vertical energy fluxes, the contribution to H_N consists of the following terms (see sketch in Figure 4.1):

- short-wave radiation, H_{sho} $[W\ m^{-2}]$, which is the solar irradiance not reflected by the water surface and partially absorbed by water column according to the Beer's law integrated over the water column height;
- net incoming long-wave radiation, H_{lon} $[W\ m^{-2}]$, which is the difference between radiation emitted by the atmosphere (and fully absorbed by water) and the long-wave radiation emitted by the water column;
- sensible heat flux, H_{sen} $[W\ m^{-2}]$, which is the convective heat flux exchanged at the AWI;
- latent heat flux, H_{lat} $[W\ m^{-2}]$, leaving the water column due to evaporation or entering it due to condensation;
- conductive heat flux at the SWI, H_{sed} $[W\ m^{-2}]$, exchanged between water and sediment because of their temperature gradient.

The energy fluxes at the AWI will be better discussed in section 4.3.

The horizontal energy flux is produced by advection induced by tidal (mostly) and wind currents. For estimating this flux, a bidimensional approach describing the horizontal currents is needed. However, a simple 1-D approach focused on the temperature dynamics driven by only the vertical energy fluxes can be applied if the conditions are such that the advective contribution to the energy balance can be neglected. As discussed in section 3.1, we actually chose our study site in order to limit the relevance of the advective component. Therefore, our purpose is to study the temperature dynamics of the water-sediment continuum and the relevance of the interaction between water and sediment at the SWI applying a simple 1-D approach neglecting the effect of advection.

Knowing the time series of the water temperature T_w and the tidal signal Y, equation (4.1) can be solved also considering as unknown the net energy flux H_N entering/leaving the water column.

4.2 Sediments Temperature Dynamics

The vertical temperature profile within the sediments is described by solving the 1-D heat diffusion equation applied to the sediments, implicitly neglecting the effect of the horizontal fluxes. More precisely, horizontal diffusion can be neglected because of the small horizontal temperature gradient (Fang and Stefan (1998)), while horizontal energy advection can be neglected because of the small values of the sediment hydraulic conductivity typical of these environments (Ursino et al. (2004), Tosatto et al. (2009)).
The 1-D heat diffusion equation describing the sediment temperature dynamics is the following:

$$\begin{aligned} \frac{\partial T_s(t,z)}{\partial t} &= \frac{1}{C_s}\frac{\partial}{\partial z}\left(k\frac{\partial T_s(t,z)}{\partial z}\right) \\ &= \alpha\frac{\partial^2 T_s(t,z)}{\partial z^2} \end{aligned} \tag{4.2}$$

where $T_s(t,z)$ [$^\circ C$] is sediment temperature at time t [s] and depth z [m] below the SWI, C_s [$J\ m^{-3}\ ^\circ C^{-1}$] is the sediment thermal capacity per unit volume,

k $[W\ m^{-1}\ {}^{\circ}C^{-1}]$ is the sediment thermal conductivity, $\alpha = k/C_s$ $[m^2 s^{-1}]$ is the sediment thermal diffusivity. We consider uniform and temporally constant the sediment thermal properties (i.e. C_s, α and k constant in t and z).

Equation (4.2) can be solved using a finite elements method, which enables us to solve the equation imposing as boundary condition (BC) either the temperature (Dirichlet BC) or the heat flux (Neumann BC) at the boundaries of our spatial domain.

Following Piccolo et al. (1993), assuming homogeneous sediments and using available temperature observations within the sediments, we can use equation (4.2) in order to provide a characterization of the sediment thermal properties. In particular, providing the necessary IC and BC, we can estimate the sediment thermal diffusivity α by solving equation (4.2) using several values of α and ascertain the value that maximize the agreement between computed sediment temperature and the available observations at intermediate depths within the chosen spatial domain.

When the upper boundary of our spatial domain coincide with the SWI ($z = 0\ m$), the BC expressed in terms of energy flux consists on the energy flux at the SWI $H_{SWI}[W\ m^{-2}]$. This flux can be calculated using equation (4.2), integrated from a prescribed lower boundary condition (z_{lower}) to the SWI ($z = 0\ m$) and solved considering the energy flux as the unknown (Harrison and Phizacklea (1985)), obtaining:

$$H_{SWI}(t) = C_s \int_{z_{lower}}^{0} \frac{\partial T_s(t,z)}{\partial t} dz + \left(k \frac{\partial T_s(t,z)}{\partial z} \right)_{z_{lower}} \tag{4.3}$$

that, properly discretized, becomes:

$$H_{SWI}(t) = C_s \sum_i \frac{\Delta T_s}{\Delta t}(t, z_i) \Delta z_i + k \frac{\Delta T_s}{\Delta z}(t, z_{lower}) \tag{4.4}$$

where $\frac{\Delta T_s}{\Delta t}(t, z_i)\Delta z_i$ is the heat stored in time Δt within a sediment layer characterized by a thickness Δz_i and a mean depth z_i below the SWI, while $\frac{\Delta T_s}{\Delta z}(t, z_{lower})$ is the temperature gradient a the lower boundary of the spatial domain.
The first term on the right-hand side of equation (4.4) represents the energy stored by the sediment between z_{lower} and the SWI in Δt while the second

term represents the energy flux at the lower boundary.
To compute H_{SWI}, we must know the time series of the sediment temperature at different depths and the sediments thermal properties.

The heat diffusion equation (4.2) describing the sediment temperature dynamics can be solved also analytically. Following Nishri et al. (2015) we can compute an analytical solution of (4.2) for estimating the daily mean temperature profile within the sediments for each day of the year. This analytical solution is:

$$T_s(t,z) = T_0 + T_A \; exp\left[-z\sqrt{\frac{\omega}{2\alpha}}\right] \; sin\left[\omega\,(t + L_d) - z\sqrt{\frac{\omega}{2\alpha}}\right] \tag{4.5}$$

where T_0 $[^{\circ}C]$ is the average seasonal temperature at the SWI (or the constant sediment temperature that one can register deep enough within the sediment bed), T_A $[^{\circ}C]$ is the seasonal temperature amplitude, $\omega = 2\pi/365.25$ $[d^{-1}]$ is the annual angular frequency, α $[m^2\ d^{-1}]$ is the sediment thermal diffusivity, L_d $[d]$ is the phase shift.
Having enough sediment temperatures data to describe the seasonal variation of the sediment temperature at different depths, we can calibrate the values of the parameters T_0, T_A, α and L_d maximizing the agreement between measured temperature and the temperature profile computed using the analytical solution.

4.3 Energy Fluxes at the AWI

As shown in Figure 4.1, the net energy flux at the AWI is given by the sum of four different components: the short-wave energy flux (H_{sho}), the long-wave energy flux (H_{lon}), the sensible heat flux (H_{sen}) and the latent heat flux (H_{lat}). A wide literature exists on the heat fluxes at the AWI and many formulas can be found for estimating the different contributions to the energy balance. Here we present the energy fluxes and the formulas we used to compute them in the present study.
Table 4.1 provides a list of specific quantities necessary for estimating the energy fluxes at the AWI that, for sake of simplicity, are not explicitly discussed in the following sections.

Variable	Expression	Unit
Saturated Vapor Pressure	$e_S = 6.11 \exp\left(17.502 \frac{T}{T+240.97}\right) \cdot \cdot (1.0007 + 3.46\ 10^{-6}\ p_{atm})$	$[mbar]$
Water Vapor Pressure	$e_V = e_S\ H_{rel}/100$	$[mbar]$
Specific Humidity	$q = 0.622\ e_V\ (p_{atm} - 0.378\ e_V)^{-1}$	
Friction Velocity	$u_* = V_{wind}\ k \ln^{-1}(z/z_0)$	$[m\ s^{-1}]$
Latent Heat of Vaporization	$L_v = (2.501 - 0.00237\ T)\ 10^6$	$[J\ kg^{-1}]$
Air Density	$\rho_{air} = p_{atm} \cdot 100\,[H_{rel}\ T_{air}\ \ (1 + 0.61\ q)]^{-1}$	$[kg\ m^{-3}]$

Table 4.1: Formulas providing the quantities required to compute the energy fluxes at the AWI driving the water column dynamics.

4.3.1 Short-Wave Radiation

The short-wave radiation contribution to the energy balance of the water column ($H_{sho}\ [W\ m^{-2}]$) consists in the solar irradiance not reflected by the water surface and absorbed by the water column. Dealing with very shallow water, characterized by well-mixed conditions of the water column, we consider the energy provided by the short-wave component of the energy balance uniformly absorbed and distributed along the water column.
The irradiance absorption by the water column is commonly described as an exponential function (e.g Denman and Miyake (1973)) of the water column height $Y\ [m]$. Therefore, the component H_{sho} of the water column energy balance is computed as:

$$H_{sho}(t) = R_0(t)\,[1 - \exp\,(-\lambda\ Y(t))] \tag{4.6}$$

where $R_0(t) = (1 - A)\ \ R_{sun}(t)\ [W\ m^{-2}]$ is the incident less reflected irradiance at the water surface (where we assume the albedo of the water surface $A = 0.04$), $\lambda\ [m^{-1}]$ is the extinction coefficient (inverse of the attenuation

length).
The extinction coefficient λ is theoretically time variant as function of the water column turbidity, but turbidity data are often not available (like in our case). Therefore, we consider λ constant in time and representative of the average turbidity condition characterizing the considered study site.

4.3.2 Long-Wave Radiation

The net long-wave radiation, as the others surface heat fluxes at the AWI, can be estimated using the so-called bulk transfer formulas. These empirical formulas provide the heat fluxes as functions of measurable quantities, generally available and easy to measure.
The parameters of the bulk formulas need to be properly tested and calibrated in order to obtain a satisfactory description of the heat fluxes.

The net long-wave flux at the sea surface (H_{lon} $[W\ m^{-2}]$) consists in the difference between the atmospheric radiation at the water surface (H_{atm} $[W\ m^{-2}]$) and the infrared radiation emitted by the water body (H_{wat} $[W\ m^{-2}]$):

$$H_{lon}(t) = H_{atm}(t) - H_{wat}(t) \tag{4.7}$$

In literature many empirical formulas to compute the net long-wave radiation are available. In the present study, we decided to use the formula proposed by Bignami et al. (1995). This formula has been determined and tested using direct measurements of infrared heat fluxes collected in the Mediterranean Sea. Therefore we can safely apply it to study the energy budget at our study site (i.e. the Venice Lagoon).
Following Bignami et al. (1995), the two contribution to the net long-wave heat flux are computed separately.
The infrared heat flux emitted by the water body (H_{wat} $[W\ m^{-2}]$) is expressed by the Stefan-Boltzmann law:

$$H_{wat}(t) = \epsilon\ \sigma\ T_w^4(t) \tag{4.8}$$

where $\epsilon = 0.98$ is the water surface emissivity, $\sigma = 5.5576 \cdot 10^{-8}$ $[W\ m^{-2}K^{-4}]$ is the Stefan Boltzmann constant and T_w $[K]$ is the absolute water temperature.
The expression for the atmospheric radiation reaching the water surface

(H_{atm} $[W\ m^{-2}]$) has been developed based on the data collected in the Mediterranean Sea. This contribution is computed as:

$$H_{atm}(t) = \sigma\ T_{air}^4(t)\ \left(0.653 + 0.00535\ e_V(t)\right)\ \left(1 - 0.1762\ N^2(t)\right) \tag{4.9}$$

where T_{air} $[K]$ is the air temperature, e_V $[mbar]$ is the water vapor pressure and N the fraction of covered sky (i.e. sky cloudiness).

4.3.3 Sensible and Latent Heat Flux

The sensible heat flux (H_{sen} $[W\ m^{-2}]$), or convective heat addition or removal from the water surface, represents the heat exchange at the AWI driven by the temperature gradient between air and water (i.e. flux related to conduction) and added to/removed from the AWI by convective air movements.
The latent heat flux (H_{lat} $[W\ m^{-2}]$) represents the loss/gain of energy by the water column due to evaporation/condensation.
Different methods can be applied in order to estimate these fluxes (Smith et al. (1996), Fairall et al. (1997)). In the present study we used the algorithm COARE 3.0 (Fairall et al. (2003)) for estimating both sensible and latent heat fluxes. Such an algorithm has been already applied to compute the surface heat fluxes over a lagoon located along the Mediterranean coast of France (Bouin et al. (2012)), which can be considered representative of a generic coastal lagoon located in the Mediterranean Sea (like the Venice Lagoon).
In particular, we simplified the algorithm considering just neutral condition of the atmosphere and thus neglecting the universal stability functions in the computation of the fluxes. The estimation of the fluxes is based on the mass transfer method. Following this approach, the flux F_x corresponding to the quantity x (e.g. wind speed, temperature or humidity) can be computed as follows:

$$F_x = C_x\ V_{wind}\ (x_z - x_s)$$

where C_x is the transfer coefficient for x, V_{wind} is the wind speed at the height z and x_s, x_z are the values of x at the AWI and at height z.
Therefore, sensible and latent heat fluxes can be estimated as:

$$H_{sen} = C_{sen}\ c_{Pair}\ \rho_{air}\ V_{wind}\ (T_{air} - T_w) \tag{4.10}$$

$$H_{lat} = C_{lat}\ \rho_{air}\ L_v\ V_{wind}\ (q_a - q_S) \tag{4.11}$$

where C_{sen} and C_{lat} are respectively the transfer coefficient for sensible and latent heat fluxes, $c_{Pair} = 1005\ [J\ kg^{-1}{}^{\circ}C^{-1}]$ is the specific heat of air, $\rho_{air}\ [kg\ m^{-3}]$ is the air density, $V_{wind}\ [m\ s^{-1}]$ is the wind speed at the height z, $T_{air}\ [^{\circ}C]$ is the air temperature at the height z_T, $T_w\ [^{\circ}C]$ is the water surface temperature, $L_v\ [J\ kg^{-1}]$ is the latent heat of vaporization, q_a and q_S are the specific humidity at z_T and at the water surface.
Neglecting the stability functions, the transfer coefficients C_{sen} and C_{lat} can be computed as:

$$C_{sen} = k^2 \left(\ln \frac{z}{z_0}\right)^{-1} \left(\ln \frac{z_T}{z_{0T}}\right)^{-1}$$
$$C_{lat} = k^2 \left(\ln \frac{z}{z_0}\right)^{-1} \left(\ln \frac{z_H}{z_{0H}}\right)^{-1}$$

where $k = 0.4$ is the von Kármán constant, z, z_T and $z_H\ [m]$ are the measuring heights for wind speed, air temperature and humidity, z_0, z_{0T} and $z_{0H}\ [m]$ are the roughness lengths associated to wind speed, temperature and humidity.
Following Smith (1988), the roughness length z_0 is computed as:

$$z_0 = \frac{\gamma u_*^2}{g} + \frac{0.11\nu}{u_*} \tag{4.12}$$

where γ is the Charnock parameter, $g = 9.806\ [m^2 s^{-1}]$ is the gravitational acceleration, $u_*\ [m\ s^{-1}]$ is the friction velocity at the water surface and $\nu\ [m^2 s^{-1}]$ is the kinematic viscosity. Following the scheme of the COARE 3.0 algorithm, we consider a variable value of the Charnock parameter γ as a function of the wind speed. In particular, γ is equal to 0.011 for $V_{wind} \leq 10\ m\ s^{-1}$ and to 0.018 for $V_{wind} \geq 18\ m\ s^{-1}$, while increases following a simple linear relation for $10 < V_{wind} < 18\ m\ s^{-1}$.
The roughness lengths z_{0T} and z_{0H} are computed as functions of the Reynolds number $Re = z_0 \frac{u_*}{\nu}$.

Algorithm COARE 3.0 also provides a parameterization of the roughness length z_0 based on the sea state/wave properties. In fact, surface waves affect the surface roughness when wind speed is greater than $5\ m\ s^{-1}$. Therefore, following the relationship provided by Taylor and Yelland (2001) and adding the smooth flow component, the roughness length can be also computed as:

$$z_0 = 1200\ H_s\,(H_s/L_p)^{4.5} + 0.11\nu/u_* \tag{4.13}$$

where H_s $[m]$ is the significant wave height (i.e. mean height of the upper third of the wave height distribution) and L_p $[m]$ is the wavelength of the dominant wave period (i.e wavelength associated with the peak of the wave frequency-size spectrum). This relationship would allow us to exploit information about the sea state conditions when available (e.g. H_s and L_p provided by measuring stations or by numerical model).

4.4 Energy Flux at the SWI

To our knowledge, the interaction between water and sediment at the SWI has not been widely investigated in literature especially in the case of shallow tidal environments.

Considering the sketch of the energy fluxes shown in Figure 4.1, the net energy flux at the SWI, H_{SWI}, can be expressed as the sum of two components:

$$H_{SWI}(t) = H_{sed}(t) + H_{res}(t) \tag{4.14}$$

where H_{sed} $[W\ m^{-2}]$ is the conductive heat flux at the SWI due to the temperature gradient between water and sediment, while H_{res} $[W\ m^{-2}]$ is the residual solar radiation reaching the bottom, not reflected at the water surface and not absorbed by the water column.

We model the conductive component H_{sed} as:

$$H_{sed}\,(t) = \begin{cases} k_1\ \frac{dT}{dz} & \text{when} \quad T_w \geq T_s(t, z=0) \\ k_2\ \frac{dT}{dz} & \text{when} \quad T_w < T_s(t, z=0) \end{cases} \tag{4.15}$$

where k_1 and k_2 $[W\ m^{-1}{}^{\circ}C^{-1}]$ are two model parameters describing the conductive heat flux due to the temperature gradient dT/dz between water and sediment at the SWI. We distinguish the case of flux directed downward (i.e. when water temperature is higher than sediment temperature) and upward (i.e. when sediment temperature is higher than water temperature) in order to consider the possible unstable conditions characterizing the water column that favor the formation of convective cells also responsible for the observed uniform temperature profile.

The residual solar radiation H_{res} is often neglected in models used to describe the water temperature profile (Fang and Stefan (1998)), being usually negligible (e.g. in deep lakes). Dealing with very shallow water depths, or in condition of very clear water, the contribution of H_{res} might become not negligible (Boike et al. (2015)).
We computed H_{res} following the Beer Law:

$$H_{res}(t) = R_0(t)\, e^{-\lambda Y(t)} \tag{4.16}$$

where $R_0(t) = (1 - A) \cdot R_{sun}(t)$ $[W\ m^{-2}]$ is the solar irradiance not reflected by the water surface, A is the water surface albedo, λ $[m^{-1}]$ is the extinction coefficient, representing the capability of the water column to absorb the solar irradiance.
As discussed in section 4.3, λ is time dependent, being function of the water column turbidity (i.e. the solar radiation adsorbed by the water column increases with the water column turbidity). Turbidity data are not available at our study site, therefore we treat λ as a model parameter, looking for the value of λ that better represent, on average, the water column condition.

4.5 Water-Sediment Temperature - "Point" Model

Coupling equation (4.2) describing the temperature dynamics of the water column and the 1-D heat diffusion equation (4.1) applied to the bed sediments, we developed and applied a "point" model for describing the energy transfer through the water-sediment continuum considering reflection, scattering, and absorption of radiative energy, and conduction of heat in the vertical direction. The model reconstructs the water and sediment temperature dynamics as function of the vertical energy fluxes.
As previously discussed, the adopted approach implies the assumption of neglecting advection associated with horizontal currents. The model applicability is therefore limited to periods in which horizontal advection does not play a crucial role for the water and sediments temperature dynamics.

In order to apply the model, we need:

- the water temperature $T_w(0)$ and the vertical temperature profile within the sediment $T_s(0, z)$ at $t = 0$ s to impose as initial conditions (IC);

- the value of the sediment thermal diffusivity α, that we assume constant within the sediments (i.e. homogeneous sediments and constant thermal properties in time).

- the model parameters k_1, k_2 and λ necessary to compute the energy flux at the "internal" boundary represented by the SWI;

- the meteorological data to impose as upper boundary condition (BC), necessary to compute the energy fluxes at the AWI. In particular, the required meteorological input are: solar radiation at the water surface (R_{sun} $[W\ m^{-2}]$), air temperature (T_{air} $[°C]$), relative humidity (H_{rel} $(\%)$), atmospheric pressure (p_{atm} $[mbar]$), wind speed (V_{wind} $[m\ s^{-1}]$), fraction of covered sky (N).

- the sediment temperature at a prescribed depth within the sediments to be imposed as BC at the lower limit of the computational domain.

To impose the correct IC and BC necessary to apply the "point" model, we can use water and sediment data records. In particular, we can use as lower BC the sediment temperature measured by the lowermost sensor within the sediments, and reconstruct the initial temperature profile between the lower boundary and the SWI using sediment temperature measured at intermediate depths (in our case, using the data recorded during the field campaign described in chapter 3, we can use the temperature measured at $z = -1.5\ m$ as BC and observations at $z = -0.05,\ -0.25,\ -0.50,\ -1.00\ m$ to reconstruct the IC) to which we add the initial water temperature (uniform in the water column).

Assuming measured sediment temperature data as IC and BC clearly undermine the possibility of using the model as a predictive tool as these data are typically not available. In order to overcome this limitation, we can use the analytical solution of the heat diffusion equation (4.2) described in section 4.2, which provides an estimate of the mean daily temperature profile within the sediments. This clearly represents an approximation of the actual temperature profile at a certain time, but represents a good alternative when sediment temperature data are not available.
Beside providing a reliable IC for the vertical temperature profile within the bed sediment when temperature data are not available, the analytical solution (4.5) can be used to expand the computational domain to the depth

below the SWI where the sediment temperature is not affected by the seasonal temperature fluctuations (for temperate latitudes and silty-sand sediments typically $z \approx -10\ m$). In this way the BC at the lower limit of the domain can be imposed assuming a constant value for the temperature, approximately equal to the mean annual air temperature for the specific location.

4.6 MPB Photosynthetic Capacity Rate

The microphytobenthos (MPB), as discussed in section 1.1, consists of communities of microscopic algae typical of shallow coastal areas (i.e. estuaries, deltas, lagoons). They play a crucial role for the ecosystem, being one of the major factors driving the primary productivity (MacIntyre et al. (1996)) and providing a bio-stabilization of the sediments surface thus affecting the morphodynamic evolution of the environment (Paterson (1989)).
The proliferation of the benthic biomass is driven by four major factors: light availability, sediment temperature, nutrients concentration and sediment transport (Barranguet et al. (1998)). Nutrients availability is usually a minor problem in coastal areas, therefore the MPB biomass growth is mostly affected by light and sediments temperature (Du et al. (2016)).

As demonstrated by Kingston (1999), photoihnibition is usually not shown by microphytobentic communities. Although experiments showed that MPB exhibit photoinhibition if constantly illuminated (Blanchard and Gall (1994)), the same behavior is not observed *in situ*, because of the capability of the microalgae to move downward, avoiding inhibitory conditions and still photosynthesizing at their best because of these tiny vertical movements.
Therefore, following Jassby and Platt (1976), the photosynthetic rate (P^B $[\mu g\ C\ (\mu g\ Chl\ a)^{-1} h^{-1}]$) of the photosynthetic active biomass at the sediment surface in the absence of photoinhibition can be computed using the equation:

$$P^B = P^B_{max} \tanh\left(H_{res}/E_k\right) \tag{4.17}$$

where H_{res} $[W\ m^{-2}]$ is the light level at the sediment surface (assumed equal to the total solar irradiance reaching the bottom), E_k $[W\ m^{-2}]$ is the light saturation constant, P^B_{max} $[\mu g\ C\ (\mu g\ Chl\ a)^{-1} h^{-1}]$ is the maximal photosynthetic rate normalized to $Chl\ a$.
The parameter E_k can be assumed constant during the year (Blanchard et al.

(1997), while P^B_{max} varies as function of the surface sediment temperature.

In particular, the variation of P^B_{max} as function of the surface sediment temperature is described by the following equation (Blanchard and Guarini (1996)):

$$
\begin{aligned}
&if\ T_{s0}(t) < T_{max}: \\
P^B_{max}(T_{s0}(t)) &= P_{max}\left(\frac{T_{max} - T_{s0}(t)}{T_{max} - T_{opt}}\right)^{\beta} \exp\left[\beta\left(1 - \frac{T_{max} - T_{s0}(t)}{T_{max} - T_{opt}}\right)\right] \\
&if\ T_{s0}(t) \geq T_{max}: \\
P^B_{max}(T_{s0}(t)) &= 0
\end{aligned}
\tag{4.18}
$$

where $T_{s0}(t)$ $[^{\circ}C]$ is the surface sediment temperature. P^B_{max} increases to its maximum value P_{max} $[\mu g\ C(\mu gChl\ a)^{-1}h^{-1}]$ when T_{s0} reaches the optimal temperature T_{opt} $[^{\circ}C]$, while decreases to 0 when T_{s0} exceeds a maximum threshold equal to T_{max} $[^{\circ}C]$. β is a dimensionless shape factor.
The parameters T_{max}, T_{opt} and β are site dependent and constant in time, while P_{max} is site dependent and shows a seasonal variability (Guarini et al. (1997)).

Following Guarini et al. (2000), the photosynthetic rate P^B of the photosynthetic active biomass, multiply by a properly estimated ratio of $C/Chl\ a$, represents the source term of MPB biomass in the equation describing the MPB dynamics of growth and death.
Therefore, we can consider P^B as a good descriptor for the proliferation possibility of the MPB in a certain environment.

4.7 Error parameters

For quantitatively estimating the model efficiency and the results of the calibration procedures, in the present study we used two error parameters, namely the Root Mean Square Error ($RMSE$) and the Nash Sutcliffe model

efficiency coefficient (*N-S*):

$$RMSE = \sqrt{\frac{\sum_{i=1}^{n} \left(X_{mod_i} - X_{obs_i}\right)^2}{n}} \tag{4.19}$$

$$N - S = 1 - \frac{\sum_{i=1}^{n} \left(X_{mod_i} - X_{obs_i}\right)^2}{\sum_{i=1}^{n} \left(X_{mod_i} - \bar{X}_{obs}\right)^2} \tag{4.20}$$

where X_{mod_i} and X_{obs_i} are respectively the estimated and the observed (or based on the observed data) value of the variable of interest, $\bar{X}_{obs}$ is the mean value of the observed variable and n is the number of available data.
The efficiency coefficient provides an estimate of the capacity of the model to represent the process. In particular, the variation range for the coefficient is $-\infty \leq N-S \geq 1$: negative values of $N-S$ indicate that $\bar{X}_{obs}$ is a better predictor than the model while the model efficiency increases as $N-S$ tends to 1.

Chapter 5

Energy Flux at the SWI

To our knowledge, the energy flux at the SWI and the relevance of the water-sediment thermal interaction for the water temperature dynamics is poorly studied in literature, especially considering very shallow tidal environments. In the present chapter we describe how we estimate the energy flux at the SWI on the basis of the sediment temperature records collected during the field campaign in the Venice lagoon (see chapter 3). The contribution of the estimated energy flux to the energy balance of the water column is further compared with the contributions of the energy fluxes at the AWI in order to evaluate its relevance for the water temperature dynamics.

5.1 Sediment Thermal Properties

The first use we made of the temperature data collected during the field campaign is meant to characterize the thermal properties of the bed sediment.

The thermal diffusivity α $[m^2\ s^{-1}]$, assumed uniform within the sediment (i.e. we assume homogeneous bed sediment), was estimated using equation (4.2) as described in section 4.2. In particular, we solved equation (4.2) numerically using a spatial resolution of 2.5 cm and a timestep of 5 minutes. The spatial domain considered in our analysis extends from $z = -1.50\ m$ to $z = -0.05\ m$, depths that correspond to the positions of the lowermost and the uppermost temperature sensors we deployed within the sediment bed. We imposed as IC the measured vertical temperature distribution re-

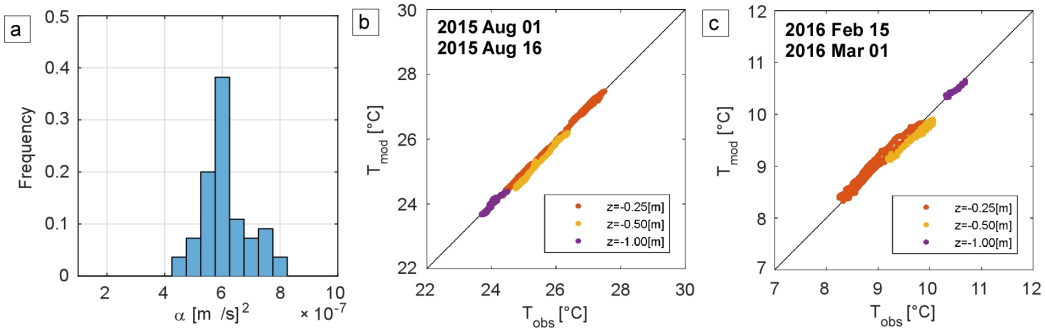

Figure 5.1: Sediment thermal diffusivity characterization: panel (a) shows the frequency of the values obtained from the characterization procedure; panels (b) and (c) show, respectively for a summer and a winter period of 15 days, the scatter plots of the sediment temperature at different depths z observed and computed solving equation (4.2) using $\alpha = 6.0\ 10^{-7}\ [m\ s^{-2}]$.

constructed on the basis of the measured temperature data at intermediate depths and as BC the measured sediment temperature at the boundaries of the spatial domain. We tested 10^4 values of thermal diffusivity α in the range: $10^{-7} \leq \alpha \leq 10^{-6}\ m^2\ s^{-1}$, looking for the value that simultaneously minimize the RMSE between measured and computed sediment temperature data at intermediate depths within the considered spatial domain where temperature data where available. More precisely we minimized the following function FT:

$$FT = \sqrt{\sum_i RMSE^2(z_i)} \tag{5.1}$$

where $RMSE(z_i)$ is the RMSE 4.19 between the measured and computed sediment temperature at z_i, with z_i equal to: $0.25, 0.50, 1.00\ m$ below the SWI.
In our analysis we considered a moving time window of 15 days, identifying for each time window the best value for α.

Figure 5.1(a) shows the frequency distribution of the values obtained for α from the calibration procedure, ranging from $4.7 \cdot 10^{-7}$ and $8.0 \cdot 10^{-7}\ m^2\ s^{-1}$, with a maximum RMSE over all the periods considered of 0.25 $°C$. The frequency analysis of the results clearly suggests that the most appropriate value for characterizing the sediment thermal diffusivity at our measuring station is $\alpha = 6.0 \cdot 10^{-7}\ [m^2\ s^{-1}]$. The estimated value of thermal diffusivity

is coherent with a silty-sand (Kim et al. (2007)), a sediment characterization also confirmed by the geotechnical analysis of sediment cores collected *in situ*.
Solving equation (4.2) using the identified value of $\alpha = 6.0 \cdot 10^{-7}$ $[m^2\ s^{-1}]$ for all the considered periods we obtained a good description of the temperature dynamics within the sediments characterized by a maximum RMSE of 0.3 $[°C]$, as confirmed by the scatter plots between the measured and computed sediment temperature at different depths shown in Figures 5.1(b) and 5.1(c).

Based on the above sediment characterization, we derived from Kim et al. (2007) the following values of thermal capacity per unit volume: $C_s = 3.00 \cdot 10^6$ $[J\ m^{-3}\ °C^{-1}]$, and thermal conductivity: $k = C_s \cdot \alpha = 1.8$ $[W\ m^{-1}\ °C^{-1}]$.

5.2 Energy Flux at the SWI

Once estimated the sediment thermal properties (section 5.1), we computed the energy flux at the SWI (H_{SWI}) from equation (4.4). The available temperature data allowed us to estimate the heat stored by the sediments within the investigated sediment layer, from the SWI to a depth of 1.5 m below the SWI, and the heat flux at $z = -1.5$ m. The sum of these two components gives the net flux at the SWI, H_{SWI}.
Figure 5.2 shows the scatter plots between sediment temperature observed and computed by solving equation (4.2) imposing as upper BC the flux H_{SWI} estimated on the basis of the temperature data. In particular, we solved the equation using a spatial resolution of 2.5 cm and a timestep of 5 minutes, and imposing the measured sediment temperature as IC and as BC at $z = -1.5$ m. The agreement is satisfactory, confirming that the "data based" H_{SWI} correctly represents the energy flux at the SWI.

Then, we used the computed flux H_{SWI} to calibrate the parameters k_1, k_2 and λ of equation (4.14). We performed the calibration considering periods obtained from our data set using a moving time window of 15 days, which enabled us to consider 55 periods. Using the random sampling technique we tested, for each period, 10^6 random combinations of the parameters (Figure 5.3(a) and 5.3(b) provide two examples), looking for the values of the parameters that maximized the efficiency of the model, described by the

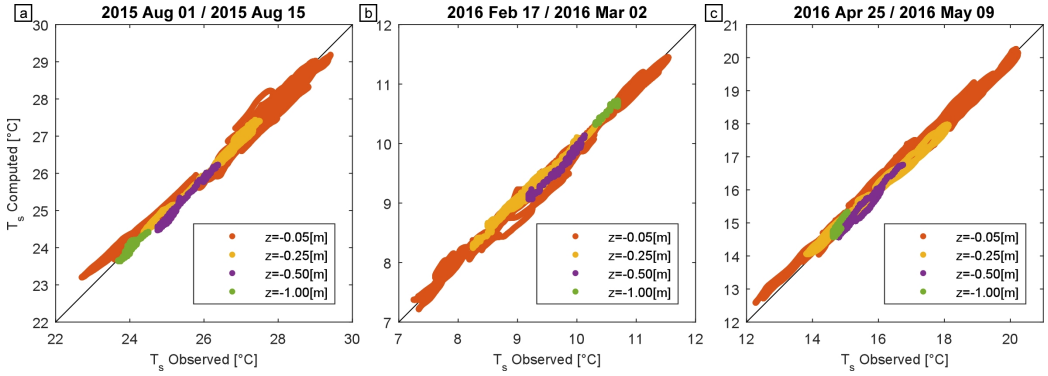

Figure 5.2: Scatter plots of the sediment temperature at different depths observed and computed solving equation (4.2) imposing as boundary condition at the SWI the energy flux H_{SWI} computed on the basis of the available temperature data.

Nash-Sutcliffe coefficient $N - S$ 4.20.

The results of the calibration procedure revealed that the model better reproduces the process in summer and spring ($N - S$ usually greater than 0.75 - see Figure 5.3(a) and 5.3(b)), while on average the values of the coefficient $N - S$ are lower in winter ($N - S$ in the range $0.50 - 0.60$).
We can ascribe this both to the fewer data available for the winter season (see Figure 3.4), which made the calibration procedure less robust, and to the fact that during winter the computed H_{SWI} is lower than in summer and spring and therefore the processes we neglect in our 1D approach (e.g. underground water movement) might become relevant.
Focusing on the summer and spring periods, we performed a frequency analysis of the calibration results. Figure 5.3(c) clearly shows that our analysis identifies different values of k_1 and k_2 for the two seasons, with larger values of both the parameters in spring. This observation seems to suggest a seasonal variation of the parameters, probably due to the different temperature characterizing the sediment and to the different stability conditions of the water column. However, the available data (covering less than 1 year) are not sufficient to confirm and define a clear seasonal trend.

The ratio k_2/k_1 is quite the same for the two seasons and equal to $\approx 1.5 \div 1.75$. This means that, for the same temperature gradient between

Parameter	Unit	Summer	Spring
k_1	$[Wm^{-1}°C^{-1}]$	1.00	2.25
k_2	$[Wm^{-1}°C^{-1}]$	1.75	3.50
λ	$[m^{-1}]$	8	8

Table 5.1: Values of the parameters for equation (4.14) for modeling the energy flux at the SWI provided by the calibration procedure described in section 5.2.

water and sediment, the energy flux directed towards the water is larger than the flux directed toward the sediments. We can ascribe this behavior to the different stability condition affecting the water column, where the convective cells contribute to the column mixing.
The frequency analysis further shows that, both in summer and spring, the best value for the extinction coefficient λ is larger than 7 m^{-1}. This suggests that the water turbidity at our study site is, in general (i.e. not only during storm events when wind waves typically generates high suspended sediment concentration (Carniello et al. (2016))), high enough to absorbs most of the incoming solar radiation and therefore the residual irradiance reaching the sediment surface H_{res} is negligible (i.e. from eq. (4.14) $H_{SWI} \approx H_{sed}$). This also explains why λ seems to be not well identified from the dotty plots in figure 5.3(a) and 5.3(b): in fact, when λ exceeds a threshold (roughly $\lambda \approx$ 6 m^{-1}), H_{res} is negligible and no longer affects the results of the calibration. Our findings are consistent with persistent turbid water column conditions characterizing the Venice lagoon (Carniello et al. (2012), Carniello et al. (2014), Venier et al. (2014)) and very shallow lakes (Subin et al. (2012)).
The values of k_1 and k_2 we selected for modeling the heat flux at the SWI are listed in Table 5.1.

Figure 5.3(d) provides two examples of the capability of equation (4.15), using the calibrated value of k_1, k_2 and λ provided in Table 5.1, of reproducing the dynamics of the heat flux at the SWI for both a summer and a spring period. In particular, in 5.3(d) the flux is positive when directed toward the water column.

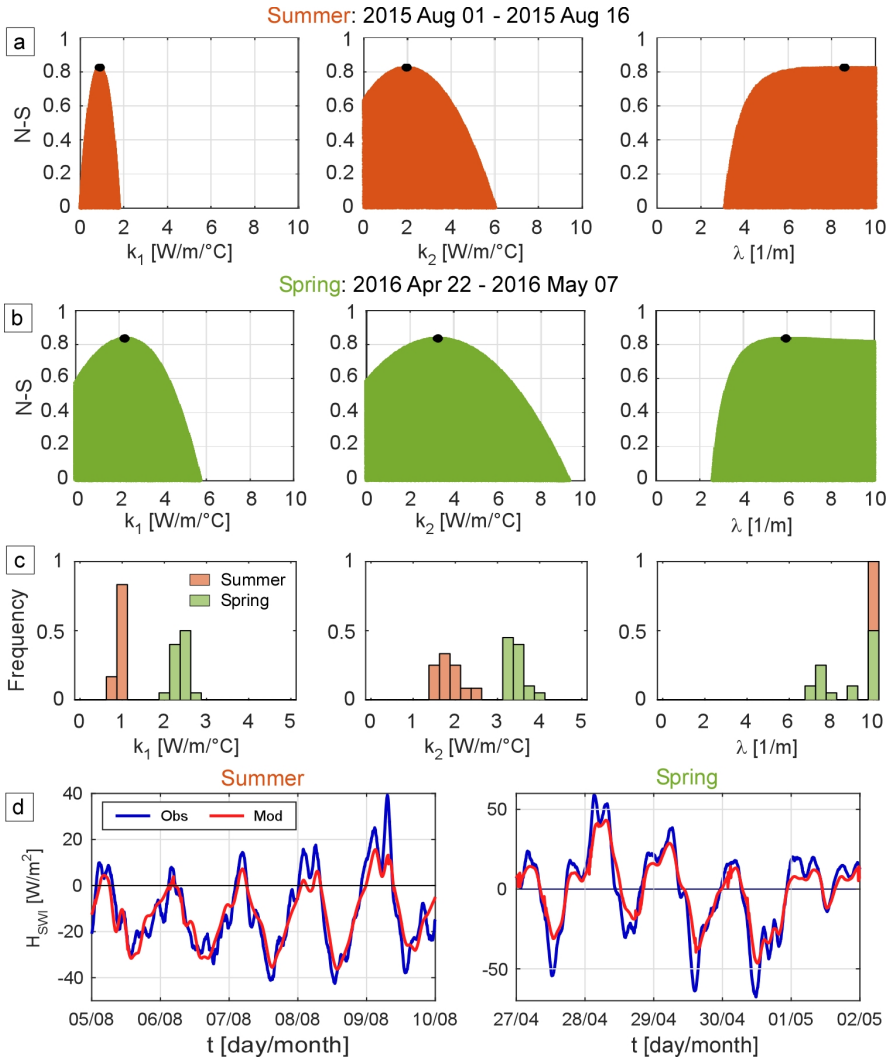

Figure 5.3: Calibration of the parameters in equation (4.14) for modeling H_{SWI}, performed over a 15-days-long moving time window. Panels (a) and (b) show the dotty plots of the Nash-Sutcliffe coefficient for the parameters obtained for, respectively, a summer and a spring time window; panel (c) shows the frequency analysis of the tested values of the parameters; panel (d) shows the comparison between the flux H_{SWI} computed on the basis of the data (i.e. using equation (4.4)) and modeled following (4.14). The flux is assumed positive when directed toward the water column.

5.3 Water-Sediment Interaction

In order to estimate the relevance of the thermal interaction between water and sediments at the SWI on the energy balance of the water column, we compared the contribution of the heat exchanged between water and sediments at the SWI with the contributions provided by the fluxes at the AWI (H_{sho}, H_{lon}, H_{sen}, H_{lat}).
As discussed in the previous section, the solar irradiance reaching the bottom at our study site is very small because of the high average turbidity of the water column. Therefore, the contribution of H_{res} to the net energy flux H_{SWI} is almost negligible and we can assume that the heat exchanged between water and sediments at the SWI H_{sed} can be represented by the net energy flux H_{SWI} computed on the basis of our sediment temperature data ($H_{sed} \approx H_{SWI}$).
We computed the energy fluxes at the AWI using the meteorological data provided by the Venice Municipality Monitoring Network (see section 3.3) as input for the formulas described in section 4.3.

To estimate the relevance of H_{SWI} for the energy balance of the water column, we analyzed the contribution of each vertical energy flux at the hourly and daily timescale. In particular, the contribution E_i $[J\ m^{-2}]$ provided by each flux H_i $[W\ m^{-2}]$ is given by:

$$E_i = \int_t^{t+\Delta t} H_i\ dt$$

where Δt is the considered timescale (hour or day). Each contribution E_i has been normalized using the total energy entering or exiting the water column (i.e. the sum of the different contributes in absolute value, $E_{tot} = \sum_i |E_i|$ $[J\ m^{-2}]$). The contribution of the flux to the energy balance is positive when it is directed toward the water column (i.e. it is warming the water column).

Figure 5.4 shows the comparison of the contributions provided by the different energy fluxes to the enegy balance at the daily timescale for a summer (Figure 5.4(a)) and a winter (Figure 5.4(b)) period of 10 days.
We observed that: both in summer and in winter the short wave radiation H_{sho} plays a major role; the heat loss due to evaporation H_{lat} is relevant in summer, while in winter the net long-wave energy flux H_{lon} plays the most significant role in cooling the water column; the sensible heat flux H_{sen}

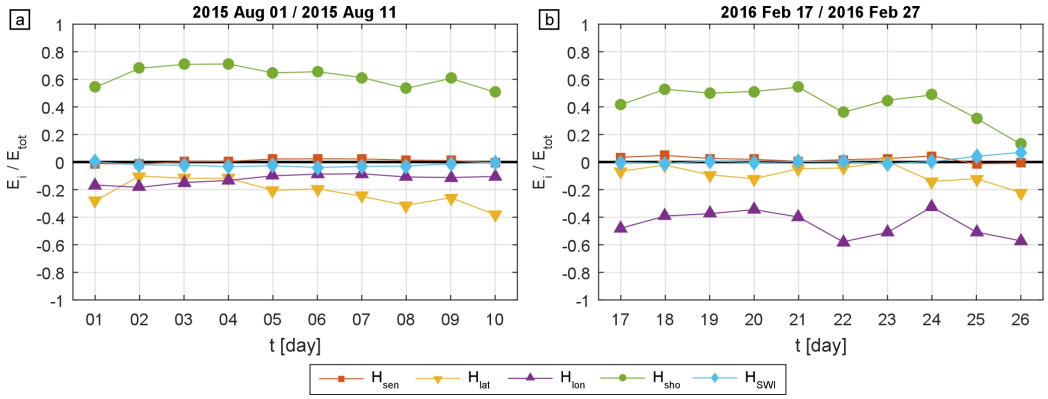

Figure 5.4: Comparison of the contribution provided by each vertical energy flux ($E_i = \int_t^{t+\Delta t} H_i \; dt \; [J \; m^{-2}]$) driving the water column dynamics to the water column energy balance at the daily timescale (i.e. $\Delta t = 1 \; day$), normalized with respect to $E_{tot} = \sum_i |E_i| \; [J \; m^{-2}]$. The figure shows the comparison in a summer (a) and in a winter (b) period 10-days-long. The contributions are positive when entering (i.e. warming) the water column.

and the heat exchanged at the SWI H_{SWI} provide always the lowest contributions, being usually negligible and never exceeding the 10% of the total energy.

Figure 5.5 shows the comparison of the contributions to the energy balance at the hourly timescale for a summer (Figure 5.5(a)) and a winter (Figure 5.5(b)) period of 2 days. In this case, we show also the time evolution of the different energy fluxes and of the net vertical energy flux H_N driving the water column dynamics (Figure 5.5(c) and 5.5(d)) for the same periods.
From the hourly timescale analysis we observed that: both in summer and winter, H_{sho} represents the most relevant contribution during daylight; in summer, H_{lon} and H_{lat} play an important role in cooling the water temperature, becoming the most important fluxes during night time; in winter, the cooling effect of H_{lon} is still important, while decreases the importance of H_{lat}; again, the contributions provided by H_{sen} and H_{SWI} are the lowest. In particular, the contribution related to H_{SWI} confirms to be limited and usually less than the 10% of the total energy entering/exiting the water column, never exceeding the 20%. Focusing on the time evolution of the energy fluxes (Figure 5.5(c) and 5.5(d)), we observed that, even when its contribu-

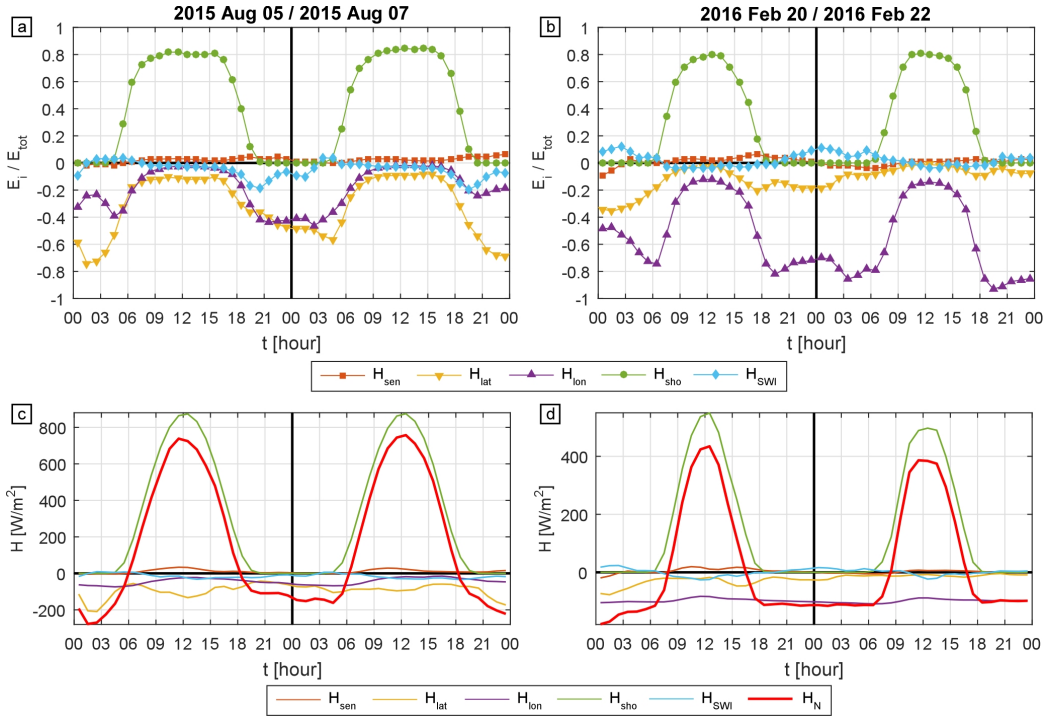

Figure 5.5: Comparison of the contribution provided by each vertical energy flux ($E_i = \int_t^{t+\Delta t} H_i dt$ $[J\ m^{-2}]$) driving the water column dynamics to the water column energy balance at the hourly timescale (i.e. $\Delta t = 1\ hour$), normalized with respect to$E_{tot} = \sum_i |E_i|$ $[J\ m^{-2}]$. Panels (a) and (b) show the contributions of the different energy fluxes for a period of 2 days in summer and in winter respectively. Panels (c) and (d) show, for the same periods, the time evolution of the different fluxes H_i $[W\ m^{-2}]$ driving the water column dynamics. The fluxes are positive when entering (i.e. warming) the water column.

tion to the total energy balance increases, the value of H_{SWI} is still very small. Especially in summer (Figure 5.5(c)), we observed that the contribution of H_{SWI} increases when the net vertical energy flux driving the water column temperature dynamics is smaller, and therefore the water column is not experiencing important temperature variations.

These observations seem to suggest that, for the considered study site, at least as a first approximation, we can neglect the heat flux at the SWI when

modeling the water temperature dynamics; we will further investigate this in section 6.1 based on the application of the "point" model.
Notwithstanding, H_{SWI} remains crucial for describing the sediment temperature dynamics and all the biological and ecological processes taking place in the lagoonal bed sediments.

Chapter 6

Water-Sediment Temperature Dynamics

In order to describe the temperature dynamics of the water-sediment continuum, we developed a "point" model by coupling equation (4.1), which describes the water column temperature dynamics, and the 1-D heat diffusion equation (4.2), applied to describe the dynamics of the vertical temperature profile within the bed sediments (see section 4.5). The 1-D (in the vertical direction) model we obtain following this approach allows us to reconstruct the time evolution of the water column temperature and of the sediments temperature as a function of the vertical energy transfer.
The SWI represents an "internal" boundary, where the interaction between water and sediments is described by the energy flux H_{SWI}, modeled as described in section 4.2. The values of the model parameters derive from the calibration procedure described in section 5.2, and they are valid for the study case considered in the present work.
The developed "point" model is based on a 1-D approach for studying the temperature dynamics of the water-sediment continuum, considering as driving forces only the vertical energy fluxes. Therefore, the applicability of such an approach is limited to the conditions in which the horizontal heat transport driven by advection is negligible.

6.1 Energy Balance: Advection Relevance

As discussed in section 4.5, a simple 1-D approach can be applied for investigating the temperature dynamics of the water-sediment continuum only when the horizontal heat transport driven by advection is negligible or at least plays a minor role compared to the vertical energy fluxes driving the temperature dynamics.

We analyzed the data we collected at our study site in order to ascertain if horizontal advection is indeed negligible and identify the periods when such an assumption is more reliable. We compared the net energy flux driving the water column temperature dynamics (i.e. the sum of both vertical and horizontal energy fluxes, H_N) with the sum of the vertical energy fluxes entering/exiting the water column (H_{NVert}).
In particular, H_N at our study site is computed using equation (4.1), describing the water column dynamics, solved considering the net energy flux as the unknown and using the measured water column temperature and water depth time series as input. Following such an approach, the "data based" net energy flux H_N necessarily accounts for both the horizontal and vertical heat fluxes.
The net vertical energy flux H_{NVert} consists in the sum of the energy fluxes at the AWI (H_{sho}, H_{lon}, H_{sen}, H_{lat}) and of the heat exchanged between water and sediments at the SWI (H_{sed}). We computed the energy fluxes at the AWI using the formulas from the literature described in section 4.1, providing as input the meteorological data obtained from the Venice Municipality Monitoring Network (see section 3.3). Being negligible the residual solar irradiance at the bottom (and therefore $H_{sed} \approx H_{SWI}$, see section 5.2), we assumed the flux H_{SWI} computed from equation (4.4) on the basis of the sediments temperature data as the best available estimate of the heat exchanged between water and sediments.

Figures 6.1, 6.2 and 6.3 show some examples of the comparison between the two fluxes (H_N and H_{NVert}) considering 5-days-long periods. In particular, in each figure, panel (a) shows the comparison of the two fluxes and, superimposed, the tidal signal, while panel (b) shows the comparison between the water temperature measured at the sea (T_S) and at our measuring station inside the lagoon (T_L).
We observe that the dynamics of the two fluxes is similar, but there are some

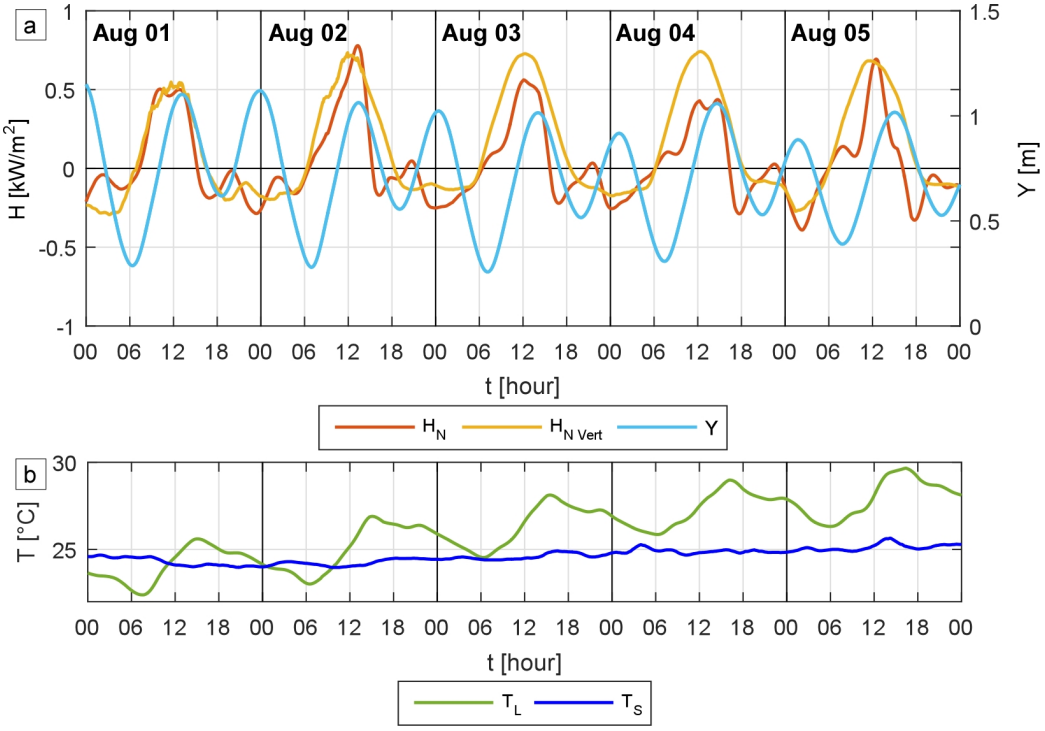

Figure 6.1: Relevance of the horizontal heat transport due to advection on the energy balance of the water column at our study site during for a 5-days-long period in Summer. Panel (a) shows the comparison between the net energy flux driving the water column temperature dynamics H_N $[kW\ m^{-2}]$, computed from equation (4.1) using the measured water temperature time series, and the sum of the vertical energy fluxes (H_{NVert} $[kW\ m^{-2}]$), and, superimposed, the water column depth (Y). Panel (b) shows the time evolution of the water temperature measured at the measuring station (T_L $[°C]$) (i.e. inside the Lagoon) and at the sea (T_S $[°C]$) (measured at the CNR platform, see figure 3.3).

marked differences during the flood phase of the tide.
Focusing on figure 6.1, the net energy flux H_N is lower than the sum of the vertical energy fluxes H_{NVert}, especially during the flood phases occurred in the morning of the 3^{rd} and 4^{th} of August, characterized by a quite big tidal excursion and a temperature of the sea quite lower than the lagoon temperature. The agreement between H_N and H_{NVert} is much better the 1^{st} of August, when we observe a lower difference between T_S and T_L. This

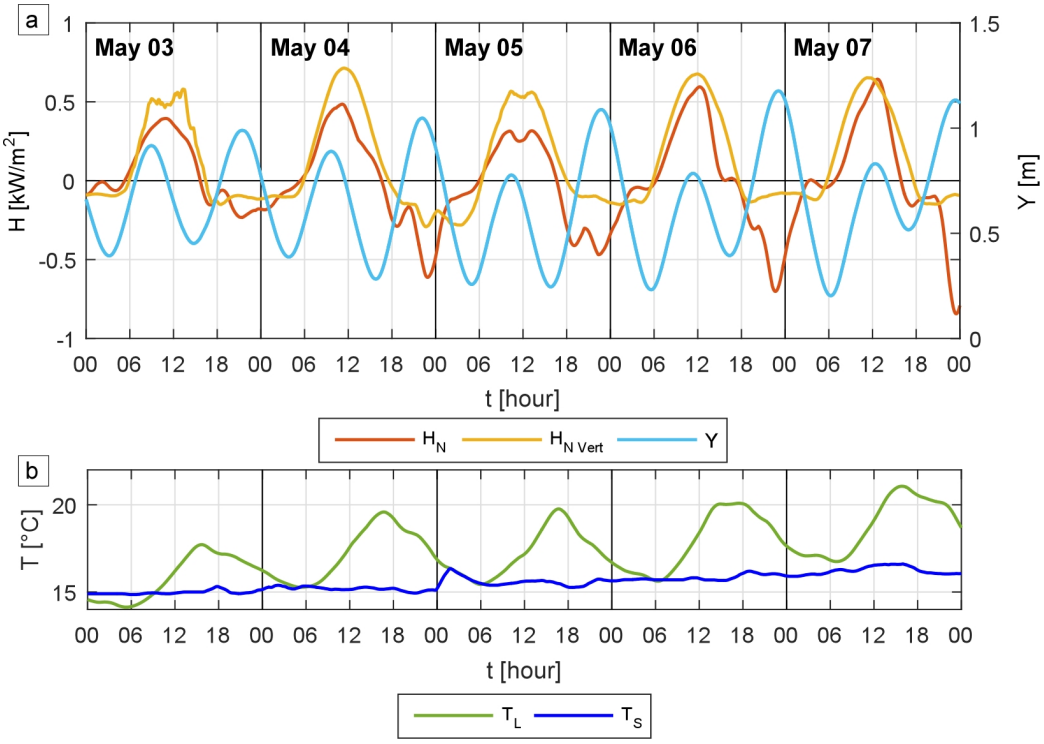

Figure 6.2: Relevance of the horizontal heat transport due to advection on the energy balance of the water column at our study site during for a 5-days-long period in Spring. Panel (a) shows the comparison between the net energy flux driving the water column temperature dynamics H_N $[kW\ m^{-2}]$, computed from equation (4.1) using the measured water temperature time series, and the sum of the vertical energy fluxes (H_{NVert} $[kW\ m^{-2}]$), and, superimposed, the water column depth (Y). Panel (b) shows the time evolution of the water temperature measured at the measuring station (T_L $[°C]$) (i.e. inside the Lagoon) and at the sea (T_S $[°C]$) (measured at the CNR platform, see figure 3.3).

observations suggest that the disagreement can be ascribed to the advective transport of colder water from the sea to the lagoon that is not accounted for in H_{NVert}.

Figure 6.2 shows the comparison for a 5-days-long period in May. Also in this case we observed a relevant difference between the two fluxes during the flood phase of the tide, especially between $6pm$ and $12am$ of the 5^{th}, the 6^{th}

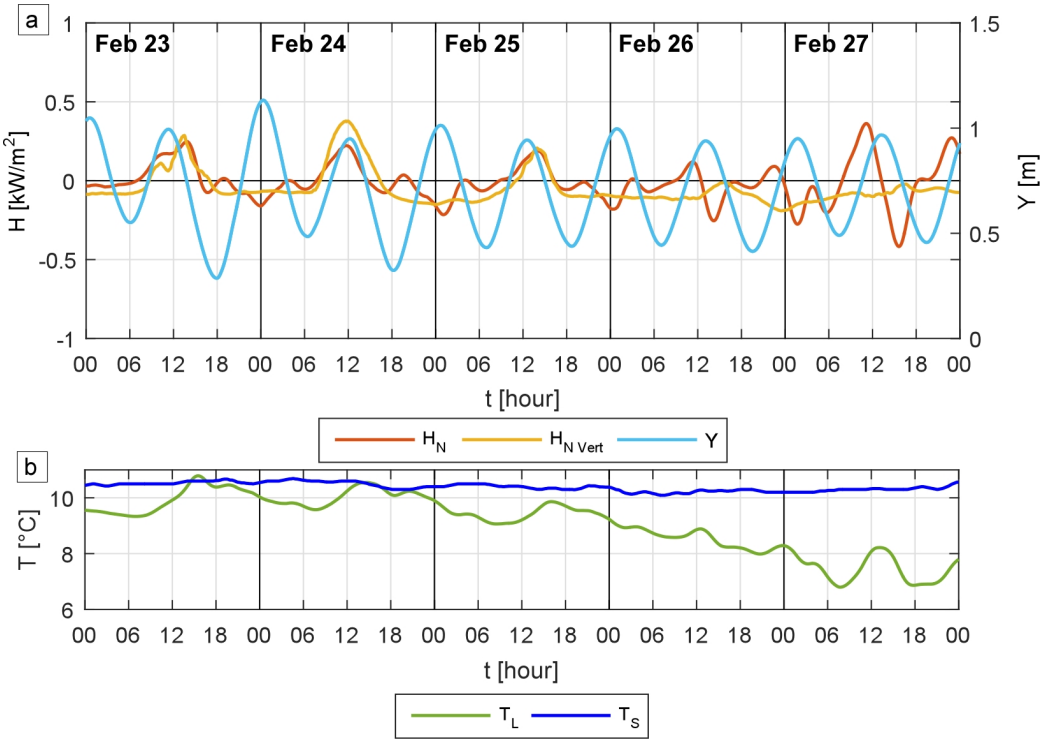

Figure 6.3: Relevance of the horizontal heat transport due to advection on the energy balance of the water column at our study site during for a 5-days-long period in Winter. Panel (a) shows the comparison between the net energy flux driving the water column temperature dynamics H_N $[kW\ m^{-2}]$, computed from equation (4.1) using the measured water temperature time series, and the sum of the vertical energy fluxes (H_{NVert} $[kW\ m^{-2}]$), and, superimposed, the water column depth (Y). Panel (b) shows the time evolution of the water temperature measured at the measuring station (T_L $[°C]$) (i.e. inside the Lagoon) and at the sea (T_S $[°C]$) (measured at the CNR platform, see figure 3.3).

and the 7^{th} of May, when the tidal oscillation is particularly high. Being the water temperature at the sea T_S lower than the water temperature inside the lagoon T_L, we observed a lower value of H_N because of a negative horizontal heat flux not accounted for in H_{NVert}. A much better agreement between the two fluxes characterizes the 3^{rd} of May, when both the difference between the water temperature at the sea and inside the lagoon and the tidal oscillation

are lower.
In winter the energy fluxes driving the water column temperature dynamics are much lower than in summer, and therefore their analysis becomes much more difficult. Nevertheless, the comparison between H_N and H_{NVert} during a 5-days-long period in February shown in Figure 6.3 provides further examples of the role of advection on the water column energy balance. In fact, in Figure 6.3 we observed that the disagreement between H_N and H_{NVert}, quite small during the first days, increases as the difference between the temperature at the sea and at the measuring station increases. In particular, during the flood phase of the 27th of February, positive flux not accounted for in H_{NVert}, and related to the warmer water transported from the sea toward the Lagoon by the tidal currents, can be identified concurrently with the flood phase of the tide. The negative flux characterizing the subsequent ebb phase (again not described by H_{NVert}) can be ascribed to the colder water transported from the internal portion of the lagoon.

The above observations suggest that, despite the choice of the study site quite close to the divide, horizontal advection is not always negligible, especially when the tidal excursion is large and the water temperature inside the lagoon is quite different from the water temperature at the sea. In order to investigate the water and sediment temperature dynamics using the "point" model described in the section 4.5 we therefore considered the periods in our dataset characterized by neap tide (i.e. small tidal oscillation) and/or small differences between water temperature at the sea and inside the lagoon, i.e. suitable conditions for considering the effect of the advective heat transport negligible.

6.2 Sediment Daily Temperature Profile

In order to apply the "point" model, we need to impose proper IC and BC as described in section 4.5. In particular, focusing on the spatial domain within the sediments, we need to provide the sediments vertical temperature profile at time $t = 0\ s$ as IC and the time evolution of the heat flux or of the sediment temperature as BC at the lower boundary of the spatial domain.
Recorded sediments temperature data, as the data collected during our field campaign, can provide both the necessary IC and BC. But these data are typically unavailable, and therefore their use as IC and BC clearly under-

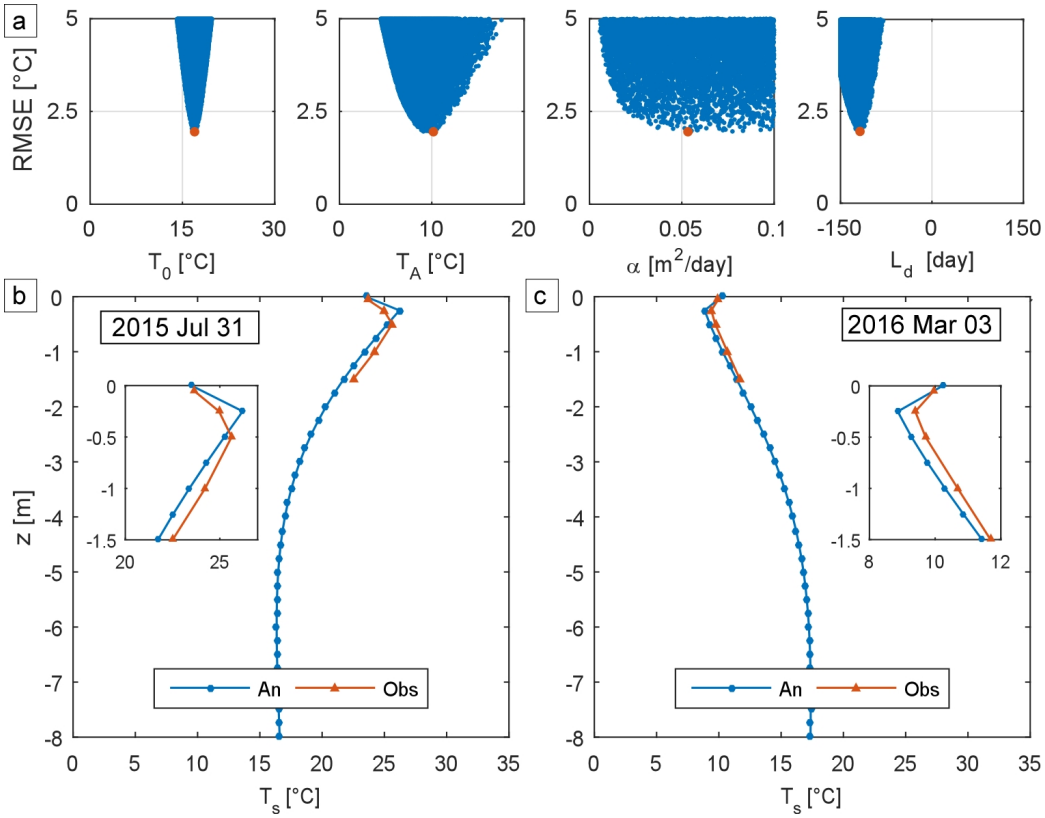

Figure 6.4: Calibration of the parameters in the analytical solution (4.5) of the heat diffusion equation (4.2). Panel (a) shows the dotty plots of the RMSE for the 4 parameters. Panels (b) and (c) show the observed mean daily temperature profile (orange line) and the mean daily temperature profile provided by solution (4.5) (blue line) using the calibrated parameters combination, in a summer and in a winter day respectively.

mines the applicability of the model as a predictive tool.

To overcome this limitation, when sediments temperature data are not available we can use as IC the mean daily temperature profile within the sediments provided by the analytical solution (4.5) of the heat diffusion equation (see section 4.5). The analytical solution (4.5) allows us to expand the spatial domain to a depth below the SWI where the sediments temperature is no longer affected by seasonal variations (i.e. the heat flux is $\approx 0\ Wm^{-2}$),

Parameter	Calibrated Value	Unit
T_0	≈ 17	$[^\circ C]$
T_A	≈ 10	$[^\circ C]$
α	$\approx 5.3\ 10^{-2}$ $\approx 6.1\ 10^{-7}$	$[m^2 d^{-1}]$ $[m^2 s^{-1}]$
L_d	≈ -118	$[d]$

Table 6.1: Values of the parameters for the analytical solution (4.5) of the heat diffusion equation (4.2), estimating the mean daily temperature profile within the sediment, provided by the calibration procedure described in section 6.2.

solving also the problem of imposing the BC at the lower boundary of the spatial domain. In fact, deep enough in the sediments, the temperature does not show seasonal variation, and we can therefore impose a constant sediments temperature as lower BC that coincides with the average seasonal temperature at the SWI.

Data collected within the sediments during our field campaign have been used to calibrate the values of the parameters of the analytical solution (4.5) for our study site. The parameters consists in: T_0 $[^\circ C]$, the average seasonal temperature at the SWI; T_A $[^\circ C]$, the seasonal temperature amplitude; α $[m^2 d^{-1}]$, the sediment thermal diffusivity; L_d $[d]$, a phase shift.
To calibrate the parameters, we applied the random sampling technique, minimizing the difference between the mean daily temperature derived from the data measured at the measuring station and computed using (4.5) at the depths within the sediments where the temperature sensors are located. In particular, we tested 10^6 random combination of parameters, considering the following variation ranges: $0 \leq T_0 \leq 30$ $[^\circ C]$, $0 \leq T_A \leq 20$ $[^\circ C]$, $0 \leq \alpha \leq 0.1$ $[m^2\ d^{-1}]$, $-150 \leq L_d \leq 150$ $[d]$. To identify the best combination of the parameters, we minimized the target function (5.1), with $z_i = 0.05, 0.25, 0.50, 1.00, 1.50$ $[m]$.
Figure 6.4 shows the results of the calibration, highlighting the best values for the parameters (Figure 6.4(a), each panel showing the dotty plots of the

RMSE for the parameters), and two examples of comparisons between the mean daily temperature profiles derived from the data and computed using the calibrated analytical solution (4.5) (Figure 6.4(b) and 6.4(c)). In table 6.1 we listed the calibrated values of the parameters. It is worthwhile noting that the sediment temperature profiles computed using the analytical solution (4.5) for a summer and a winter day show that the sediment temperature variation is negligible below a depth of $7 \div 8\ m$.
Toward the goal of providing a reliable IC for the vertical temperature profile within the bed sediment when temperature data are not available, temperature profile computed using the analytical formula does favorably compare with the observed one.

Even if not clearly identified, the value of α obtained from the calibration procedure ($\alpha \approx 5.3 \cdot 10^{-2}\ [m^2 d^{-1}] \approx 6.1 \cdot 10^{-7}\ [m^2 s^{-1}]$) well matches the value obtained from calibration in section 5.1 ($\alpha \approx 6.0 \cdot 10^{-7}\ [m^2 s^{-1}]$) supporting the reliability of the previous analysis.

6.3 "Point" Model Application

As discussed in paragraph 6.1, the "point" model we introduced in section 4.5 can be applied to reconstruct the sub-diurnal water and sediment temperature dynamics when the horizontal advective energy fluxes are negligible.
Although our study site was chosen in order to limit the importance of advection, we found that its contribution to the total energy balance is often not negligible (see section 6.1), thus limiting the applicability of the proposed 1-D approach. Notwithstanding, we identified in our dataset periods characterized by negligible horizontal energy transport (i.e. periods characterized by a small tidal excursion and/or similar water temperature at the sea and inside the lagoon - the corresponding period are highlighted in blue in Figure 3.4) that we used to verify the capability of our "point" model to reproduce the temperature dynamics of the water-sediment continuum and to further investigate the role of the energy flux at the SWI (H_{sed}) on the water temperature dynamics.

Using the values obtained from the calibration described in paragraph 5.2 for the model parameters k_1, k_2 and λ, we applied the model to estimate

the time evolution of the vertical temperature profile in the water-sediment continuum driven by meteorological forcings.
We performed the computations considering two alternative set-ups:

1. in the first set of model runs we imposed a measured vertical temperature profile as IC and the following BC: i) energy fluxes at the AWI computed from observed meteorological data; ii) measured water level; iii) sediment temperature measured at the deepest sensor deployed at our study site ($-1.5\ m$ with reference to the SWI);

2. in a second set of model runs we imposed as IC the sediment temperature profile given by equation (4.5) and, as lower BC, a constant bed sediment temperature of 17 $°C$ (the mean annual temperature at the SWI, as discussed in paragraph 6.2) at $z = -10\ m$ below the SWI. Following this approach, we do not need sediment temperature observations to perform our computations.

Figures 6.5, 6.6 and 6.7 show three examples of the results obtained by applying the model to reconstruct the temperature profile for three 5-days-long periods characterized by negligible advection. The light blue line corresponds to the observed water and sediments temperature, the red line represents to the result provided by the model using the first set-up for IC and BC while the yellow line shows the results provided using the second set-up.

Considering the runs corresponding to the first approach we observe, for all the considered periods, the quite good agreement between model results and observations both for the water temperature (the RMSE between observed and computed T_w is always lower than 1.0 [$°C$], while the value of the Nash-Sutcliffe coefficient ranges from 0.60 to 0.75) and the sediment temperature (results at $z > -0.5\ m$ are not shown as sediment temperature variation during a 5 days periods are almost negligible). This confirms the ability of the model to accurately describe the energy transfer processes and to correctly reproduce temperature dynamics in the water-sediment column at the sub-diurnal time scale.
Considering Figure 6.6 and 6.7 we observed that the IC provided by the analytical solution (4.5) represent a very good description of the observed sediments temperature profile at time $t = 0\ s$. The results provided by the model with the second set-up are basically the same observed using the first set-up, being the IC provided by (4.5) an optimal representation of the real

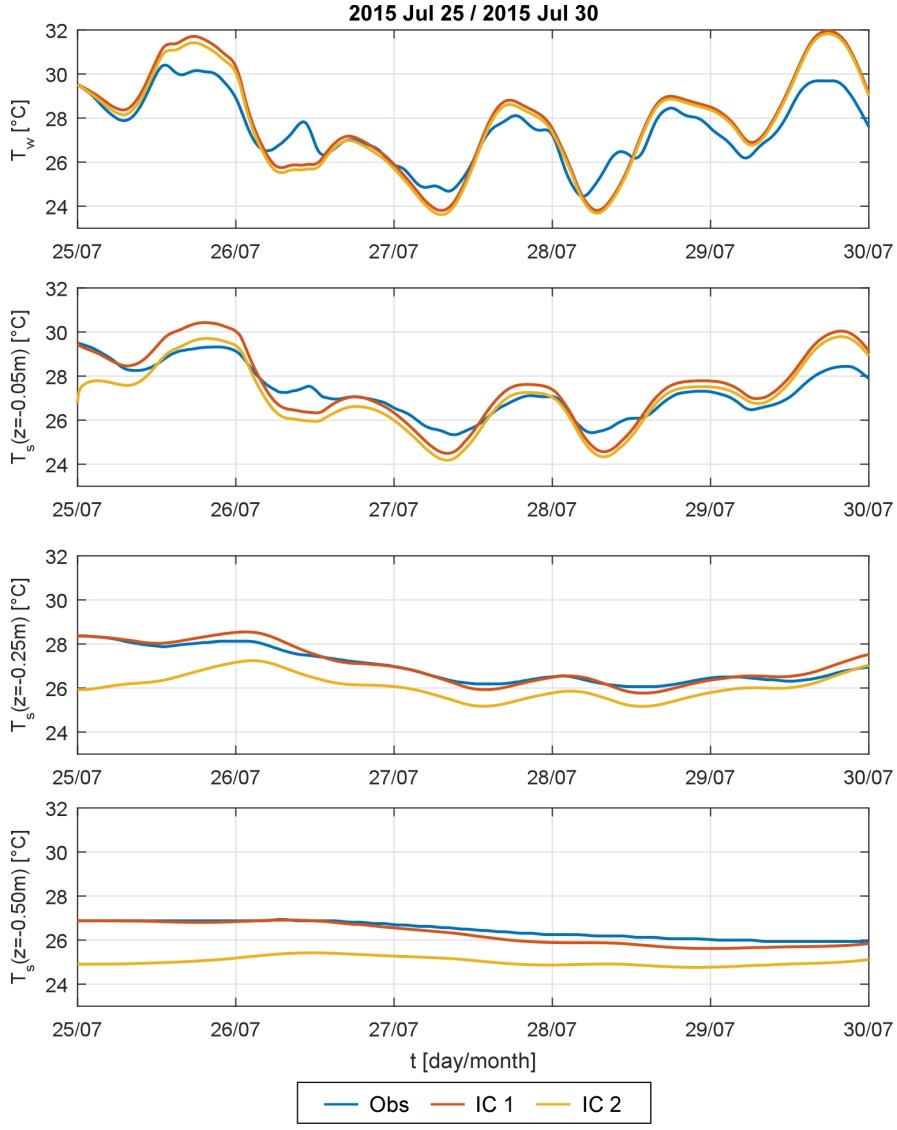

Figure 6.5: Results provided by the "point" model for a 5-days-long period in July. In particular, the Figure shows the comparison between the time evolution of the water and sediments temperature at different depths observed (Obs, blue line), computed using setup 1 (IC 1, orange line), and computed using setup 2 (IC 2, yellow line) for IC and BC within the sediments (refer to the text for the description of the two setups).

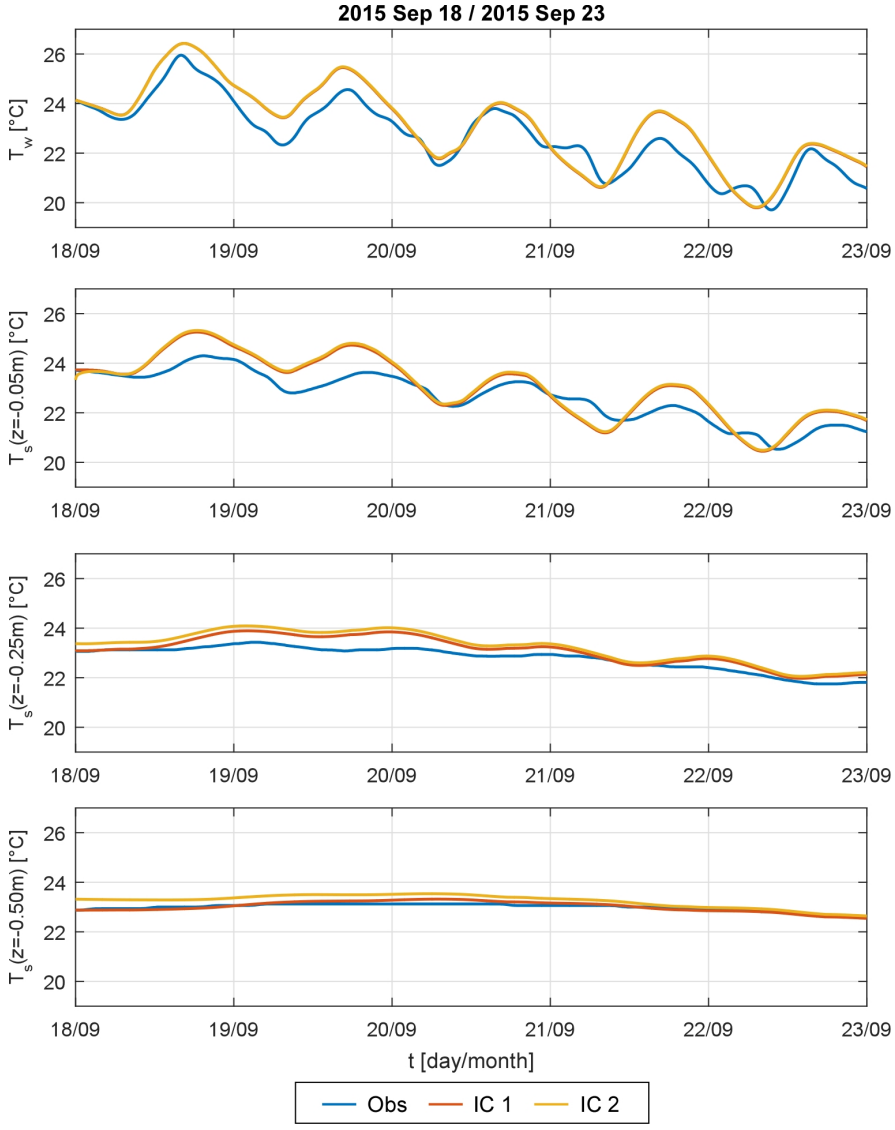

Figure 6.6: Results provided by the "point" model for a 5-days-long period in September. In particular, the Figure shows the comparison between the time evolution of the water and sediments temperature at different depths observed (Obs, blue line), computed using setup 1 (IC 1, orange line), and computed using setup 2 (IC 2, yellow line) for IC and BC within the sediments (refer to the text for the description of the two setups)

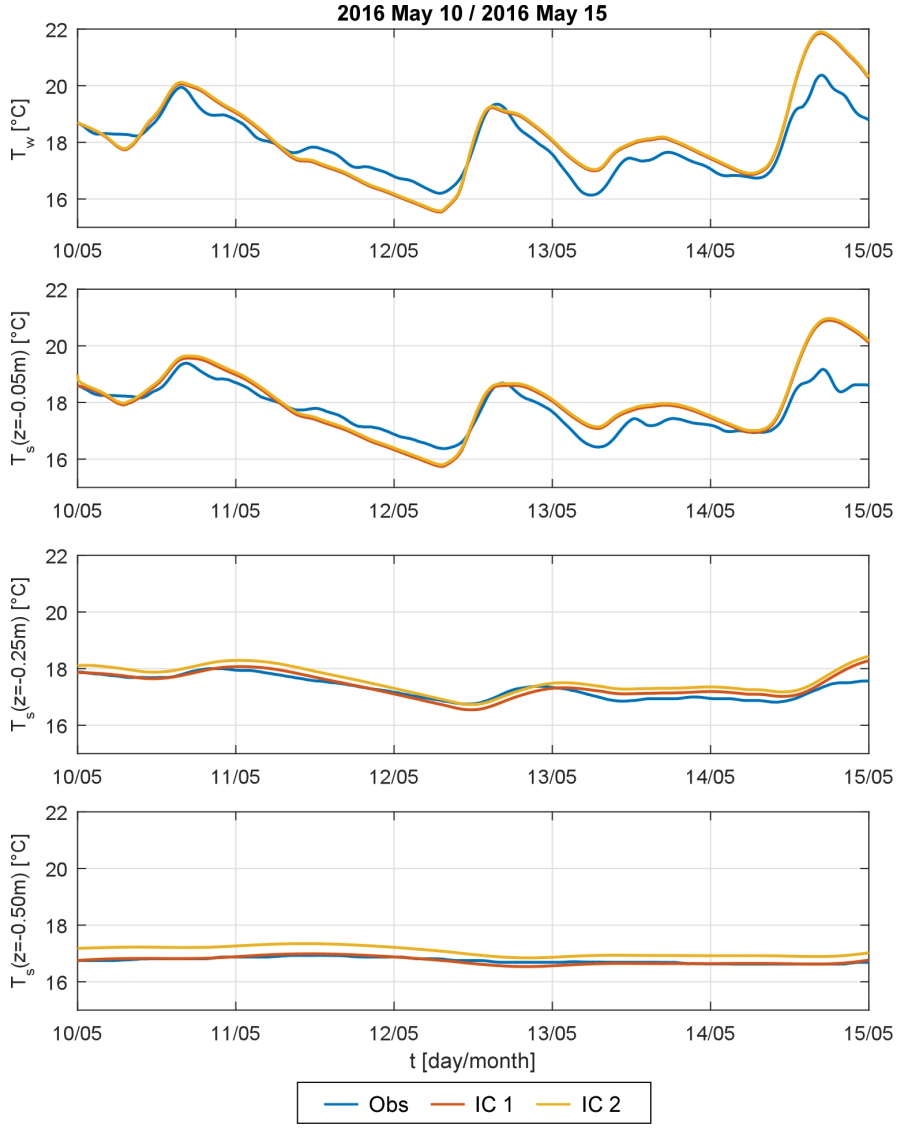

Figure 6.7: Results provided by the "point" model for a 5-days-long period in May. In particular, the Figure shows the comparison between the time evolution of the water and sediments temperature at different depths observed (Obs, blue line), computed using setup 1 (IC 1, orange line), and computed using setup 2 (IC 2, yellow line) for IC and BC within the sediments (refer to the text for the description of the two setups).

ones. Focusing on Figure 6.5, the differences between the IC imposed using the two different set-ups are more relevant. Interestingly, the difference between the sediment temperature observed and computed imposing as IC the temperature profile estimated using (4.5) decreases in time, suggesting that, even if the IC are not perfectly representative of the real temperature state of the sediments, the system (and the model) rapidly loses memory of the IC and converges to a good description of the temperature dynamics. In particular, the difference decreases quite fast in the upper part of the sediments, while more time is required in the deeper part to converge to the observed temperature because of the sediments thermal inertia. We can conclude that, in absence of temperature data within the sediments, the analytical solution of equation (4.2) provides a reasonably good approximation of the temperature profile within the sediment to be used as IC when sediment temperature data are not available, thus enhancing the possibility of using the model as a predictive tool.

Figures 6.8, 6.9 and 6.10 show the relevance of the thermal interaction between water and sediments for describing the water column temperature time evolution. In particular, panel (a) of each figure shows the comparison between H_{sed} computed either using the temperature data to solve equation (4.4) (being $H_{sed} \approx H_{SW1}$) (Obs, blue line) or provided by the model (i.e. using equation (4.15)) (Mod 1, red line), with positive values of the energy flux corresponding to fluxes directed toward the water column. Panel (b) compares the time evolution of the water temperature both measured (Obs, light blue line) and computed either considering (Mod 1, orange line) or neglecting (Mod 2, yellow line) H_{sed} in the energy balance. The 5-days-long periods considered for this analysis are the same observed in Figures 6.5, 6.6 and 6.7.
By comparing the modeled and the "data based" H_{sed} we observe a decent agreement between the time evolution of the fluxes, confirming the capability of the model to correctly reproduce the water-sediments interaction at the SWI. The satisfactory agreement between the water temperature measured and the results provided by the model has been already observed but, more interestingly, the negligible difference between the water temperature computed both considering and neglecting the heat flux at the SWI confirms that, at least at our study site, H_{sed} is small compared to other fluxes driving the water column dynamics and, therefore, can be neglected for modeling the water column temperature time evolution. In order to generalize this obser-

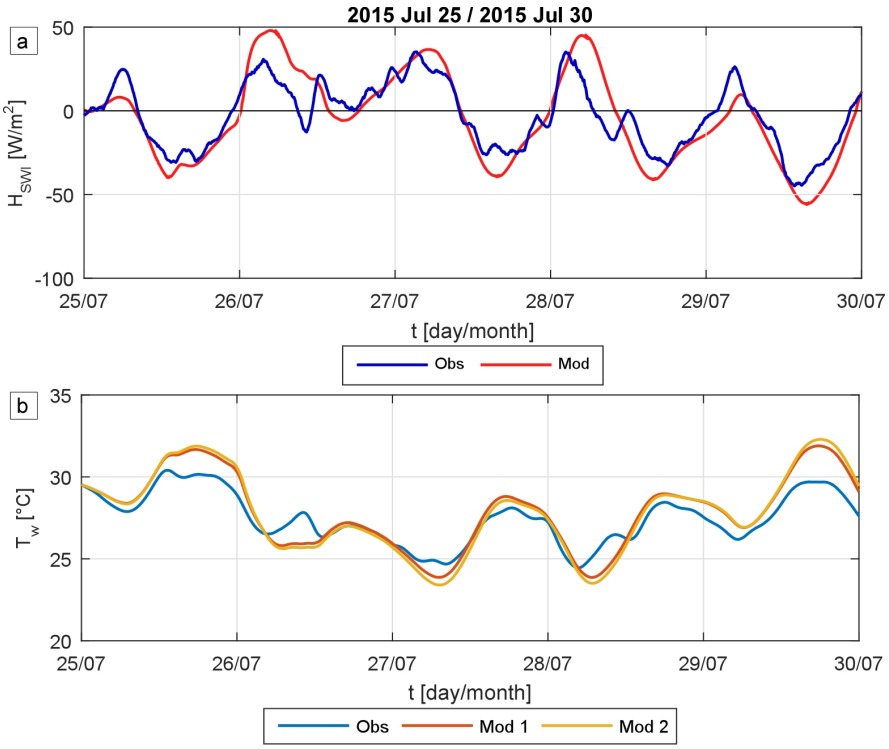

Figure 6.8: Relevance of the heat exchanged between water and sediment H_{sed} for modeling the water temperature dynamics, evaluated on a 5-days-long period in July. Panel (a) compares H_{sed} computed on the basis of the sediments temperature data (Obs, blue line), and provided by the model (Mod, red line). The flux is positive when directed toward the water column. Panel (b) compares the time evolution of the water temperature measured (Obs, blue line) and computed using the model both considering (Mod 1, orange line) and neglecting (Mod 2, yellow line) H_{sed}.

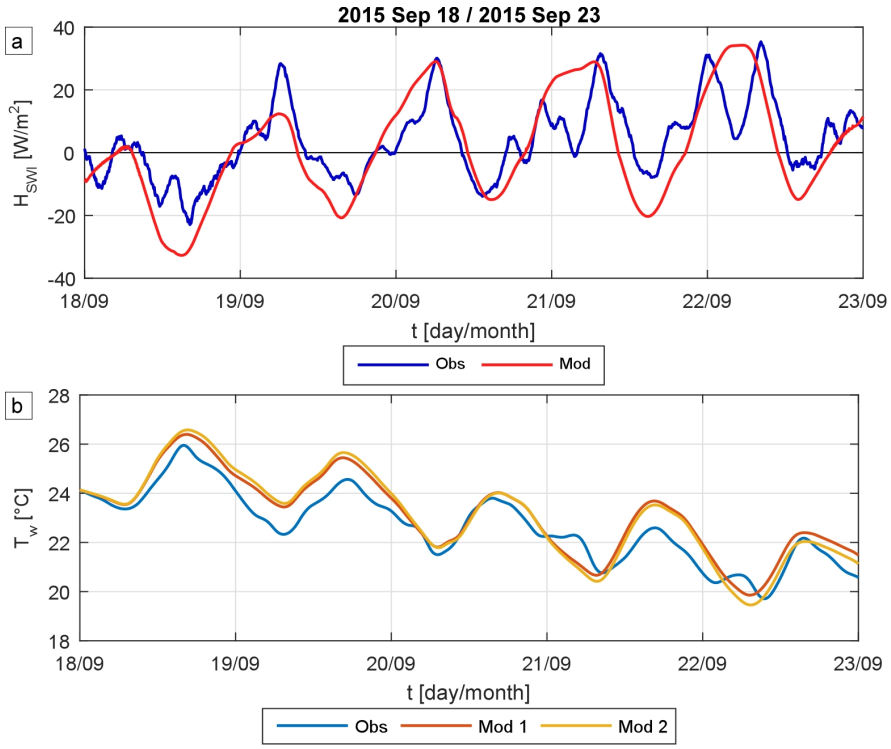

Figure 6.9: Relevance of the heat exchanged between water and sediment H_{sed} for modeling the water temperature dynamics, evaluated on a 5-days-long period in September. Panel (a) compares H_{sed} computed on the basis of the sediments temperature data (Obs, blue line), and provided by the model (Mod, red line). The flux is positive when directed toward the water column. Panel (b) compares the time evolution of the water temperature measured (Obs, blue line) and computed using the model both considering (Mod 1, orange line) and neglecting (Mod 2, yellow line) H_{sed}.

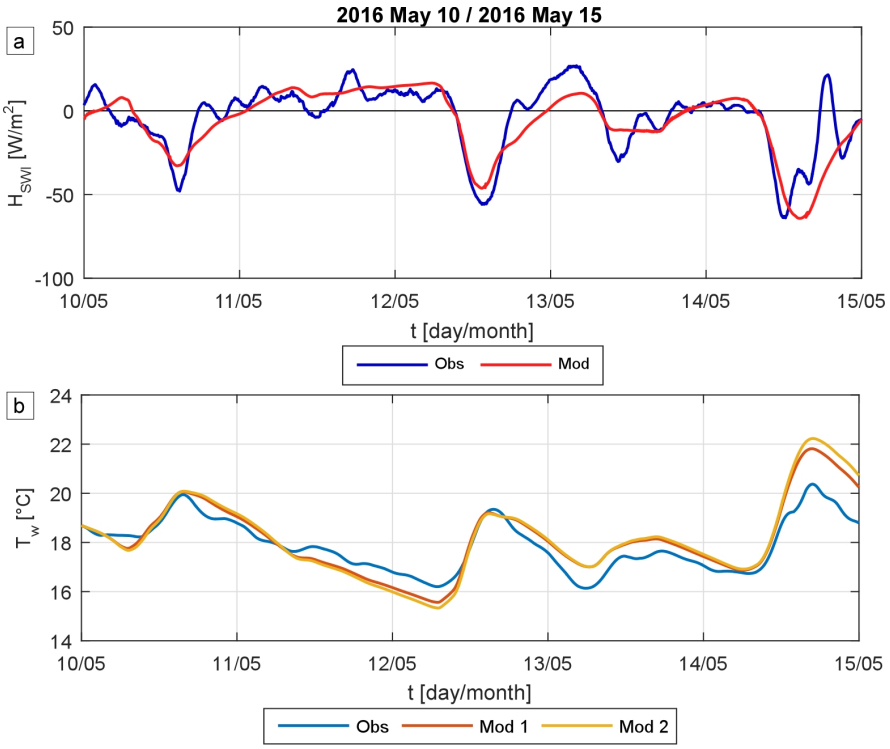

Figure 6.10: Relevance of the heat exchanged between water and sediment H_{sed} for modeling the water temperature dynamics, evaluated on a 5-days-long period in May. Panel (a) compares H_{sed} computed on the basis of the sediments temperature data (Obs, blue line), and provided by the model (Mod, red line). The flux is positive when directed toward the water column. Panel (b) compares the time evolution of the water temperature measured (Obs, blue line) and computed using the model both considering (Mod 1, orange line) and neglecting (Mod 2, yellow line) H_{sed}.

vation, the process deserves further investigation considering shallower, less turbid locations under the effect of different meteorological forcings.

Notwithstanding it is worthwhile noting that H_{sed} remains crucial for describing the sediment temperature dynamics and the dynamics of all the biochemical processes that take place within the first layer of sediment. For example the growth of benthic microalgae communities, frequently colonizing the tidal flat bottom and affecting the sediments stability, is sensitively affected by sediment temperature (Guarini et al. (1997)).

Chapter 7

Turbidity and Water-Sediment Temperature

The residual solar radiation reaching the sediment surface H_{res} $[W\ m^{-2}]$, found to be negligible at our study site, can be important considering different environmental conditions. In particular, lower turbidity conditions in the water column (i.e. clearer water, higher transparency) would reduce the irradiance absorption from the water column, increasing the radiative energy reaching the bottom for the same water depth.
In order to investigate the effect of the water turbidity on the water and sediments temperature dynamics, we performed a synthetic application of the "point" model we developed and discussed in the previous sections (see section 4.5 and chapter 6).
The results provided by the model application (i.e. water and sediment temperature and vertical heat fluxes driving the temperature dynamics) were then used to analyze the potential effect of the water column depth and turbidity on dynamics of the MPB, providing interesting hints on this process to be further investigated in future studies.

7.1 Synthetic Application

In order to investigate the effect of the water column turbidity on the temperature dynamics of the water-sediments continuum and on the MPB biomass growth, we applied the "point" model to a synthetic configuration, characterized by simplified conditions that allows us to isolate the process we are

interested in.

In particular, we performed different runs of the model investigating the effect of different combinations of water depth Y $[m]$ and water column turbidity, represented by the extinction coefficient λ $[m^{-1}]$. For each run of the model, we assumed Y and λ constant in time.
Apart from the water column turbidity and the water depth, we assumed to apply the model to a "study site" analogous to the tidal flat where we performed our field campaign (see chapter 3 for a description). Therefore we assumed a thermal diffusivity $\alpha = 6.0\ 10^{-7}$ $[m^2 s^{-1}]$ to characterize the bed sediments, in line with the sediments characterization performed considering the sediment temperature data we collected during the field campaign in the Venice lagoon (see section 5.1). We then used real meteorological data as BC for computing the energy fluxes at the AWI. In particular, for each combination of Y and λ we performed a 1-year-long run forcing the model with the meteorological data collected by the measuring stations of the Venice Municipality Monitoring Network (see section 3.3) during the year 2016.
As IC we imposed the mean daily temperature profile within the sediments computed using the analytical solution (4.5), using the parameters values provided by the calibration procedure described in section 6.2. The initial water temperature is assumed equal to the temperature at $z = 0\ m$ provided by equation (4.5). The analytical solution (4.5) allows us to extend our spatial domain to a depth of $z = -10\ m$ below the SWI, where the sediments temperature does not show seasonal variation, and therefore we can impose as BC a constant value of $T_s(t, z = 10\ m) = 17\ ^\circ C$. The constant temperature value at $z = -10\ m$ consists on the average annual temperature at the SWI, identified by the calibration of the parameters characterizing equation (4.5), described in section 6.2. In order to provide a proper start up to the system and loose memory of the initial state we actually run the simulations starting from the 1st of December 2015 and disregarded the first month of simulation when analyzing the results.
We modeled the energy flux at the SWI using equation 4.14. The analysis described in section 5.2 suggests a seasonal variation of the parameters k_1 and k_2, but the available data are not sufficient to identify a clear seasonal trend. Therefore, considering the synthetic approach of the present analysis we are performing and in order to apply the model for simulations 1-year-long, we assumed $k_1 = k_2 = 2.0$ $[W\ m^{-1} {}^\circ C^{-1}]$, i.e. the average value obtained in the calibration procedure performed using the data from our study site in the

Venice lagoon.

The results provided by the simulations performed using the "point" model allowed us to investigate the dynamics of the MPB photosynthetic rate P^B $[\mu g\ C\ (\mu g\ Chl\ a)^{-1} h^{-1}]$, described following the formulation presented by Guarini et al. (2000) and presented in section 4.6. The major factors driving the photosynthetic process of the MPB are the sediments surface temperature and the light availability at the bottom, both quantities provided as results from the application of the "point" model. In particular, we used the sediments temperature computed at the depth of 2.5 cm below the SWI as the sediment surface temperature T_{s0} and the residual solar irradiance actually reaching the bottom H_{res} (i.e. not absorbed by the overlying water column) to quantify the light availability. Therefore, we can study the variation of P^B as function of the different investigated conditions of turbidity and water depth.
The mathematical formulation describing the relationship between P^B, T_{s0} and H_{res} contains four site dependent physiological parameters: the light saturation constant, E_k $[W\ m^{-2}]$; the maximum photosynthetic rate under light saturation conditions, P_{max} $[\mu g\ C(\mu g\ Chl\ a)^{-1} h^{-1}]$, reached when the surface sediments temperature is equal to the optimal temperature T_{opt} $[^{\circ}C]$; the thermal threshold beyond which no photosynthesis occurs, T_{max} $[^{\circ}C]$. Furthermore, the formulation requires a dimensionless parameter β to be identify. Following Guarini et al. (2000), we can assume constant values for E_k, T_{opt}, T_{max} and β, while P_{max} experiences relevant seasonal variation. Since a general formulation providing the seasonal variation of P_{max} is not available in the literature, for our synthetic analysis we decided to use a con-

Parameter	**Value**	**Unit**
E_k	100	$[W\ m^{-2}]$
T_{opt}	25	$[^{\circ}C]$
T_{max}	38	$[^{\circ}C]$
β	2	
P_{max}	7	$\left[\frac{\mu g\ ^{\circ}C}{(\mu g\ Chl\ a)\ h}\right]$

Table 7.1: Values of the parameters used in the present study to describe the photosynthetic capacity of the MPB following the formulation proposed by Guarini et al. (2000).

stant value of P_{max}. Such an assumption, even if not physiologically correct, allows us to better highlight the effect of λ and Y on the P^B dynamics, being T_{s0} and H_{res} the only time varying variables.
In absence of specific data for the Venice lagoon, in the present study, we considered the values of the above parameters identified for the temperate Bay of Marennes-Oléron along the French Atlantic coast, used by Guarini et al. (2000). In particular, for P_{max} we used the mean among the values identified for different periods of the year in this Bay (see Blanchard et al. (1997)). Table 7.1 provides a list of the parameters and the associated values adopted in the present analysis.

7.2 Temperature and Fluxes Variation

In order to investigate the effect of the extinction coefficient λ (i.e. a proxy for the water turbidity), and of the water depth Y on the water and sediment temperature dynamics, we analyzed the variation of the daily maximum and minimum temperature during an entire year.

Figures 7.1 and 7.2 show the difference ΔT between the weekly maximum/minimum temperature computed using each considered value of λ and that computed considering the maximum investigated value for λ (i.e $\lambda = 8\ [m^{-1}]$), representative of a very turbid water column condition.
Figure 7.3 shows the daily contribution to the energy balance of the water column of each energy flux $E_i\ [J\ m^{-2}]$ driving the water column dynamics (i.e. daily integral of each energy flux), normalized using the total daily energy budget entering/exiting the water column $E_{tot} = \sum_i |E_i|\ [J\ m^{-2}]$.

The effect of λ on both the water column and the bed sediment temperature is more relevant during summer, when the solar irradiance reaches its maximum and water and sediment temperatures are higher.
We observed that the effect of λ decreases for higher water depths Y, being the solar radiation absorbed by the water column (H_{sho}) proportional to Y. Therefore, increasing Y, the water column absorbs most of the solar radiation also for low turbidity conditions (i.e. the contribution of H_{sho} to the energy balance of the water column does not change significantly with λ, as shown in figure 7.3), while the residual solar radiation at the bottom H_{res} decreases, causing limited variation of the sediments temperature time

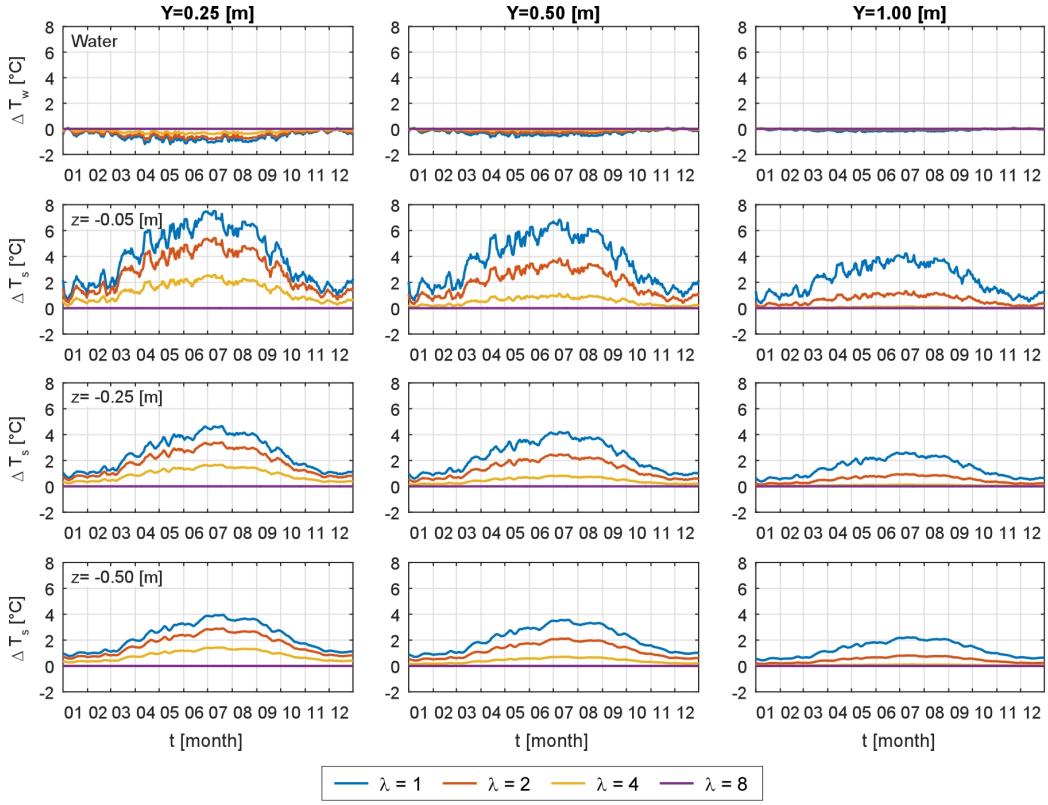

Figure 7.1: Time evolution of the difference ΔT $[°C]$ between the weekly maximum temperature computed using different values of λ $[m^{-1}]$ and that obtained considering extremely turbid conditions (i.e. $\lambda = 8.0\ m^{-1}$). ΔT is computed both for the water column (first row) and the sediments (other rows). Each column shows the time evolution of ΔT obtained for a different water depth Y overlying the sediment bottom. The results refer to the entire year 2016.

evolution. In particular, considering $Y \leq 0.50\ m$, ΔT is not negligible for each value of λ we compared to $\lambda = 8.0\ m^{-1}$, while for $Y > 0.50\ m$ ΔT is relevant only when comparing very clear water condition ($\lambda \leq 1.0\ m^{-1}$) with very turbid water condition ($\lambda = 8\ m^{-1}$).

Interestingly, the dynamics of the water temperature T_w appears to be poorly affected by the value of λ, independently on the water depth. Reducing the water column turbidity (i.e. decreasing λ), and therefore the solar

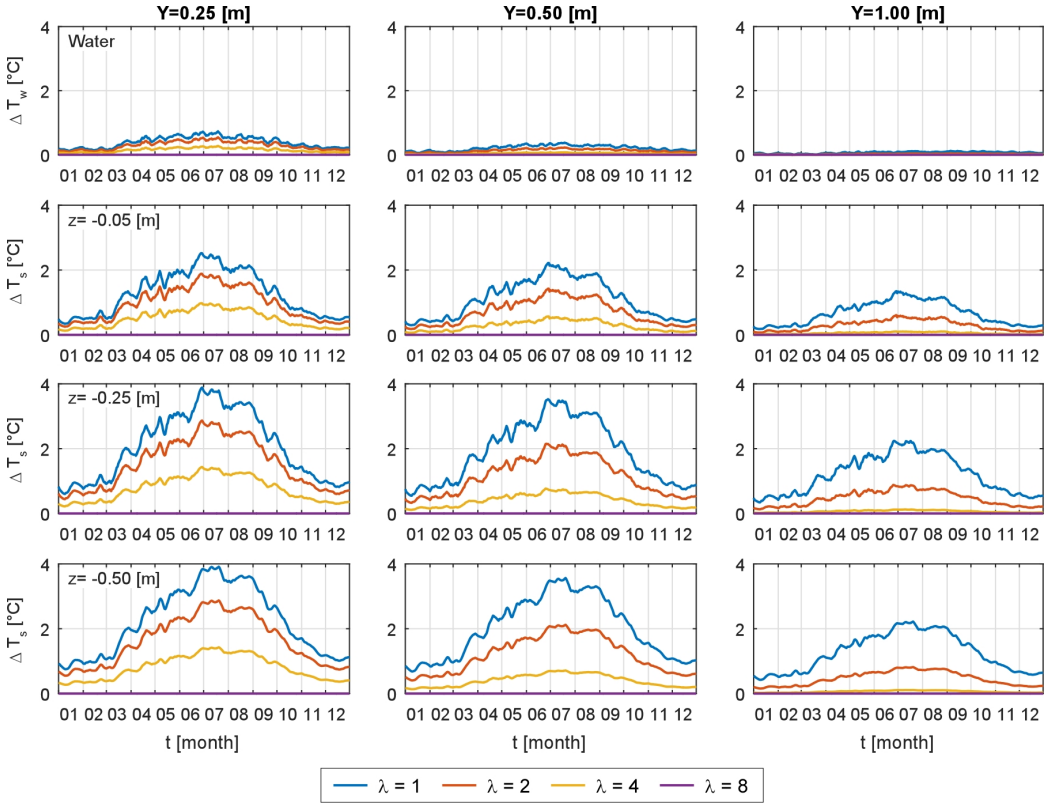

Figure 7.2: Time evolution of the difference ΔT $[^{\circ}C]$ between the weekly minimum temperature computed using different values of λ $[m^{-1}]$ and that obtained considering extremely turbid conditions (i.e. $\lambda = 8.0\ m^{-1}$). ΔT is computed both for the water column (first row) and the sediments (other rows). Each column shows the time evolution of ΔT obtained for a different water depth Y overlying the sediment bottom. The results refer to the entire year 2016.

radiation absorbed by the water column, we observed a reduction of the maximum water temperature that is always lower than $1.5^{\circ}C$ throughout year, and almost negligible for $Y \geq 0.50\ m$. The variation of the minimum water temperature is positive (i.e. the minimum temperature increases decreasing λ), but it is even less significant than the variation observed for the temperature maximum (i.e. less than $0.75^{\circ}C$).

This behavior can be explained observing Figure 7.4, showing: the daily contributions to the water column energy balance, normalized with E_{tot}, of

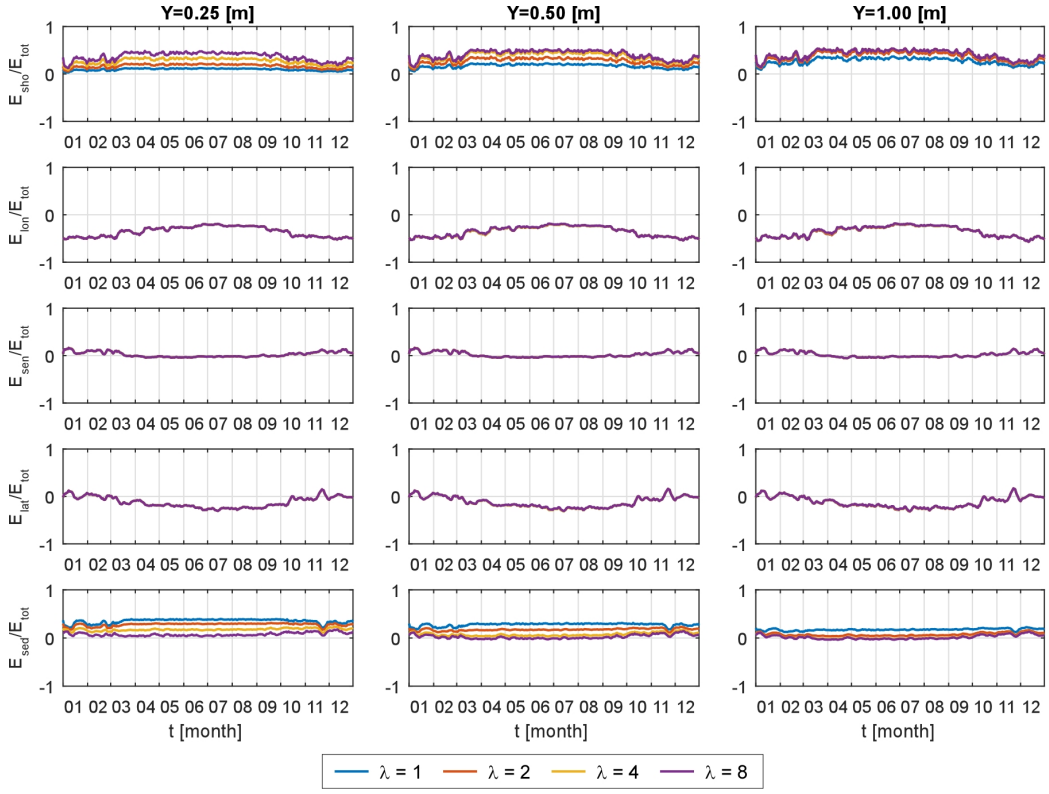

Figure 7.3: Analysis at the seasonal timescale of the daily contribution E_i $[J\ m^{-2}]$ of each energy flux driving the water column temperature dynamics (i.e. daily integral of the energy flux) to the energy balance of the water column as function of λ and Y. Contributions E_i are normalized with $E_{tot} = \sum_i |E_i|$ $[J\ m^{-2}]$. The results shown refer to the entire year 2016.

the solar radiation absorbed by the water column (E_{sho}) and of the heat exchanged at the SWI between water and sediments (E_{sed}); the daily integral of the residual solar radiation H_{res} reaching the bottom (E_{res}), also normalized with E_{tot} in order to make it comparable with E_{sho} and E_{sed}.
Decreasing λ (i.e. decreasing the water column turbidity), the contribution E_{sho} decreases because the solar radiation absorption capacity of the water column is lower, while E_{sed} increases. In fact, the solar radiation not absorbed by the water column reaches the sediment bottom and consequently increases the sediment temperature and the temperature gradient at the SWI. Therefore, the heat exchanged between water and sediments at the SWI increases,

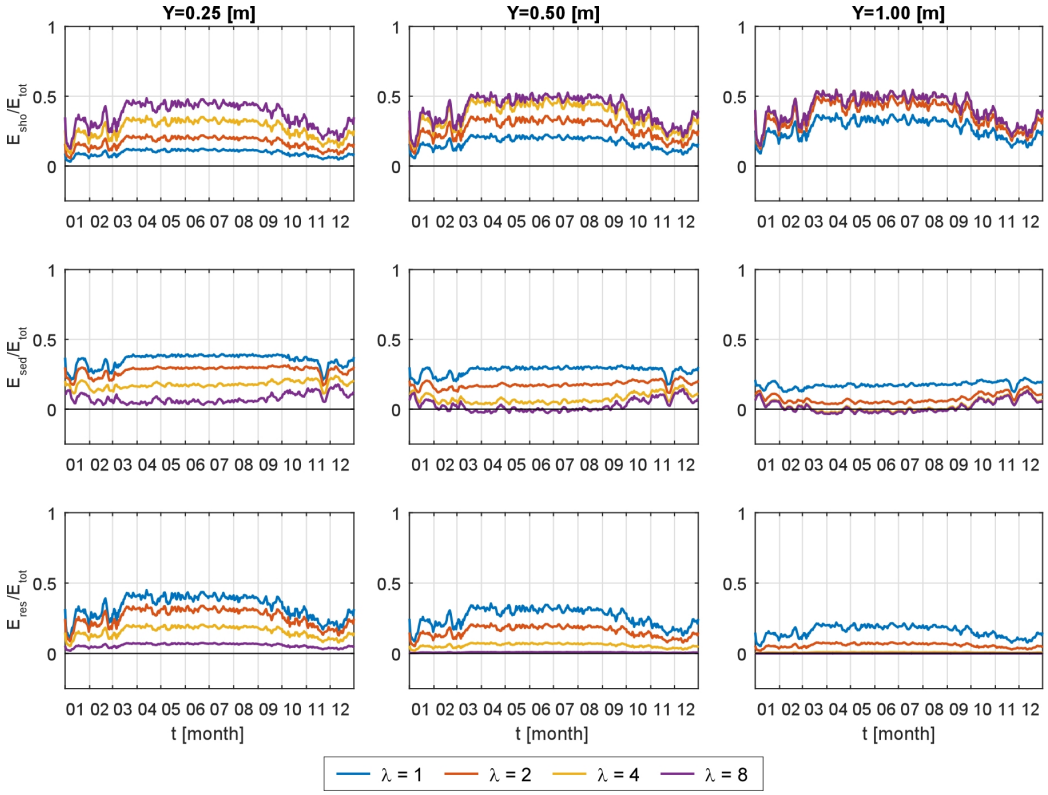

Figure 7.4: Seasonal variation of the daily integral of the solar radiation absorbed by the water column E_{sho} $[J\ m^{-2}]$, of the heat flux exchanged between water and sediments at the SWI E_{sed} $[J\ m^{-2}]$ and of the residual solar radiation reaching the sediment bottom E_{res} $[J\ m^{-2}]$ as function of λ and Y, normalized with the total energy entering/exiting the water column E_{tot} $[J\ m^{-2}]$. The results shown to the entire year 2016.

such as the contribution E_{sed}. Comparing E_{sed} and E_{res}, both normalized with respect to E_{tot}, we observed that their values are similar, especially in summer when the solar radiation is higher. This observation suggests that an important portion of the energy provided to the sediment by the residual solar radiation actually reaching the SWI when turbidity is low is given back to the water column by the sediment as conductive heat flux.
Because of the negligible variation of T_w, the fluxes at the AWI not directly linked to the solar irradiance do not vary significantly, as shown in Figure 7.3.

On the contrary, the bed sediment temperature is strongly affected by the extinction coefficient λ and by the water depth Y. The variation of the solar radiation reaching the bottom indeed modifies the sediment temperature, at the surface as well as deeper underground.
Considering the maximum temperature, the effect of λ is more relevant at the surface. The difference between the maximum temperature computed assuming very clear water conditions ($\lambda = 0.5\ m^{-1}$) and very turbid water ($\lambda = 8.0\ m^{-1}$) is $\geq 6°C$ for all the considered water depths Y at the sediment surface, and is still about $4°C$ until $z = -1.0\ m$.
Considering the minimum temperature, instead, the difference between the temperature computed in very clear water and very turbid water conditions are more relevant when increasing the water depth.

7.3 MPB Photosynthetic Capacity

Using the time evolution of the bed sediment temperature at the SWI T_{s0} [$°C$] and of the solar irradiance reaching the bottom H_{res} [$W\ m^{-2}$] as a function of λ and Y provided by the model runs, we analyzed how the different conditions we investigated affect the photosynthetic rate P^B [$\mu g\ C(\mu g\ Chl\ a)^{-1}h^{-1}$] of the MPB. Following the formulation described in section 4.6, P^B is function of the light availability at the sediment bottom, assumed equal to H_{res}, and of the maximal photosynthetic capacity under light saturation P^B_{max} [$\mu g\ C(\mu g\ Chl\ a)^{-1}h^{-1}$], which is function of T_{s0}.

Figures 7.5, 7.6 and 7.7 show the dynamics of P^B_{max}, P^B and of T_{s0} for 2-days-long periods in spring, winter and summer respectively.
The MPB photosynthetic process results to be favored by the combination of light availability and sediments temperature during the spring period (Figure 7.5). The surface sediments temperature, especially during daytime, is similar to the optimal temperature T_{opt} (red line in Figures 7.6(c), 7.5(c) and 7.7(c)) at which P^B_{max} reaches its maximum, independently on the water column turbidity conditions. Being the temperature conditions favorable, the light availability represents the limiting factor for the photosynthetic process. Therefore, we observed that clear water conditions (i.e. lower values of λ) correspond to higher values of P^B for water column depths we considered in our analysis. Figure 7.5 further shows that for very shallow water conditions

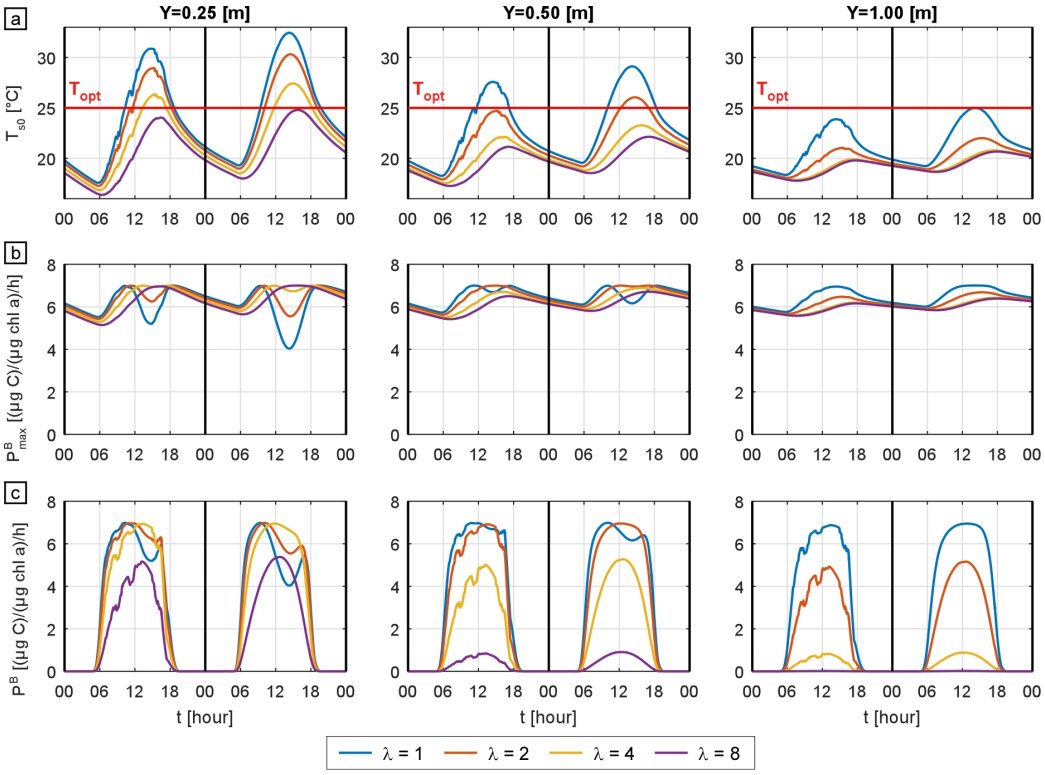

Figure 7.5: Dynamics, as function of the water column turbidity (described by λ $[m^{-1}]$) and of the water depth Y $[m]$, of: (a) the surface sediments temperature T_{s0} $[°C]$; (b) the MPB photosynthetic rate under light saturation condition P^B_{max} $[\mu g\ C(\mu g\ Chl\ a)^{-1}h^{-1}]$; (c) the MPB photosynthetic rate P^B $[\mu g\ C(\mu g\ Chl\ a)^{-1}h^{-1}]$. The red line in panel (a) identifies the optimal temperature T_{opt} for P^B_{max}. The results refer to $15-16$ April 2016.

(e.g. $Y \approx 0.25\ m$) the light availability is enough to promote the MPB photosynthesis even in very turbid water condition, while a clear water column conditions is necessary for increasing the photosynthetic rate for higher values of Y, in particular for $Y > 0.50\ m$. We observed that light availability at the bottom becomes insufficient for MPB photosynthesis when $\lambda \geq 8\ m^{-1}$ if $Y = 0.5\ m$ and when $\lambda \geq 4\ m^{-1}$ if $Y = 1.0\ m$.
In winter (Figure 7.6), both light availability and sediments temperature T_{s0} conditions are such that they limit the potential photosynthetic activity. T_{s0} is always lower than T_{opt}, and the solar radiation is significantly lower compared to the other seasons. Therefore, we observed that the MPB

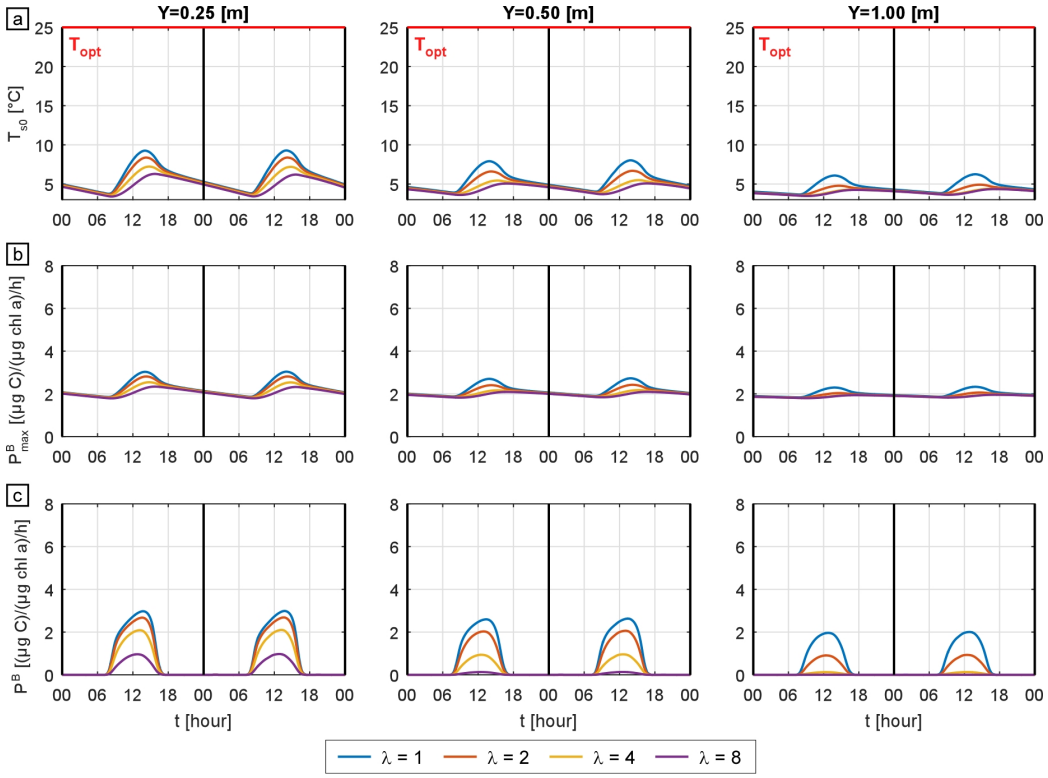

Figure 7.6: Dynamics, as function of the water column turbidity (described by λ $[m^{-1}]$) and of the water depth Y $[m]$, of: (a) the surface sediments temperature T_{s0} $[°C]$; (b) the MPB photosynthetic rate under light saturation condition P^B_{max} $[\mu g\ C(\mu g\ Chl\ a)^{-1}h^{-1}]$; (c) the MPB photosynthetic rate P^B $[\mu g\ C(\mu g\ Chl\ a)^{-1}h^{-1}]$. The red line in panel (a) identifies the optimal temperature T_{opt} for P^B_{max}. The results refer to $16-17$ January 2016.

photosynthetic capacity is favored by clearer water conditions, for which, during daytime, we observe an increase of both the light availability and the sediments temperature, reducing the difference between T_{s0} and T_{opt} and consequently increasing P^B_{max}.
Conversely, during the summer season (Figure 7.7), the observed bed sediment temperature is much higher than T_{opt}. Therefore, even if clear water conditions (low values of λ) provide more light for photosynthesis, the irradiance reaching the bottom increases the bed sediment temperature, raising the difference between T_{s0} and T_{opt} and causing a decrease of P^B_{max} and, consequently, of P^B. For very clear water conditions and shallow water depths,

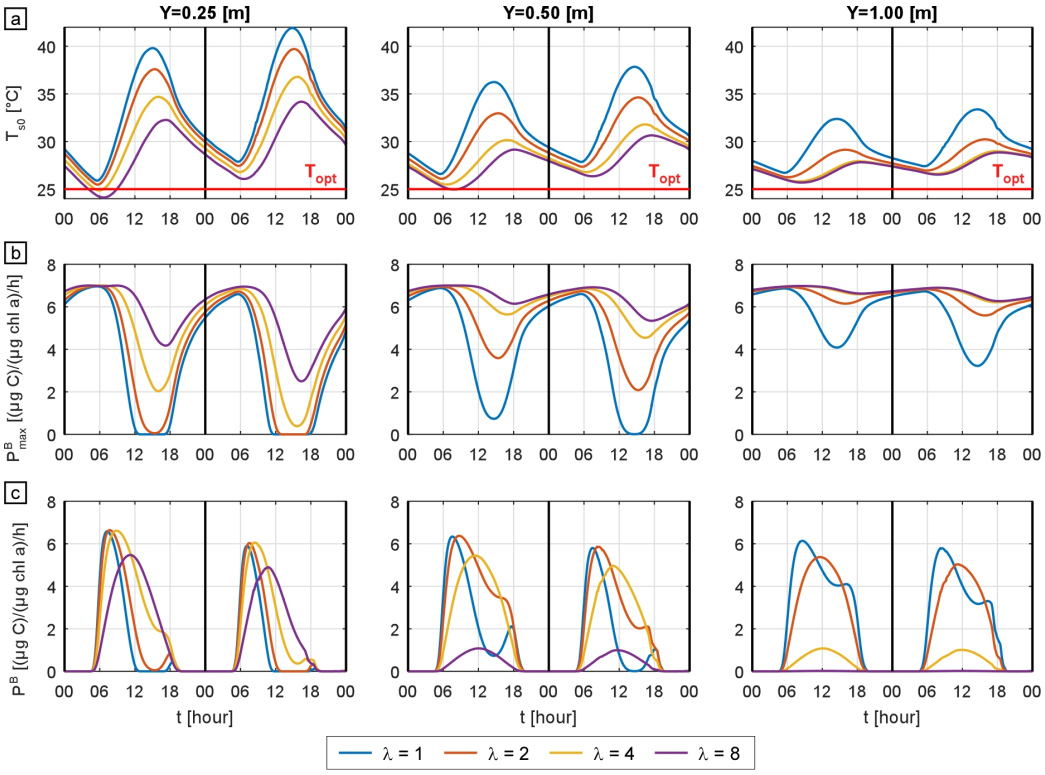

Figure 7.7: Dynamics, as function of the water column turbidity (described by λ $[m^{-1}]$) and of the water depth Y $[m]$, of: (a) the surface sediments temperature T_{s0} $[°C]$; (b) the MPB photosynthetic rate under light saturation condition P^B_{max} $[\mu g\ C(\mu g\ Chl\ a)^{-1}h^{-1}]$; (c) the MPB photosynthetic rate P^B $[\mu g\ C(\mu g\ Chl\ a)^{-1}h^{-1}]$. The red line in panel (a) identifies the optimal temperature T_{opt} for P^B_{max}. The results refer to $8-9$ August 2016.

we observed an increase of T_{s0} driven by the residual solar irradiance reaching the bottom over the maximum temperature threshold T_{max}, which makes P^B_{max} and P^B to go to zero. Therefore, during summertime, the photosynthetic activity can be better promoted by more turbid water conditions, especially dealing with very shallow water depths (i.e. $Y \leq 0.5\ m$). With higher water depths (e.g $Y = 1.0\ m$), we observe that, such as in winter and spring, clearer water conditions represent the more suitable condition for the MPB photosynthesis because the major limiting factor consists again with the light availability at the bottom. In particular, P^B decreases dramatically for $\lambda > 2.0\ m^{-1}$ if compared with the dynamics observed before using the

same value of λ but with shallower overlying water column.

In order to observe the seasonal dynamics of the MPB photosynthetic capacity P^B, Figure 7.8 shows the daily integral of P^B ($P^B_{day} = \int_{0h}^{24h} P^B(t)dt$ $[\mu g\ C(\mu g\ Chl\ a)^{-1}]$).
Figure 7.8 confirms the observations we made analyzing the dynamics of P^B at the daily timescale. On average, spring and autumn are the seasons characterized by the combination of light availability and sediments temperature that better promotes the MPB photosynthetic process. This observation is particularly true when dealing with shallow water depths and relatively clear water conditions (i.e. $\lambda \leq 4\ m^{-1}$ for $Y = 0.25\ m$, $\lambda \leq 2\ m^{-1}$ for $Y = 0.5\ m$). In these cases, the important amount of solar irradiance reaching the bottom in summer increases the temperature over T_{opt}, acting as a limiting factor for the photosynthetic process. For higher water depths and/or more turbid water conditions, the amount of residual solar radiation at the bottom is lower and does not increase significantly T_{s0}. Therefore, the limiting factor for the MPB growth becomes the light availability, that increases for clearer water column conditions. In general, considering shallow water conditions ($Y \leq 0.50\ m$), the same values of turbidity can be more or less favorable for the photosynthetic rate. During most of the year, from mid September to mid May, P^B increases with the increasing of the water column clarity (lower values of λ), while from late spring to late summer we observe an inversion, with higher values of P^B related to more turbid water condition ($2 \leq \lambda \leq 4$). Nevertheless, excluding a brief period during summer with very shallow water ($Y = 0.25\ m$), very turbid water conditions ($\lambda \approx 8\ m^{-1}$) are the least favorable for P^B and therefore for the growth of the MPB biomass.

The above observations suggest that, considering the average annual budget, in shallow water environments clear water column conditions better promote the photosynthetic process and therefore the MPB biomass growth compared with turbid conditions, even considering the observed reduction in case of very shallow water depths during summer. As we already discussed in section 1.1 and 4.6, the MPB proliferation provides a bio-stabilization effect on the surface sediments (Paterson (1989), Miller et al. (1996)). In fact, the MPB produces extracellular polymeric substances (EPS) creating a biofilm on the sediment surface that reduces the sediment resuspension and the bed erosion (Parsons et al. (2016)). Therefore, since an higher amount of MPB biomass on the sediments surface reduces the sediment resuspension,

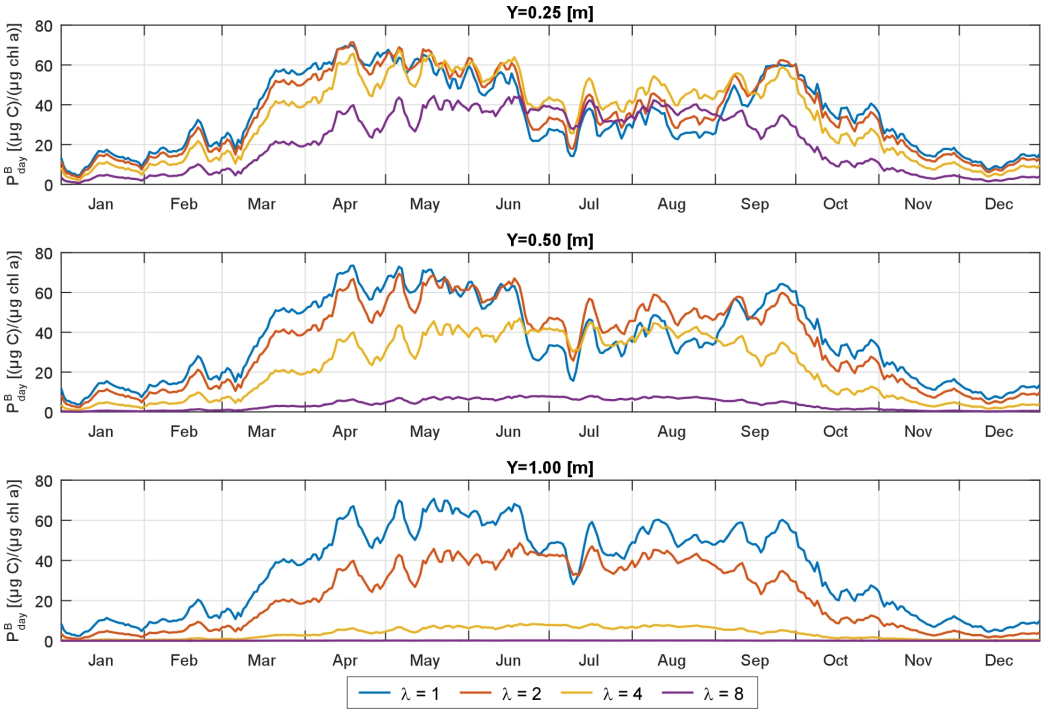

Figure 7.8: Seasonal dynamics of the daily integral of the MPB photosynthetic rate (P^B_{day} $[\mu g\ C(\mu g\ Chl\ a)^{-1}]$) as function of the water column turbidity (described by λ $[m^{-1}]$) and of the water depth Y $[m]$. The results refer to the entire year 2016.

the results we obtained with our synthetic analysis suggest the possibility of investigating a positive feedback between water column turbidity conditions and the MPB proliferation. In fact, the reduction in sediments resuspension provided by the bio-stabilization ensured by the MPB would reduce the water column turbidity, creating more suitable conditions for MPB to proliferate and to further increase the bio-stabilization of the bed sediments.

The results of the present analysis further suggest the necessity of better investigating the interaction between the morphodynamics and MPB biomass growth in shallow coastal environments. The stabilizing effect of MPB and its role in driving the long term evolution of tidal environments has been already accounted for in the literature (e.g. Marani et al. (2010)) but only assuming a constant increase of the critical shear stress for erosion provided by the

EPS biofilm that immediately establishes over the bed sediments when local conditions are suitable for MPB colonization. Marani et al. (2010), for example, assume that those favorable conditions for MPB colonization are simply related to the local water depth assumed as a proxy for the light availability (i.e. a constant water turbidity is considered). More realistically, during a storm event producing sediment resuspension, the EPS biofilm is disrupted and the MPB requires time to recover and restore the stabilizing effect on the sediments. Our results suggest that recovery is strongly affected by the water column depth and turbidity. Moreover, recent studies (Chen et al. (2017)) showed that the strength of the bio-stabilization is "age" dependent, affecting progressively deeper layers as the MPB biomass grows. Therefore, a time evolution of the critical threshold for sediments erosion depending on the MPB biomass growth, affected by water depth and turbidity conditions and by the frequency of the resuspension events (Carniello et al. (2016)) (i.e. the time available for the MPB to recover) would potentially improve our understanding of the short and long term bio-morphodynamic evolution of coastal environments.

Chapter 8

Bidimensional Model: Preliminary Results

As discussed in Chapter 6, in order to investigate without restrictions the temperature dynamics, a bidimensional approach is needed for estimating the horizontal energy flux induced by tidal and wind currents.
Therefore, a step forward in our research is provided by the implementation of the formulation presented and tested with the "point" model into a fully spatial hydro-morphodynamic model, in order to describe the time-space dynamics of the water temperature within shallow water environments.
Here we present the preliminary results obtained by implementing the temperature module into a bidimensional hydro-morphodynamic model developed by the researchers of the Civil, Environmental and Architectural Engineering department of the University of Padova.

8.1 Numerical Model

8.1.1 Hydro-morphodynamic and Wave Modules

The hydro-morphodynamic model was specifically developed for very shallow tidal environments. Three modules constitute the model: the hydrodynamic module and the wind wave module, combined for providing the Wind Wave Tidal Model (WWTM) (Carniello et al., 2011), and the sediment and bed evolution module STABEM (Carniello et al., 2012).

The hydrodynamic module solves the bi-dimensional shallow water equations using a semi-empirical staggered finite element method based on the Galerkin's approach (Defina, 2000). The shallow water equations are adapted in order to account for the flooding and drying process typically characterizing large portions (i.e. salt marshes) of the tidal environments. The information provided by the hydrodynamic solution are exploited by the wind wave module to compute the wave group celerity and the wave energy dissipation and breaking processes. The wind wave model solves the wave action conservation equation parameterized using the zero-order moment of the wave action spectrum in the frequency domain (Holthuijsen et al., 1989). An empirical correlation function, relating the mean peak wave period to the local wind speed and water depth (Young and Verhagen, 1996; Carniello et al., 2011), is used to estimate the spatial and temporal variation of the wave period. Following the interpolation technique proposed by Brocchini et al. (1995), the WWTM uses the available wind data to reconstruct the spatial distribution of the wind speed and direction.

STABEM computes sediment resuspention and redistribution within the domain induced by wind waves and tidal currents by simultaneously solving the advection diffusion equation and Exner's equation. Following Soulsby (1997), the model computes the total bottom shear stress accounting for the nonlinear wave current interaction, that enhances the shear stress value beyond the sum of the two contributions. To correctly reproduce the near-threshold conditions for sediments entrainment, STABEM uses a stochastic approach: the erosion rate depends on the probability that the total bottom shear stress exceeds the critical shear stress for erosion, with both the total shear stress and the critical shear stress treated as random variables characterized by a lognormal distribution. The stochastic approach allows us to take into account the periodicity that characterizes the resuspension events and to describe the consequent transition between no sediment motion and fully developed entrainment (Carniello et al., 2012).

Both WWTM and STABEM were successfully tested comparing the results provided by the models to observed data (Carniello et al., 2011; Mariotti and Fagherazzi, 2010; Carniello et al., 2012, 2014).

8.1.2 Temperature Module

We implemented in the existing hydro-morphodynamic model a temperature module that computes the vertical and horizontal energy fluxes driving the water temperature dynamics. The temperature module exploits the information provided by the hydrodynamic module necessary for estimating the space-time variability of the water temperature (e.g. water levels, water flow produced by tide and wind).
The model describes the water temperature dynamics by solving the advection diffusion equation:

$$\frac{\partial T_w Y}{\partial t} + \nabla \mathbf{q} T_w - \nabla \left(\mathbf{D} Y \nabla T_w \right) = H_N \tag{8.1}$$

with T_w $[^\circ C]$ is the water temperature, Y $[m]$ is the water depth, $\mathbf{q} = (q_x, q_y)$ $[m^3 s^{-1}]$ is the flow rate per unit width (Defina, 2000), $\mathbf{D}$ is the two dimensional diffusion tensor, H_N is the net vertical energy flux.
The net vertical energy flux H_N is given by the sum of the energy fluxes at the AWI, computed following the formulas described in Section 4.3 and tested by applying the "point" model. Following the results discussed in Chapter 5 and 6, the role of the heat exchanged at the SWI between the water column and the bed sediments is negligible for the water temperature dynamics. Therefore, we neglect the energy flux at the SWI in the water column energy balance in this preliminary version of the temperature module; thus no information about the sediments temperature are needed to compute the water temperature dynamics.

8.1.3 Required Data

In order to apply the bidimensional model, we need to provide the following information:

- a numerical grid of the spatial domain reproducing the bathymetry of the tidal domain;
- the tidal level at the sea, h $[m]$, and the wind speed, V_{wind} $[m\ s^{-1}]$, and direction, D_{wind} $[GN]$, to be used as BC for computing the hydrodynamic and the wind wave generation, propagation and dissipation processes;

- the spatial distribution of the water temperature at time $t = 0\ s$;
- the time evolution of the water temperature at the sea, T_S $[°C]$;
- the meteorological data to be imposed as upper BC necessary for computing the energy fluxes at the AWI (i.e. solar radiation at the water surface R_{sun} $[W\ m^{-2}]$, air temperature T_{air} $[°C]$, relative humidity H_{rel} (%), atmospheric pressure p_{atm} $[mbar]$, wind speed V_{wind} $[m\ s^{-1}]$, wind direction, D_{wind} $[GN]$, fraction of covered sky N);
- an estimate of the average water column turbidity for defining the extinction coefficient η $[m^{-1}]$.

8.2 Model Application

We applied the bidimensional model to the Venice lagoon, a shallow water basin where the hydro-morphodynamic model has been widely tested. In particular, the preliminary results presented in this chapter refer to simulations reproducing the period between the 6^{th} and the 12^{th} of July 2010, a period for which all the data necessary to run the model were available.

8.2.1 Input Dataset

The meteorological data required as BC for the model application are provided by the Venice Municipality through its Tidal Forecast and Alert Center with a 5-minutes resolution. For each necessary variable, we used the data provided by the same monitoring station described in Section 3.3, whose location is shown in Figure 8.1(a). Apart from wind speed and direction, the spatial distribution of the meteorological variables is assumed to be uniform on the whole Lagoon. In addition to wind data measured at the monitoring station of Saline-Laguna Nord, we considered the data measured at the monitoring station of Chioggia (located in the southern part of the Lagoon). Exploiting the information provided by the two measuring stations, located at the opposite side of the Lagoon, the model reconstructs the wind field over the Lagoon following the approach described by Carniello et al. (2012).
The lack of cloudiness data forced us to assume a constant value of cloudiness. In particular, we assumed $N = 0$, value that describes a clear sky

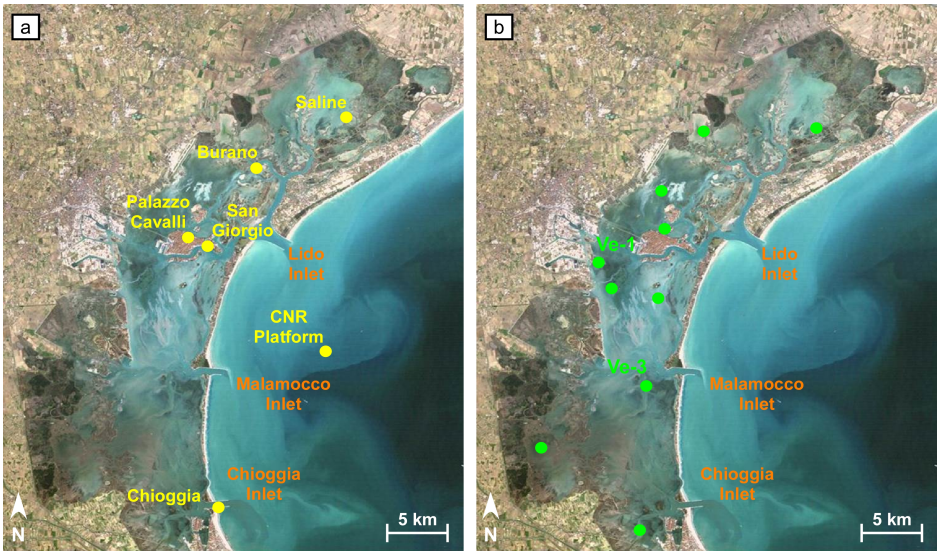

Figure 8.1: Satellite images of the Venice Lagoon showing the location of: (a) the measuring station (yellow dots) of the Venice Municipality Monitoring Network that provided the meteorological data; (b) the multiparametric gauges *Ve* (green dots) managed by Consorzio Venezia Nuova that provided the water temperature measured at different locations within the Lagoon.

condition, which can be reasonably representative of a Summer period.
The Venice Municipality Monitoring Network further provided the sea water temperature (T_S $[°C]$) and the tidal level (h $[m]$) measured at the off-shore CNR platform. Both these datasets were used as BC at the boundary of the spatial domain at the sea.

Water temperature data inside the Lagoon were provided by the 10 measuring stations managed by Consorzio Venezia Nuova (identified as *Ve* measuring stations), whose location is shown in Figure 8.1(b). Each station is equipped with a multiparametric gauge that measures water temperature, salinity, turbidity and dissolved oxygen. We used the temperature data provided by the measuring stations first to estimate a reliable spatial distribution of the water temperature within the Lagoon to be used as IC, and then to evaluate the model capability to describe the water temperature dynamics by comparing the observations with the results provided by the model.

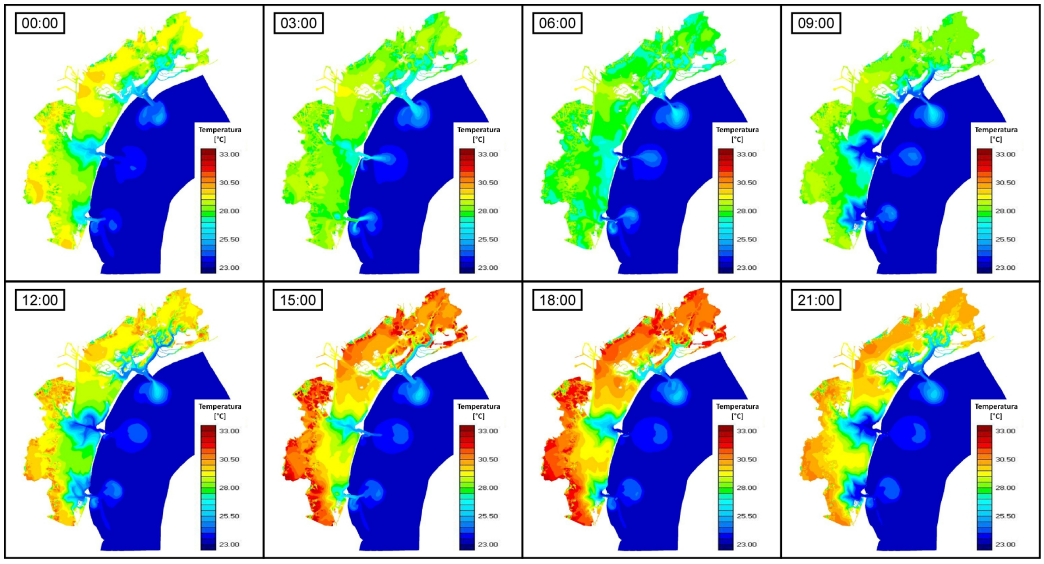

Figure 8.2: Spatial distribution of the water temperature within the Lagoon computed by the 2-D model at different hours of the 3^{rd} day of simulation (the 9^{th} of July).

8.2.2 Preliminary Results

We ran a 7-days-long simulation, lasting from the 6^{th} to the 12^{th} of July 2010. We used the first 24 *hours* to initialize the Lagoon's hydrodynamic; the simulation of the water temperature space-time evolution starts from the second day of simulation considering the initial water temperature spatial distribution reconstructed from the data collected by the *Ve* Stations.

Figure 8.2 shows the water temperature spatial distribution provided by the model at different hours of the 4^{th} day of simulation (i.e. July 9).
On average, we observe that the water temperature within the Lagoon decreases during night and increases during the day, as a consequence of the warming effect provided by the solar radiation. In fact, especially during Summer, the short-wave radiation represents the major contribution to the water column energy balance. We observe the lowest water temperature values before the dawn (e.g. temperature distribution at 06:00 in Figure 8.2), while the warmest condition characterizes the late afternoon hours (e.g. temperature distribution at 18:00 in Figure 8.2). Excluding the areas near the inlets, the shallower areas of the Lagoon experience both the minimum

and maximum observed temperature values: decreasing the water depth, the thermal inertia of the water column decreases, leading to larger temperature variation.
The analysis of the reconstructed time and spatial dynamics of the water temperature provides also interesting observations on the relevance of the horizontal heat transport induced by the tidal currents. Focusing on the temperature distribution at 09:00, 12:00 and 21:00 in Figure 8.2, we clearly recognizes the cooling effect, especially near the inlets, provided by the cold water entering into the Lagoon during the flood phase of the tide (during Summer the water temperature at the sea is lower than inside the Lagoon). Furthermore, the temperature distribution in the northern part of the Lagoon shows that the lagoonal channels act as preferential paths for the water coming from the sea to propagate inside the Lagoon, favoring the entrance of the colder water from the sea.

In order to further investigate the advection importance, we compared the water temperature measured by the multiparametric gauges within the Lagoon with the temperature computed by both the "point" model (1-D) and the bidimensional model. In particular, Figure 8.3 shows the comparison between the measured and computed water temperature at the location corresponding to the measuring station *Ve-1* (Figure 8.3(a)) and *Ve-3* (Figure 8.3(b)), whose positions are specified in Figure 8.1. Focusing on Figure 8.3(a), we observe that both the 1-D and the 2-D models provide a proper description of the water temperature dynamics at the *Ve-1* station. This measuring station is located far from the inlets and close to the divide separating the central sub-basin (i.e. referring to the Malamocco inlet) and the Northern sub-basin (i.e. referring to the Lido inlet); therefore the tidal currents in this position are low and the contribution of the advective energy transport to the energy balance is almost negligible. Conversely, the station *Ve-3*, is located close to the Malamocco inlet, is much more affected by the tidal currents induced by the tide oscillation. Here the effect of the advective components to the energy balance becomes crucial, as we observe in Figure 8.3(b). During the last three days of simulation, the measured water temperature, instead of increasing because of the energy provided by the solar radiation, decreases during daytime because of the cold water coming from the sea during the flood phase of the tide. This behavior is correctly described by the 2-D model which accounts for the advective component in the water column energy balance, while it can not be described by the 1-D model

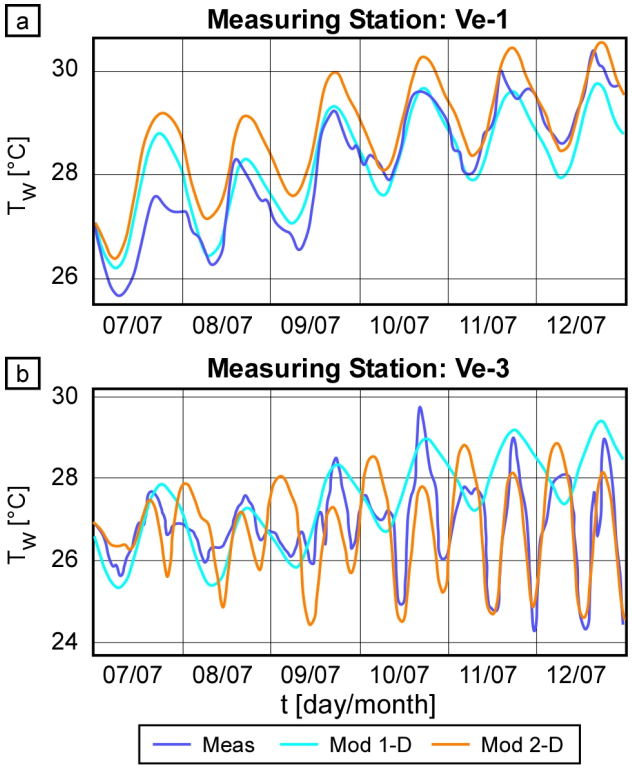

Figure 8.3: Comparison between the water temperature measured (Meas) and computed using the "point" model (Mod 1-D) and the bidimensional model (Mod 2-D). Panel (a) and (b) show respectively the comparison referred to the water temperature at the measuring station *Ve-1* and at the measuring station *Ve-3*. The position of the measuring stations is specified in Figure 8.1.

that computes only the vertical energy contributions to the water column energy balance. The above observations confirm that for describing the water temperature dynamics within the Lagoon without restrictions regarding the location and the amplitude of the tide oscillation, a bidimensional approach is required.

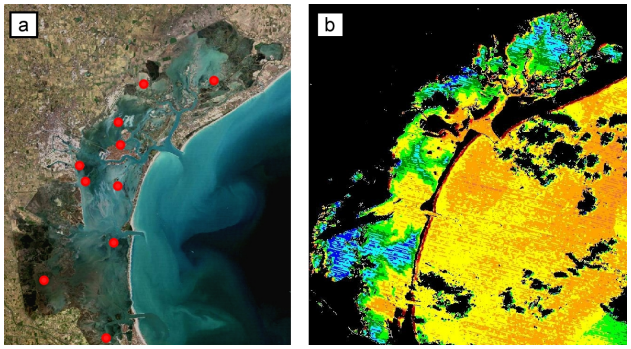

Figure 8.4: Panel (a) shows the location of the measuring stations *Ve*, managed by Consorzio Venezia Nuova, while Panel (b) shows the water temperature spatial distribution within the Venice lagoon provided by a satellite image. The combination of the two data retrieval procedures provides a full description of the water temperature time-space variability.

8.2.3 Future Developments

The preliminary results provided by the bidimensional model are satisfactory and encouraging for the future development of the model itself. However, more work is required in order to improve the model capability to correctly describe the water temperature dynamics. In particular, we observed that the model tends to overestimate the water temperature, especially in the shallower areas of the water body, far from the inlets.

We need to extend the available dataset necessary to test the model, integrating the use of point measurements (e.g. observations provided by the *Ve* measuring stations) with information provided by satellite images (see Figure 8.4). In situ point measurements ensure useful information about the time evolution of the temperature dynamics, but their distribution within the water basins is usually not sufficient to describe the spatial variability of the process. Instead, satellite images provide a full description of the water temperature spatial distribution, but not of the time evolution of the process, being the time interval between two consecutive images typically of the order of days. Combining the information provided by point measurements and satellite images it is possible to overcome the limitations of both the data retrieval procedure to obtain a much more complete description of the process we are interested in.

Chapter 9

Summary and Conclusions

The purpose of the present study is to investigate the water and sediment temperature dynamics and their thermal interaction in shallow coastal environments.
Coastal environments are of great importance for both their ecological and socioeconomic implications. Coastal ecosystems are in fact characterized by high biodiversity and primary productivity rates, providing fundamental ecosystem services. Important urban centers are usually located along the coastline, and their economy is strictly connected to the surrounding environment (e.g. fisheries, commercial ports, industrial area exploiting the water resource), leading to a strong anthropogenic pressure threatening the ecosystem. In order to preserve these ecosystems, we must monitor and study the processes driving their eco-bio-morphological evolution.
Water and sediment temperature is one of the major factor driving many ecological and biological processes affecting the ecosystem (e.g. dissolved oxygen, benthic algae growth and death, proliferation of animal and plants species).

In the present study, we focused on the Venice Lagoon, a worldwide famous shallow water basin located in the northeastern part of Italy and characterized by a temperate climate.
We collected temperature data within the water-sediment continuum in a tidal flat and developed a "point" energy balance model that solves for energy transfer processes in the water-sediment continuum. The model computes the energy fluxes at the air-water and sediment-water interface and thus describes the water-sediment temperature dynamics, enabling us to draw some

interesting inferences from the observations.

The temperature data collected *in situ* show a quite uniform distribution of the temperature within the water column, allowing us to describe the temperature state of the water column with a single temperature value. Sediment temperature varies over daily time scales within the topmost $30-50\ cm$ layer, while seasonal scale temperature variations propagate throughout the entire $1.50\ m$ layer of sediment where we deployed temperature sensors during our field observations.

Sediment temperature data allowed us to estimate the energy flux at the sediment-water interface. The flux computed on the basis of the recorded data was then reconstructed as the sum of two components, a conductive heat flux and the residual solar radiation reaching the sediment bottom. We found that, under the investigated conditions, the contribution of the residual solar radiation is negligible: the average water turbidity is such that most of the incoming solar radiation is either reflected at the water surface or absorbed within the water column even when water depth is small ($Y \approx 0.3\ m$). Conductive heat flux is thus the chief energy transfer mechanism at the sediment-water interface and crucial to model the sediment temperature dynamics.
However, comparing this energy flux with the energy fluxes at the air-water interface, computed using formulas from the literature forced by the meteorological data provided by the Venice Municipality Monitoring Network, we observed that the contribution to the water column energy balance of the heat flux at the sediment-water interface (SWI) is very small, mostly less than 10% at the hourly timescale and mostly less than 5% at the daily timescale, independently on the season. This observation suggests the possibility to model the water temperature dynamics, in shallow water environment characterize by meteorological condition similar to our case study (i.e. the Venice lagoon), solely as a function of the heat fluxes at the air-water interface.

Using parameter values calibrated on the basis of our observations, we applied the 1-D model to describe the dynamics of the temperature profile of the water-sediment continuum.
The model applicability is limited because of the relevant role often played by the horizontal heat transport related to advection, not accounted for by a 1-D approach like the "point" model we developed. In fact, even if the

study site where we performed the field campaign was located quite close to an internal divide of the lagoon in order to limit the horizontal transport related to advection, we found the latter being often not negligible.
However, focusing on periods characterized by conditions such as to limit advection (i.e. neap tide and small difference between the water temperature at the sea and inside the Lagoon), we observed that the "point" model properly represents the measured dynamics of the vertical temperature profile within the water-sediment continuum. Model application further confirms that neglecting the heat flux at the SWI minimally affects the capability of the model in correctly reproducing the water column temperature dynamics.

The application of the "point" model to a synthetic configuration representing a shallow environments at temperate latitude allowed us to study the effect of different water depths and water column turbidity conditions on the dynamics of the water and sediment temperature. The results provided by the model application to this synthetic configuration allowed us also to investigate the potential effect of the different water depths and turbidity conditions on the MPB proliferation, which has crucial implication for the ecosystem (i.e. primary productivity, sediment bed stabilization).
Interestingly, we found that the time evolution of the water temperature is poorly affected by the different turbidity conditions investigated, while the variation of the sediment temperature dynamics is significant, especially for very shallow water conditions (i.e. water depth $\leq 0.5\ m$). The negligible effect of turbidity on the water temperature can be explained analyzing the heat fluxes driving the water column temperature dynamics. Decreasing the water column turbidity, the solar radiation absorption decreases (i.e. solar absorption capacity of the water column decreases) and therefore decreases the energy supply to the energy balance of the water column provided by the solar irradiance. However, the solar energy not absorbed by the water column reaches the bottom, increasing the sediment surface temperature and the temperature gradient between water and sediments at the sediment-water interface. Therefore, we observe an increase of the conductive heat flux between water and sediment and directed toward the water that compensates the reduction of energy supply related to the solar radiation absorption.
Sediment temperature and light availability are two major factors driving the photosynthetic rate of the MPB (i.e. a proxy of the potential MPB biomass growth rate). Studying the dynamics of the MPB photosynthetic rate as function of the results obtained for the investigated synthetic config-

uration, we observe that throughout the year the process is better promoted by clear water conditions (i.e. low turbidity), being the light availability at the bottom the major limiting factor. The sediment temperature becomes the major limiting factor for the MPB photosynthesis only during summer and for very shallow water depth (i.e. water depth $\leq 0.5\ m$), when the solar radiation reaching the bottom with low water turbidity conditions increases the sediment temperature over the optimal temperature for the photosynthetic process. However, considering the average annual budget, clear water conditions result to better promote the MPB photosynthesis and proliferation.
Since an abundance of MPB biomass provides a bio-stabilization effect on the surface sediments, reducing sediments resuspention and therefore the water column turbidity, the results provided by the synthetic analysis we performed suggest the possibility of investigating a positive feedback between water column turbidity and the MPB proliferation.

We think that the formulation presented and tested here with the "point" model constitutes a building block that can be incorporated into a fully spatial hydro-morphodynamic model providing proper description of the horizontal advective-dispersive energy transport (e.g. Carniello et al. (2011), Carniello et al. (2012), Carniello et al. (2014)). A bidimensional model capable of describing both the hydro-morphodynamics and the temperature dynamics of shallow coastal environments would be a useful and necessary tool for coupling physical and biological processes, investigating their mutual interaction (e.g. the bio-stabilization provided by the MPB previously discussed) in the short and long term evolution of the ecosystem.
Proper testing of such a fully spatial energy balance model will require temperature observations distributed in space and time (e.g. through remote sensing) and will contribute to further our predictive understanding of temperature dynamics in shallow water environments.

Bibliography

Barranguet, C., Kromkamp, J., and Peene, J. (1998). Factors controlling primary production and photosynthetic characteristics of intertidal microphytobenthos. *Marine Ecology Progress Series*, 173(1994):117–126.

Battin, T. J., Luyssaert, S., Kaplan, L. A., Aufdenkampe, A. K., Richter, A., and Tranvik, L. J. (2009). The boundless carbon cycle. *Nature Geoscience*, 2(9):598–600.

Bendoni, M., Mel, R., Solari, L., Lanzoni, S., Francalanci, S., and Oumeraci, H. (2016). Insights into lateral marsh retreat mechanism through localized field measurements. *Water Resources Research*, 52:1446–1464.

Bignami, F., Marullo, S., Santoleri, R., and Schiano, M. E. (1995). Longwave radiation budget in the Mediterranean Sea. *Journal of Geophysical Research*, 100(C2):2501.

Black, K. S., Tolhurst, T. J., Paterson, D. M., and Hagerthey, S. E. (2002). Working with natural cohesive sediments. *Journal of Hydraulic Engineering*, 128(1):2–8.

Blanchard, G. and Guarini, J. (1996). Studying the role of mud temperature on the hourly variation of the photosynthetic capacity of microphytobenthos in intertidal areas. *Comptes rendus de l'Académie des sciences. Série 3, Sciences de la vie*, 319(12):1153–1158.

Blanchard, G. F. and Gall, V. C.-L. (1994). Photo synthetic characteristics of microphytobenthos in Marennes-Oléron Bay, France: Preliminary results. *Journal of Experimental Marine Biology and Ecology*, 182(1):1–14.

Blanchard, G. F., Guarini, J.-M., Gros, P., and Richard, P. (1997). Seasonal effect on the relationship between the photosynthetic capacity of intertidal microphytobenthos and temperature. *Journal of Phycology*, 33(5):723–728.

Boike, J., Georgi, C., Kirilin, G., Muster, S., Abramova, K., Fedorova, I., Chetverova, A., Grigoriev, M., Bornemann, N., and Langer, M. (2015). Thermal processes of thermokarst lakes in the continuous permafrost zone of northern Siberia - observations and modeling (Lena River Delta, Siberia). *Biogeosciences*, 12(20):5941–5965.

Bouin, M. N., Caniaux, G., Traullé, O., Legain, D., and Le Moigne, P. (2012). Long-term heat exchanges over a Mediterranean lagoon. *Journal of Geophysical Research Atmospheres*, 117(23):1–18.

Brocchini, M., Wurtele, M., Umgiesser, G., and Zecchetto, S. (1995). Calculation of a Mass-Consistent Two-Dimensional Wind Field with Divergence Control.

Carniello, L., D'Alpaos, A., Botter, G., and Rinaldo, A. (2016). Statistical characterization of spatiotemporal sediment dynamics in the Venice lagoon. *Journal of Geophysical Research F: Earth Surface*, 121(5):1049–1064.

Carniello, L., D'Alpaos, A., and Defina, A. (2011). Modeling wind waves and tidal flows in shallow micro-tidal basins. *Estuarine, Coastal and Shelf Science*, 92(2):263–276.

Carniello, L., Defina, A., and D'Alpaos, L. (2009). Morphological evolution of the Venice lagoon: Evidence from the past and trend for the future. *Journal of Geophysical Research: Earth Surface*, 114(4):1–10.

Carniello, L., Defina, A., and D'Alpaos, L. (2012). Modeling sand-mud transport induced by tidal currents and wind waves in shallow microtidal basins: Application to the Venice Lagoon (Italy). *Estuarine, Coastal and Shelf Science*, 102-103:105–115.

Carniello, L., Silvestri, S., Marani, M., D'Alpaos, A., Volpe, V., and Defina, A. (2014). Sediment dynamics in shallow tidal basins: In situ observations, satellite retrievals, and numerical modeling in the Venice Lagoon. *Journal of Geophysical Research: Earth Surface*, 119(4):802–815.

Carr, J., D'Odorico, P., McGlathery, K., and Wiberg, P. (2010). Stability and bistability of seagrass ecosystems in shallow coastal lagoons: Role of feedbacks with sediment resuspension and light attenuation. *Journal of Geophysical Research: Biogeosciences*, 115(3):1–14.

Carr, J. A., D'Odorico, P., McGlathery, K. J., and Wiberg, P. L. (2015). Spatially explicit feedbacks between seagrass meadow structure, sediment and light: Habitat suitability for seagrass growth. *Advances in Water Resources*, 93:315–325.

Chen, X. D., Zhang, C. K., Paterson, D. M., Thompson, C. E. L., Townend, I. H., Gong, Z., Zhou, Z., and Feng, Q. (2017). Hindered erosion: The biologicalmediation of noncohesive sediment behavior. *Water Resources Research*, 53:4787–4801.

Cho, H.-Y. and Lee, K.-H. (2012). Development of an Air-Water Temperature Relationship Model to Predict Climate-Induced Future Water Temperature in Estuaries. *Journal of Environmental Engineering-Asce*, 138(5):570–577.

Cochero, J., Licursi, M., and Gómez, N. (2014). Changes in the epipelic diatom assemblage in nutrient rich streams due to the variations of simultaneous stressors. *Limnologica*, 51:15–23.

Cronk, J. K. and Fennessy, M. S. (2016). *Wetland Plants: Biology and Ecology*. CRC Press.

D'Alpaos, L. (2010). *Fatti e misfatti di idraulica lagunare. La laguna di Venezia dalla diversione dei fiumi alle nuove opere delle bocche di porto*. Istituto Veneto di Scienze, Lettere e Arti.

Defina, A. (2000). Two-dimensional shallow flow equations for partially dry areas. *Water Resources Research*, 36(11):3251–3264.

Denman, K. L. and Miyake, M. (1973). Upper Layer Modification at Ocean Station Papa: Observations and Simulation.

Du, G., Yan, H., Liu, C., and Mao, Y. (2016). Behavioral and physiological photoresponses to light intensity by intertidal microphytobenthos. *Chinese Journal of Oceanology and Limnology*.

Fairall, C. W., Bradley, E. F., Hare, J. E., Grachev, A. A., and Edson, J. B. (2003). Bulk parameterization of air-sea fluxes: Updates and verification for the COARE algorithm. *Journal of Climate*, 16(4):571–591.

Fairall, C. W., White, A. B., Edson, J. B., and Hare, J. E. (1997). Integrated shipboard measurements of the marine boundary layer. *Journal of Atmospheric and Oceanic Technology*, 14(3):338–359.

Fang, X. and Stefan, G. (1998). Temperature variability in lake sediments depth. *Water Resources*, 34(4):717–729.

Fang, X. and Stefan, H. G. (1996). Dynamics of heat exchange between sediment and water. *Water Resources Research*, 32(6):1719–1727.

FAO (2001). World fisheries and aquaculture atlas cd-rom.

Gambolati, G. and Pietro Teatini (2013). *Venice Shall Rise Again.* Elsevier Science.

Gritti, E. S., Smith, B., and Sykes, M. T. (2006). Vulnerability of Mediterranean Basin ecosystems to climate change and invasion by exotic plant species. *J. Biogeogr.*, 33(1):145–157.

Guarini, J. M., Blanchard, G. F., Gros, P., Gouleau, D., and Bacher, C. (2000). Dynamic model of the short-term variability of microphytobenthic biomass on temperate intertidal mudflats. *Marine Ecology Progress Series*, 195:291–303.

Guarini, J. M., Blanchard, G. F., Gros, P., and Harrison, S. J. (1997). Modelling the mud surface temperature on intertidal flats to investigate the spatio-temporal dynamics of the benthic microalgal photosynthetic capacity. *Marine Ecology Progress Series*, 153(1-3):25–36.

Hagy, J. D., Boynton, W. R., Keefe, C. W., and Wood, K. V. (2004). Hypoxia in Chesapeake Bay, 1950–2001: Long-term change in relation to nutrient loading and river flow. *Estuaries*, 27(4):634–658.

Harrison, S. J. and Phizacklea, A. P. (1985). SEASONAL CHANGES IN HEAT FLUX AND HEAT STORAGE IN THE INTERTIDAL MUDFLATS OF THE FORTH ESTUARY , SCOTLAND. *Journal of Climatology*, 5:473–485.

Hearn, C. J. and Robson, B. J. (2001). Inter-annual variability of bottom hypoxia in shallow mediterranean estuaries. *Estuarine Coastal and Shelf Science*, 52(5):643–657.

Holthuijsen, L. H., Booij, N., and Herbers, T. H. C. (1989). A prediction model for stationary, short-crested waves in shallow water with ambient currents. *Coastal Engineering*, 13(1):23–54.

Imboden, D. and Wuest, A. (1995). *Physics and Chemistry of Lakes, chap. 4 Mixing Mechanisms in Lakes*. Springer-Verlag.

Jassby, A. D. and Platt, T. (1976). Mathematical formulation of the relationship between photosynthesis and light for phytoplankton. *Limnology and Oceanography*, 21(4):540–547.

Kemp, W. M., Boynton, W. R., Adolf, J. E., Boesch, D. F., Boicourt, W. C., Brush, G., Cornwell, J. C., Fisher, T. R., Glibert, P. M., Hagy, J. D., Harding, L. W., Houde, E. D., Kimmel, D. G., Miller, W. D., Newell, R. I., Roman, M. R., Smith, E. M., and Stevenson, J. C. (2005). Eutrophication of Chesapeake Bay: Historical trends and ecological interactions. *Marine Ecology Progress Series*, 303:1–29.

Kettle, H., Thompson, R., Anderson, N. J., and Livingstone, D. M. (2004). Empirical modeling of summer lake surface temperatures in southwest Greenland. *Limnology and Oceanography*, 49(1):271–282.

Kim, T. W., Cho, Y. K., and Dever, E. P. (2007). An evaluation of the thermal properties and albedo of a macrotidal flat. *Journal of Geophysical Research: Oceans*, 112(12):1–9.

Kingston, M. B. (1999). Effect of light on vertical migration and photosynthesis of Euglena proxima (Euglenophyta). *J. Phycol*, 35:245–253.

Kirillin, G., Engelhardt, C., and Golosov, S. (2009). Transient convection in upper lake sediments produced by internal seiching. *Geophysical Research Letters*, 36(18):1–5.

Kirwan, M. L. and Murray, A. B. (2007). A coupled geomorphic and ecological model of tidal marsh evolution. *Proceedings of the National Academy of Sciences of the United States of America*, 104(15):6118–22.

Lee, Y. J. and Lwiza, K. M. M. (2008). Characteristics of bottom dissolved oxygen in Long Island Sound, New York. *Estuarine, Coastal and Shelf Science*, 76(2):187–200.

MacIntyre, H. L., Geider, R. J., and Miller, D. C. (1996). Microphytobenthos: The Ecological Role of the "Secret Garden" of Unvegetated, Shallow-Water Marine Habitats. I. Distribution, Abundance and Primary Production. *Estuaries*, 19(2):186–201.

Marani, M., D'Alpaos, A., Lanzoni, S., Carniello, L., and Rinaldo, A. (2010). The importance of being coupled: Stable states and catastrophic shifts in tidal biomorphodynamics. *Journal of Geophysical Research: Earth Surface*, 115(4):1–15.

Mariotti, G. and Fagherazzi, S. (2010). A numerical model for the coupled long-term evolution of salt marshes and tidal flats. *Journal of Geophysical Research: Earth Surface*, 115(1):1–15.

Martínez, M. L., Intralawan, A., Vázquez, G., Pérez-Maqueo, O., Sutton, P., and Landgrave, R. (2007). The coasts of our world: Ecological, economic and social importance. *Ecological Economics*, 63(2-3):254–272.

Martynov, A., Sushama, L., and Laprise, R. (2010). Simulation of temperate freezing lakes by one-dimensional lake models: Performance assessment for interactive coupling with regional climate models. *Boreal Environment Research*, 15(2):143–164.

MAV (2004). Attivitá di monitoraggio ambientale della laguna di Venezia - Attivitá A.2: trattamento ed analisi dei dati di qualitá dell'acqua, elaborazioni in linea ed interpretazioni spazio temporali. Technical report, Ministero delle infrastrutture e dei trasporti - Magistrato delle Acque (Venezia) - Consorzio Venezia Nuova, Executor: Consorzio INCA.

Mesinger, F., Chou, S. C., Gomes, J. L., Jovic, D., Bastos, P., Bustamante, J. F., Lazic, L., Lyra, A. A., Morelli, S., Ristic, I., and Veljovic, K. (2012). An upgraded version of the Eta model. *Meteorology and Atmospheric Physics*, 116(3-4):63–79.

Miller, D. C., Geider, R. J., and MacIntyre, H. L. (1996). Microphytobenthos: The Ecological Role of the "Secret Garden" of Unvegetated, Shallow-Water

Marine Habitats. II. Role in Sediment Stability and Shallow-Water Food Webs. *Estuaries*, 19(2):202.

Molinaroli, E., Guerzoni, S., Sarretta, A., Masiol, M., and Pistolato, M. (2009). Thirty-year changes (1970 to 2000) in bathymetry and sediment texture recorded in the Lagoon of Venice sub-basins, Italy. *Marine Geology*, 258(1-4):115–125.

Morrill, J. C., Bales, R. C., and Conklin, M. H. (2005). Estimating Stream Temperature from Air Temperature: Implications for Future Water Quality. *Journal of Environmental Engineering*, 131(1):139–146.

Nishri, A., Rimmer, A., and Lechinsky, Y. (2015). The mechanism of hypolimnion warming induced by internal waves. *Limnology and Oceanography*, 60(4):1462–1476.

Parsons, D. R., Schindler, R. J., Hope, J. A., Malarkey, J., Baas, J. H., Peakall, J., Manning, A. J., Ye, L., Simmons, S., Paterson, D. M., Aspden, R. J., Bass, S. J., Davies, A. G., Lichtman, I. D., and Thorne, P. D. (2016). The role of biophysical cohesion on subaqueous bed form size. *Geophysical Research Letters*, 43(4):1566–1573.

Paterson, D. M. (1989). Short-term changes in the erodibility of intertidal cohesive sediments related to the migratory behavior of epipelic diatoms. *Limnology and Oceanography*, 34(1):223–234.

Paterson, D. M. and Black, K. S. (1999). Water Flow, Sediment Dynamics and Benthic Biology. *Estuaries*, 29(Supplement C):155–193.

Piccolo, M. C., Perillo, G. M. E., and Daborn, G. R. (1993). Soil temperature variations on a tidal flat in Minas Basin, Bay of Fundy, Canada.

Piccolroaz, S., Healey, N. C., Lenters, J. D., Schladow, S. G., Hook, S. J., Sahoo, G. B., and Toffolon, M. (2017). On the predictability of lake surface temperature using air temperature in a changing climate: A case study for Lake Tahoe (U.S.A.). *Limnology and Oceanography*.

Piccolroaz, S., Toffolon, M., and Majone, B. (2013). A simple lumped model to convert air temperature into surface water temperature in lakes. *Hydrology and Earth System Sciences*, 17(8):3323–3338.

PRB (2012). Ripple effects: Population and coastal regions.

Sharma, S., Walker, S. C., and Jackson, D. A. (2008). Empirical modelling of lake water-temperature relationships: A comparison of approaches. *Freshwater Biology*, 53(5):897–911.

Smith, N. P. (2002). Observations and simulations of water-sediment heat exchange in a shallow coastal lagoon. *Estuaries*, 25(3):483–487.

Smith, S. D. (1988). Coefficients for sea surface wind stress, heat flux, and wind profiles as a function of wind speed and temperature. *Journal of Geophysical Research: Oceans*, 93(C12):15467–15472.

Smith, S. D., Fairall, C. W., Geernaert, G. L., and Hasse, L. (1996). Air-sea fluxes: 25 years of progress. *Boundary-Layer Meteorology*, 78:247–290.

Solidoro, C., Melaku Canu, D., Cucco, A., and Umgiesser, G. (2004). A partition of the Venice Lagoon based on physical properties and analysis of general circulation. *Journal of Marine Systems*, 51(1-4 SPEC. ISS.):147–160.

Soulsby, R. (1997). *Dynamics of Marine Sands: A Manual for Practical Applications*. Thomas Telford.

Subin, Z. M., Riley, W. J., and Mironov, D. (2012). An improved lake model for climate simulations: Model structure, evaluation, and sensitivity analyses in CESM1. *Journal of Advances in Modeling Earth Systems*, 4(2):1–27.

Taylor, P. K. and Yelland, M. J. (2001). The Dependence of Sea Surface Roughness on the Height and Steepness of the Waves. *Journal of Physical Oceanography*, 31(2):572–590.

Cittá di Venezia (2017). `http://www.comune.venezia.it/archivio/1653`.

IlMeteo (2017). `https://www.ilmeteo.it/`.

Toffolon, M. and Piccolroaz, S. (2015). A hybrid model for river water temperature as a function of air temperature and discharge. *Environmental Research Letters*, 10:1–22.

Tosatto, O., Belluco, E., Silvestri, S., Ursino, N., Comerlati, A., Putti, M., and Marani, M. (2009). Reply to comment by L. R. Gardner on Spatial organization and ecohydrological interactions in oxygen-limited vegetation ecosystems. *Water Resources Research*, 45(5):2–5.

Umgiesser, G., Canu, D. M., Cucco, A., and Solidoro, C. (2004). A finite element model for the Venice Lagoon. Development, set up, calibration and validation. *Journal of Marine Systems*, 51(1-4 SPEC. ISS.):123–145.

Ursino, N., Silvestri, S., and Marani, M. (2004). Subsurface flow and vegetation patterns in tidal environments. *Water Resources Research*, 40(5):1–11.

Venier, C., D'Alpaos, A., and Marani, M. (2014). Evaluation of sediment properties using wind and turbidity observations in the shallow tidal areas of the Venice Lagoon. *Journal of Geophysical Research: Earth Surface*, 119(7):1604–1616.

Viero, D. P. and Defina, A. (2016). Water age, exposure time, and local flushing time in semi-enclosed, tidal basins with negligible freshwater inflow. *Journal of Marine Systems*, 156:16–29.

Wang, C., Miao, L., Hou, J., Wang, P., Qian, J., and Dai, S. (2014). The effect of flow velocity on the distribution and composition of extracellular polymeric substances in biofilms and the detachment mechanism of biofilms. *Water Science & Technology*, 69(4):825.

Williamson, C. E., Saros, J. E., Vincent, W. F., and Smol, J. P. (2009). Lakes and reservoirs as sentinels, integrators, and regulators of climate change. *Limnology and Oceanography*, 54(6_part_2):2273–2282.

Wolf, M. A., Sfriso, A., and Moro, I. (2014). Thermal pollution and settlement of new tropical alien species: The case of Grateloupia yinggehaiensis (Rhodophyta) in the Venice Lagoon. *Estuarine, Coastal and Shelf Science*, 147:11–16.

WRI (2005). Millennium ecosystem assessment: Ecosystems and human well-being - synthesis report.

Young, I. and Verhagen, L. (1996). The growth of fetch limited waves in water of finite depth. Part 1. Total energy and peak frequency. *Coastal Engineering*, 29(1-2):47–78.